

# ANNUAL REPORT

Center for Experimental Nuclear Physics and Astrophysics  
University of Washington  
April, 2012

Sponsored in part by the United States Department of Energy  
under Grant #DE-FG02-97ER41020.

This report was prepared as an account of work sponsored in part by the United States Government. Neither the United States nor the United States Department of Energy, nor any of their employees, makes any warranty, expressed or implied or assumes any legal liability or responsibility for accuracy, completeness or usefulness of any information, apparatus, product or process disclosed, or represents that its use would not infringe on privately-owned rights.

Cover design by Nora Boyd. The upper left photo depicts postdocs Brendan Kiburg and Peter Winter assembling their lead fluoride crystal box for the  $g-2$  experiment (see Sec. 4.4.1) at Fermilab (photo by Vladimir Tishchenko, University of Kentucky). Undergraduate Arielle Steger is pictured upper right as she prepares to pump out the 1000-liter dewar that will supply the ADMX cryostat (see Sec. 5.1) with liquid helium (photo by Nora Boyd). In the lower photo, postdoc Andreas Knecht adjusts one of the many mirrors positioned on the laser table (see Sec. 3.1.3) recently moved to CENPA for the  ${}^6\text{He}$  experiment (photo by Nora Boyd). The background image displays some of the copper shielding donuts (see Sec. 1.1.4) that were recently installed on the KATRIN detector feedthrough flange pogo-pins (photo by Nora Boyd).

## INTRODUCTION

The Center for Experimental Nuclear Physics and Astrophysics, CENPA, was established in 1998 at the University of Washington as the institutional home for a broad program of research in nuclear physics, astrophysics and related fields. Research activities are conducted locally and at remote sites. CENPA has been a major participant in the Sudbury Neutrino Observatory (SNO) and is presently contributing substantially to the KATRIN tritium beta decay experiment, the MAJORANA  $^{76}\text{Ge}$  double-beta decay experiment, and the SNO+  $^{150}\text{Nd}$  double-beta decay experiment in Canada. With the arrival of the Muon Physics group from Illinois we have new activities at the Paul Scherrer Institute in Switzerland and are developing a new program to measure the anomalous magnetic moment of the muon at Fermilab. The fundamental symmetries program also includes “in-house” research using the local tandem Van de Graaff accelerator with a new experiment to measure the electron-neutrino correlation in  $^6\text{He}$  decay, and neutron physics at other locations. We conduct user-mode research on relativistic heavy ions at the Relativistic Heavy Ion Collider at Brookhaven.

The year 2011–2012 has been an exciting and productive one. The focal-plane detector for the KATRIN neutrino mass experiment was finished, tested, disassembled, packed up in dozens of crates and shipped off to Karlsruhe, Germany. There it is being installed and commissioned in time for the first tests of the main spectrometer under the watchful eye of Peter Doe, who moved to Germany for the year. A successful DOE Review was held in August (equivalent to the ‘CD-4’ review in DOE 413.3 parlance), with the conclusion that we had completed our work under budget and without causing project delays (not quite the same as ‘on schedule’, but good enough for some celebration!).

The new muon program under David Hertzog and Peter Kammel has gotten off to a flying start with publication of the ppm-level result for the muon lifetime, a very successful determination of the pseudoscalar coupling constant for muon capture on the proton, and the high priority assigned by the Fermilab PAC to the new muon  $g - 2$  experiment. At PSI the experiment to measure muon capture on deuterium is about to get under way.

Our attention was riveted in March, 2011 by the devastating earthquake and tsunami in Japan. CENPA Fellow Michael Miller, postdocs Andreas Knecht and Jarek Kaspar, and students Alexis Schubert and Jonathan Leon leapt into action to set up an air monitoring system using a MAJORANA prototype detector and the air intake filters from the Physics building. They were ready a day before fission-product activity from the Fukushima Dai-ichi reactors arrived on the West Coast. Although the levels were low from the standpoint of public health, the setup was very sensitive and strong lines were seen from  $^{131}\text{I}$ ,  $^{132}\text{I}$ ,  $^{132}\text{Te}$ ,  $^{134}\text{Cs}$ , and  $^{137}\text{Cs}$ . The team became something of a media sensation because little quantitative information was available from elsewhere. TV and radio crews and newspaper reporters were in abundance for several weeks.

The work of the gravity group under Eric Adelberger has also been the subject of media attention, most notably a Nature focus article, and an article in the Economist. The torsion pendulum method continues to press on the limits for deviations from Newtonian gravity at the tens of micrometer scale, which might arise if there are extra dimensions beyond the four we know, and for weak couplings to spin, which would be mediated by axions.

Mike Miller, who was our first CENPA Fellow, accepted a leadership position in the company he founded when he was at MIT, Cloudant, and he left us in February, 2012. We wish him every success, and are glad that he remains in the Seattle area. Postdoctoral Fellow Chris Wrede accepted a faculty position at Michigan State and departed in August 2011. We are happy to welcome Diana Parno as a postdoc as of April 2011. Diana took her PhD at Carnegie-Mellon, and did her dissertation work at Jefferson Laboratory. Frederik Wauters from Leuven, Belgium, joined us June 2011 and has been working with the Muon group. Fiscal Specialist Kate Higgins left in the summer of 2011 and we welcomed Bob Shupe, Fiscal Specialist 2, into the front office.

The DOE Office of Nuclear Physics, which provides operating support through programs in Low Energy Nuclear Physics and Heavy Ion Physics, conducted a panel review in Seattle of our 3-year renewal proposal of Grant DE-FG02-97ER41020 for FY12-14. The closeout report of the panel was very positive, and our funding has been renewed with some additional support for the new program in muon physics. The continued support of CENPA by the Office of Nuclear Physics, especially in the current difficult fiscal climate, is greatly appreciated. In the following paragraphs we record some more of the highlights of our past year in research.

- The MuCap experiment released results from its full data set on the determination of the weak-nucleon pseudo-scalar coupling, finding  $g_P = 8.1 \pm 0.5$ . It is the first unambiguous determination, owing in large part to the unique experimental method employed, and is in excellent agreement with the QCD-based prediction of  $8.26 \pm 0.23$ .
- The MuSun experiment completed its first physics data taking using the full cryogenic ultra-pure deuterium-filled Time Projection Chamber and all ancillary measuring equipment. The goal is to measure the  $\mu - d$  capture rate, one of the simplest two-nucleon weak interactions, and from that fix an important low-energy constant, which is common for the treatment of  $pp$  fusion in the sun and neutrino breakup of deuterium.
- We now have the most intense source of  ${}^6\text{He}$  in the world. We have worked on a new determination of the  ${}^6\text{He}$  lifetime and resolved a long-standing discrepancy. We have also succeeded in moving the laser systems from Argonne National Lab and have installed them at UW. We have recently trapped about 30 atoms of  ${}^6\text{He}$  in a Magneto-Optical Trap. The apparatus will be used for searches for Tensor currents in weak decays.
- This year we installed and commissioned the DAQ and slow control systems for SNO+.
- The KATRIN detector system was shipped to KIT and reassembled. Its performance was measured and compared with the original performance at UW. Some differences were investigated, and some troubles identified. Based on these, repairs, improvements, and upgrades are underway.
- Along with the detector system shipping, detector analysis tools were also moved from the UW local environment to the KATRIN standard analysis platform. Taking this opportunity, all the existing programs were reviewed, examined and reorganized into a quality-controlled toolkit for general use by the entire KATRIN group.

- A KATRIN analysis group was formed and it started software development towards a KATRIN integrated analysis platform. The UW group contributed to its fundamental infrastructure design and implementation, took responsibility for detector analysis components, and provided database definitions for the detector section.
- Construction of KamLAND-Zen, a large modification to KamLAND to measure the double-beta decay of  $^{136}\text{Xe}$ , was completed. Successful data taking started in October, 2011, and a measurement of the double-beta decay half-life was published. CENPA Fellow Sanshiro Enomoto had sole responsibility for trigger logic development and event building, also providing technical support for DAQ electronics and software.
- We have set accurate limits on variations of the non-jet quadrupole ( $v_2$ ) source boost with centrality and collision energy in Au-Au collisions. The source boost remains within 2% of the value 0.6 at 200 and 62 GeV and for all measured Au-Au centralities. That result further reduces the likelihood that the quadrupole can be interpreted as a hydro phenomenon (elliptic flow).
- We have measured the non-jet quadrupole amplitude in p-p collisions vs charge multiplicity. The minimum-bias p-p value is consistent with our Au-Au results extrapolated to the peripheral nucleon-nucleon (N-N) limit. We find good agreement with a pQCD  $v_2$  prediction based on a color-dipole model. Such results in p-p collisions are also inconsistent with a hydro interpretation.
- We have examined claims to observe “triangular flow” in Au-Au and Pb-Pb collisions and find that the Fourier method used is actually equivalent to an alternative model for the same-side 2D jet peak. The additional model component is actually not significant for data taken with the STAR TPC. The fitted parameter is consistent with zero within systematic uncertainty.

As always, we encourage outside applications for the use of our facilities. As a convenient reference for potential users, the table on the following page lists the capabilities of our accelerator. For further information, please contact Greg Harper, Associate Director, CENPA, Box 354290, University of Washington, Seattle, WA 98195; (206) 543 4080, or gharper@u.washington.edu. Further information is also available on our web page: <http://www.npl.washington.edu>.

We close this introduction with a reminder that the articles in this report describe work in progress and are not to be regarded as publications nor to be quoted without permission of the authors. In each article the names of the investigators are listed alphabetically, with the primary author underlined in the case of multiple authors, to whom inquiries should be addressed.

Hamish Robertson, Director  
Greg Harper, Associate Director and Editor

Victoria Clarkson, Assistant Editor  
Gary Holman, Technical Editor

## TANDEM VAN DE GRAAFF ACCELERATOR

Our tandem accelerator facility is centered around a High Voltage Engineering Corporation Model FN purchased in 1966 with NSF funds, with operation funded primarily by the U.S. Department of Energy. See W. G. Weitkamp and F. H. Schmidt, "The University of Washington Three Stage Van de Graaff Accelerator," *Nucl. Instrum. Methods* **122**, 65 (1974). The tandem was adapted in 1996 to an (optional) terminal ion source and a non-inclined tube #3, which enables the accelerator to produce high intensity beams of hydrogen and helium isotopes at energies from 100 keV to 7.5 MeV.

Some Available Energy Analyzed Beams

Ion	Max. Current (particle $\mu$ A)	Max. Energy (MeV)	Ion Source
$^1\text{H}$ or $^2\text{H}$	50	18	DEIS or 860
$^3\text{He}$ or $^4\text{He}$	2	27	Double Charge-Exchange Source
$^3\text{He}$ or $^4\text{He}$	30	7.5	Tandem Terminal Source
$^6\text{Li}$ or $^7\text{Li}$	1	36	860
$^{11}\text{B}$	5	54	860
$^{12}\text{C}$ or $^{13}\text{C}$	10	63	860
$^{*14}\text{N}$	1	63	DEIS or 860
$^{16}\text{O}$ or $^{18}\text{O}$	10	72	DEIS or 860
F	10	72	DEIS or 860
* Ca	0.5	99	860
Ni	0.2	99	860
I	0.001	108	860

\*Negative ion is the hydride, dihydride, or trihydride.

Several additional ion species are available including the following: Mg, Al, Si, P, S, Cl, Fe, Cu, Ge, Se, Br and Ag. Less common isotopes are generated from enriched material. We recently have been producing the positive ion beams of the noble gases He, Ne, Ar, and Kr at ion source energies from 10 keV to 100 keV for implantation, in particular the rare isotopes  $^{21}\text{Ne}$  and  $^{36}\text{Ar}$ . We have also produced a separated beam of 15-MeV  $^8\text{B}$  at 6 particles/second.

# Contents

<b>INTRODUCTION</b>	<b>i</b>
<b>1 Neutrino Research</b>	<b>1</b>
<b>KATRIN</b> . . . . .	1
1.1 Overview of the KATRIN experiment . . . . .	1
1.1.1 The status of the KATRIN experiment . . . . .	2
1.1.2 Detector commissioning at UW . . . . .	4
1.1.3 Installation and commissioning at KIT . . . . .	7
1.1.4 Detector system upgrades . . . . .	9
1.1.5 Analysis tools . . . . .	14
1.1.6 Tritium recoil-ion mass spectrometer . . . . .	15
<b>MAJORANA</b> . . . . .	16
1.2 Overview of the MAJORANA DEMONSTRATOR . . . . .	16
1.2.1 Preamplifier with forward biased reset for CoGeNT and MAJORANA . . . . .	17
1.2.2 Cross-talk studies with parylene cables . . . . .	19
1.2.3 MAJORANA single-string test cryostat . . . . .	20
1.2.4 Preparation and shipping of Pb bricks for the MAJORANA shield . . . . .	21
1.2.5 Searches for dark matter with a MAJORANA prototype . . . . .	22
1.2.6 A Monte-Carlo model of the background energy spectrum of the MALBEK detector . . . . .	23
<b>SNO+</b> . . . . .	25
1.3 Overview of the SNO+ experiment and CENPA's contribution . . . . .	25
1.3.1 Commissioning of the SNO+ data acquisition software . . . . .	25
1.3.2 SNO+ detector and slow-control monitoring tools . . . . .	26
1.3.3 Scattering of visible light in liquid scintillator . . . . .	28

<b>Project 8</b> . . . . .	29
1.4 Status of the Project 8 neutrino mass measurement prototype . . . . .	29
<b>HALO</b> . . . . .	30
1.5 The HALO supernova detector . . . . .	30
<b>2 Fundamental symmetries and non-accelerator-based weak interactions</b>	<b>32</b>
<b>Torsion-balance experiments</b> . . . . .	32
2.1 Overview of the CENPA torsion-balance experiments . . . . .	32
2.1.1 Rotating torsion-balance test of the equivalence principle update . . .	33
2.1.2 First data from a hydrogen-rich equivalence-principle pendulum . . .	34
2.1.3 Development of a second-generation hydrogen-rich equivalence-principle pendulum . . . . .	35
2.1.4 Wedge-pendulum test of short-range gravity . . . . .	36
2.1.5 Parallel-plate inverse-square-law test update . . . . .	37
2.1.6 Development of dedicated gravity gradiometer systems . . . . .	39
2.1.7 Progress on the development of a cryogenic torsion balance . . . . .	39
2.1.8 Progress on magnetic shielding for a search for short-range spin-coupled forces . . . . .	40
2.1.9 A precision tiltmeter for advanced LIGO . . . . .	41
2.1.10 Large-dynamic-range autocollimator . . . . .	43
2.1.11 Wireless environmental sensor network . . . . .	44
<b>Non-accelerator-based weak interactions</b> . . . . .	45
2.2 Overview of the CENPA non-accelerator-based weak interactions experiments	45
2.2.1 Status of the UCNA experiment . . . . .	45
2.2.2 UCNA calibration-source foil-thickness measurement . . . . .	46
2.2.3 Mercury electric-dipole-moment experiment . . . . .	47
2.2.4 Search for time-reversal symmetry violation in neutron decay: detailed analysis report on the emiT experiment . . . . .	48

<b>3</b>	<b>Accelerator-based physics</b>	<b>49</b>
	<b>Accelerator-based weak interactions</b> . . . . .	<b>49</b>
3.1	Overview of the ${}^6\text{He}$ experiments at CENPA . . . . .	49
3.1.1	Production of ${}^6\text{He}$ at CENPA . . . . .	49
3.1.2	Precision measurement of the ${}^6\text{He}$ half-life and the weak axial current in nuclei . . . . .	50
3.1.3	${}^6\text{He}$ laser-trap setup . . . . .	52
3.1.4	Investigation of vacuum separation foils with minimal energy loss for $\beta$ particles . . . . .	53
3.2	Experimental validation of the largest calculated isospin-symmetry-breaking effect in a superallowed Fermi decay . . . . .	54
<b>4</b>	<b>Precision muon physics</b>	<b>55</b>
4.1	Overview of the muon physics program . . . . .	55
	<b>MuCap</b> . . . . .	<b>56</b>
4.2	Overview of the MuCap experiment and technique . . . . .	56
4.2.1	Finalized analysis for the singlet capture rate . . . . .	58
4.2.2	Finalized analysis of the molecular rates . . . . .	60
	<b>MuSun</b> . . . . .	<b>61</b>
4.3	Muon capture on deuterium, the MuSun experiment . . . . .	61
4.3.1	The 2011 run . . . . .	63
4.3.2	Hardware development at UW . . . . .	64
4.3.3	Data-analysis progress . . . . .	66
	<b>g-2</b> . . . . .	<b>67</b>
4.4	Overview of the $g - 2$ experiment: physics, technique and project status . .	67
4.4.1	Detector-development laboratory and test-beam run for $g - 2$ . . . . .	69
4.4.2	Current status of cross section measurements via ISR at Belle . . . . .	71

<b>5</b>	<b>Axion searches</b>	<b>73</b>
	<b>ADMX</b> . . . . .	73
5.1	ADMX axion search . . . . .	73
	<b>Axion torsion balance experiment</b> . . . . .	75
5.2	Investigation of upgrades to the axion-search torsion balance . . . . .	75
<b>6</b>	<b>Relativistic Heavy Ions</b>	<b>76</b>
6.1	UW URHI program overview . . . . .	76
6.2	Au-Au azimuth quadrupole source-boost systematics on $(b, \sqrt{s_{NN}})$ . . . . .	78
6.3	Universal parametrization of $v_2\{2D\}(p_t, b, \sqrt{s_{NN}})$ . . . . .	79
6.4	Systematic uncertainties for $v_2\{2D\}(p_t, b, \sqrt{s_{NN}})$ measurements in Au-Au . . . . .	80
6.5	Distinguishing nonjet- and jet-related azimuth quadrupole contributions . . . . .	81
6.6	The sharp transition in minijet characteristics on centrality . . . . .	82
6.7	Uniqueness of the Estruct standard 2D fit model . . . . .	83
6.8	The nonjet quadrupole in 200-GeV p-p collisions: theory vs data . . . . .	84
6.9	Centrality vs $n_{ch}$ in 200-GeV p-p collisions . . . . .	85
6.10	Systematic distinctions between 2D jet structure and the nonjet quadrupole . . . . .	86
6.11	Two-particle correlations in Au-Au collisions at $\sqrt{s_{NN}} = 200, 62, 39, 19, 11$ and 7 GeV . . . . .	87
6.12	Analysis of new tracking code for STAR . . . . .	88
<b>7</b>	<b>Other research</b>	<b>89</b>
	Status of nonlocal quantum communication test . . . . .	89

<b>8</b>	<b>Education</b>	<b>91</b>
8.1	Use of CENPA facilities in education and course work at UW . . . . .	91
8.2	Accelerator-based lab class in nuclear physics . . . . .	91
8.3	Radiochemistry and nuclear-chemistry education program in the UW Department of Chemistry . . . . .	92
8.4	Student training . . . . .	93
<b>9</b>	<b>Facilities</b>	<b>94</b>
9.1	Facilities overview . . . . .	94
9.2	Laboratory computer systems . . . . .	95
9.3	Van de Graaff accelerator and ion source operations and development . . . . .	96
9.4	Electronics shop . . . . .	97
9.5	CENPA instrument shops . . . . .	97
9.6	Building upgrades for ADMX . . . . .	98
<b>10</b>	<b>CENPA Personnel</b>	<b>99</b>
10.1	Faculty . . . . .	99
10.2	CENPA External Advisory Committee . . . . .	99
10.3	Postdoctoral Research Associates . . . . .	100
10.4	Predoctoral Research Associates . . . . .	100
10.5	NSF Research Experience for Undergraduates participants . . . . .	100
10.6	University of Washington graduates taking research credit . . . . .	101
10.7	University of Washington undergraduates taking research credit . . . . .	101
10.8	Professional staff . . . . .	101
10.9	Technical staff . . . . .	102
10.10	Administrative staff . . . . .	102
10.11	Part-time staff and student helpers . . . . .	102

<b>11 Publications</b>	<b>103</b>
11.1 Published papers . . . . .	103
11.2 Papers submitted or to be published 2012 . . . . .	106
11.3 Invited talks, abstracts, and other conference presentations . . . . .	107
11.4 Patents . . . . .	109

# 1 Neutrino Research

## KATRIN

### 1.1 Overview of the KATRIN experiment

J. F. Amsbaugh, J. Barrett<sup>\*</sup>, A. Beglarian<sup>†</sup>, T. Bergmann<sup>†</sup>, L. I. Bodine, N. M. Boyd, T. H. Burritt, T. J. Corona<sup>‡</sup>, P. J. Doe, S. Enomoto, J. Fischer<sup>†</sup>, J. A. Formaggio<sup>\*</sup>, F. M. Fraenkle<sup>‡</sup>, D. L. Furse<sup>\*</sup>, F. Harms<sup>†</sup>, G. C. Harper, M. Knauer<sup>†</sup>, A. Kopmann<sup>†</sup>, E. L. Martin, N. S. Oblath<sup>\*</sup>, D. S. Parno, L. Petzold<sup>†</sup>, D. Phillips<sup>‡</sup>, A. W. P. Poon<sup>§</sup>, R. G. H. Robertson, J. Schwarz<sup>†</sup>, M. Steidl<sup>†</sup>, D. Tcherniakhovski<sup>†</sup>, T. D. Van Wechel, B. A. VanDevender<sup>¶</sup>, B. L. Wall, K. J. Wierman<sup>‡</sup>, J. F. Wilkerson<sup>‡</sup>, and S. Wüstling<sup>†</sup>

The goal of the KATRIN experiment is to make a direct measurement of the neutrino mass by precisely measuring the electron energy spectrum from tritium beta decay. A reduction in the endpoint may be used to extract a value for the neutrino mass. With an ultimate sensitivity of 200 meV, KATRIN represents an order-of-magnitude improvement over current limits and will address the neutrino hierarchy and the reported evidence of a 560-meV indirect measure of the neutrino mass<sup>1</sup>.

The KATRIN collaboration was formed in 2001 and consists of scientists from 5 nations. The experiment is under construction at the Karlsruhe Institute of Technology (KIT), where the Tritium Laboratory Karlsruhe (TLK) provides the necessary expertise and license to handle the large amounts of tritium required for the source. Tritium data taking is expected to begin in early 2015 and to reach full sensitivity after five calendar years.

KATRIN draws on the experience of many earlier neutrino mass tritium beta decay experiments. The apparatus consists of the following chain of primary components: a windowless, gaseous tritium source, an electron transport system, a pair of electrostatic spectrometers and a 148-pixel silicon diode detector. The transport system guides the decay electrons to a pair of electrostatic spectrometers while excluding the tritium gas. The first spectrometer, the pre-spectrometer, is used to reduce the event rate by rejecting electrons below approximately 18.3 keV. The high-energy electrons, whose spectrum would reveal the presence of neutrino mass, pass into the main spectrometer, which, with an expected resolution of 0.93 eV, will make a precise integral measure of the electron spectrum up to the endpoint of 18.6 keV. Electrons passing through the main spectrometer are detected by a multipixel silicon diode array.

---

<sup>\*</sup>Massachusetts Institute of Technology, Cambridge, MA.

<sup>†</sup>Karlsruhe Institute of Technology, Karlsruhe, Germany.

<sup>‡</sup>University of North Carolina, Chapel Hill, NC.

<sup>§</sup>Lawrence Berkeley National Laboratory, Berkeley, CA.

<sup>¶</sup>Pacific Northwest National Laboratory, Richland, WA.

<sup>1</sup>H. V. Klapdor-Kleingrothaus, I. V. Krivosheina, A. Dietz, and O. Chkvorets, Phys. Lett. B **586**, 198 (2004).

### 1.1.1 The status of the KATRIN experiment

P. J. Doe

The primary US contribution to KATRIN is the main detection system. The University of Washington (UW) is the lead institute, in collaboration with the Massachusetts Institute of Technology (MIT) and the University of North Carolina (UNC), which also has responsibility for the data acquisition system (DAQ). The University of California Santa Barbara (UCSB) is designing and providing part of the source rear system, an important diagnostic tool for KATRIN. MIT is also leading the experiment simulation team while the Lawrence Berkeley Laboratory is leading the analysis team. In May 2011, the US KATRIN program underwent a successful CD-4-type review, and enters a phase of commissioning at Karlsruhe.

The layout of the KATRIN apparatus<sup>1</sup> can be seen in Fig. 1.1.1-1.

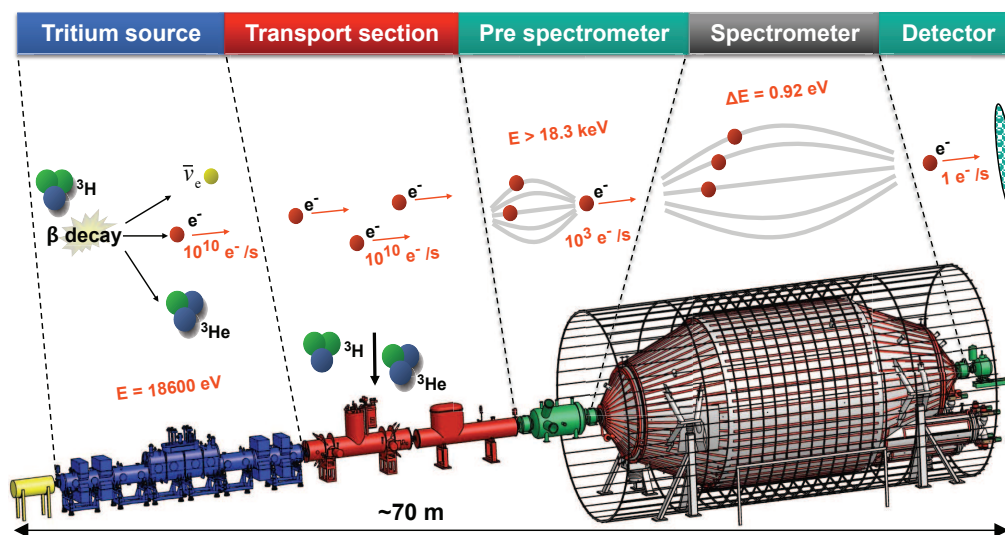


Figure 1.1.1-1. Layout of the KATRIN experiment showing the principal components. Also shown is the electron flux through each stage of the apparatus.

Starting from the rear system of the source, the status of the main KATRIN components is as follows:

- *Rear section:* Led by UCSB, the design of the rear section is almost complete. The rear wall of this system establishes the potential of the intensely active tritium source. The rear section also provides a steerable, mono-energetic electron gun. Electrons from this gun travel from the source to the detector, providing diagnostics for the entire chain of KATRIN components. A design review of the rear section is scheduled for May, 2012, after which construction is expected to begin.

<sup>1</sup>KATRIN Design Report 2004, NPI ASCR Rez EXP-01/2005.

- *KATRIN magnet system*: The electron path from the tritium source is guided through the transport system to the spectrometers, consisting of a long chain of superconducting magnets. These magnets have essentially identical design configurations and were intended to run in the persistent mode. Failure of the protection diodes during tests of the transport system (see below) revealed common design flaws in the selection and mounting of the diodes. Furthermore, the magnet design did not allow for easy replacement of failed diodes. With significant leadership from KIT, the manufacturers have provided an improved design that allows replacement of any failed diodes. In addition KIT has contracted with the Saclay Laboratory to investigate the performance of the magnets in the driven mode, i.e. continuously connected to the power supplies. These tests are ongoing with encouraging initial results. If successful, all source and transport magnets will be run in the driven mode.
- *Windowless gaseous tritium source (WGTS)*: After successfully demonstrating that the inner chamber containing the tritium gas can maintain a temperature of  $27 \pm 0.03$  K, the demonstrator was shipped back to the manufacturer for mating to the magnet chain. These magnets are being modified as described above. Final assembly of the WGTS will take place at KIT and is expected to be complete in April, 2014. Commissioning with tritium is expected to take approximately one year. This sets the critical path for the KATRIN experiment.
- *Transport section*: The transport section consists of two parts, the differential pumping system (DPS) and the cryogenic pumping system (CPS). The DPS, which includes an array of turbo pumps that return tritium gas to the source, was delivered to KIT in 2010. After successfully passing the cryogenic and vacuum tests the magnet chain was energized. This resulted in a quench and failed diodes leading to the redesign of the entire magnet chain in the source and transport system (see above). Since the CPS shares many design features with the DPS its magnet system will also be modified to enable the diodes to be replaced and to run in the driven mode. The modified CPS is expected to be delivered to KIT in early 2014 with commissioning to be completed in August, 2014.
- *Spectrometers*: In 2006, the pre-spectrometer (PS) was delivered to KIT. Along with its UW-supplied internal wire electrodes it has proved to be invaluable in guiding the design of the main spectrometer. The PS has now been moved to the KATRIN spectrometer hall and is ready to be attached to the main spectrometer (MS). The MS has seen intense activity over the past year with the installation of the internal wire-electrode system. With this technological tour de force now successfully completed, the process of closing the spectrometer and baking it out has now begun. Commissioning of the main spectrometer is expected to begin in August, 2012, and to take about one year of 24/7 operation. To ensure the stability of the retarding potential of the MS, a monitoring spectrometer has been commissioned using the refurbished Mainz spectrometer<sup>1</sup>. This spectrometer shares the same high-stability potential supply as the MS and, by monitoring the line from a  $^{83m}\text{Kr}$  source, functions as a high-precision voltmeter.

---

<sup>1</sup>Kraus, Ch, *et al.*, Eur. Phys. J. **C40**, (2005) 447-468, arXiv:hep-ex/0412056.

- *Main spectrometer beam-line valves:* Vacuum-conditioning the main spectrometer by pumping it down and baking it out in order to achieve pressures of  $10^{-11}$  mbar takes several months. To avoid contaminating the main spectrometer should it prove necessary to remove either the detector or the pre-spectrometer, the UW designed and manufactured custom in-beam valves positioned at each end of the main spectrometer. These valves may be closed to allow the removal of either the detector system or the pre-spectrometer without contaminating the interior of the main spectrometer with air.
- *Detector:* Commissioning of the detector system at UW was completed in April, 2011, and by June, 2011, 7.5 tons of hardware was ready for installation at KIT. Installation and commissioning was completed by February, 2012. A valuable understanding of the system was achieved during this installation and commissioning process. The appearance of a fundamental flaw in both the detector and pinch magnet was traced back to drift in the helium pressure sensors. These sensors have been replaced. A continuing struggle with the performance of the electronics was finally traced to a choice of voltage regulators, mechanical assembly, and errors in the cable harness. To avoid this type of problem in the future a complete bench-test assembly has been built to test the entire set of readout electronics before installation into the system. Currently this is being used to commission a new set of electronics which includes lower noise FETs prior to installing them as a system upgrade. As a result of the KIT commissioning exercise several other system upgrades have been identified and are being implemented. In addition to the electronics upgrade these include a strengthened post-acceleration electrode, reduction of radioactive background, improved electronics cooling, and improved flux-tube alignment. These upgrades will be complete in June, 2012.

Commissioning of the main spectrometer will begin in August, 2012, and the detector system will be required beginning September, 2012. The commissioning group has received a total of 30 experimental proposals, requiring a wide range of operating and performance parameters. To optimize the setup and execution of these experiments, UW has developed a set of near-time analysis tools that perform initial analysis and visualization of the data. Prior to the start of MS commissioning UW will be offering training in detector operation and near-time data analysis.

### 1.1.2 Detector commissioning at UW

E.L. Martin and B.L. Wall

The KATRIN focal-plane detector system was commissioned at the University of Washington prior to being disassembled and shipped to the Karlsruhe Institute of Technology. While the system met its overall commissioning goal for the figure of demerit, and all subsystems were deemed suitable for commissioning, some upgrades are planned during installation at KIT.

The figure of demerit ( $F$ ) measures the effect of the detector on the uncertainty in the neutrino mass measurement. For the full KATRIN setup, the commissioning goal is  $F \leq 1.2$ .

$$\sigma(m_\nu^2) = k \frac{b_{ms}^{1/6}}{r^{2/3} t^{1/2}} F$$

$$F = \frac{(f(\Delta E) + \frac{b_{det}(\Delta E)}{b_{ms}})^{1/6}}{f(\Delta E)^{2/3}} \geq 1$$

Here,  $k = (\frac{16}{27})^{1/6}$ ,  $t$  is time,  $r$  is the total count rate from the main spectrometer,  $b$  is the background rate, and  $f$  is the detector response. Detector response and background depend on the region of interest, so  $F$  is minimized by adjusting the region of interest.

$F$  was determined to be 1.119 for a region of interest between 14.6 keV and 20.3 keV, after applying muon veto and multi-pixel cuts, but without post-acceleration voltage. Data with post-acceleration voltage were taken to determine the effect on  $F$ , but low-energy electrons emitted from the rear blank-off flange were accelerated by the post-acceleration voltage and worsened the figure of demerit. This flange will not be present when the detector is installed in the final setup. Using the background without post-acceleration voltage and the detector response with post-acceleration voltage,  $F$  was estimated at 1.111 for 12 kV of post-acceleration without the rear blank-off flange.

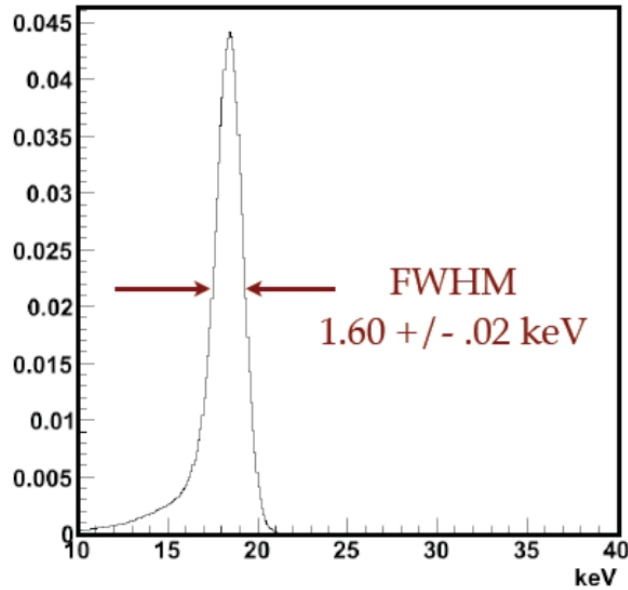


Figure 1.1.2-1. Measured spectrum for 18.6 keV electrons over the 131 working channels.

Of the 148 pixels on the focal plane detector 131 were usable during commissioning at UW, which is slightly below the commissioning goal of 90% working channels. However, the bad channels can be attributed to bad preamplifier modules and a bad connection on the cable harness. It is believed that the focal plane detector itself was fully functional and 100% working channels can be attained by correcting electronics problems during commissioning at KIT.

Detection efficiency was determined to be better than 95% for the working channels, by comparing the detector hit rate to the current from the electron source and correcting for cross-talk and dead channels. The measured efficiency meets the 90% detection efficiency goal.

The linearity was measured to be 0.3% r.m.s., which was mostly attributed to a non-linearity in the Agilent 33220A waveform generator between different output ranges, as evidenced by a step in the linearity curve at the point the waveform generator changed ranges. Linearity is not a concern for detecting electrons from tritium beta decay, but is a concern for determining the dead layer of the focal plane detector.

Timing resolution was measured to be 89.9 ns standard deviation for a 3.2  $\mu$ s shaping length, which meets the specifications of 212 ns for normal operation. Adding 10 kV of post-acceleration potential and reducing the shaping time to 1.6  $\mu$ s improved the timing resolution to 45.9 ns, which may be useful for time-of-flight measurements.

For 18.6-keV electrons, corresponding to the end-point energy for electrons from tritium  $\beta$  decay, detector energy resolution was measured to be 1.60 keV FWHM (see Fig. 1.1.2-1). The engineering goal was 1 keV FWHM but this is not a specification as it is instead tied in to the figure of demerit along with background.

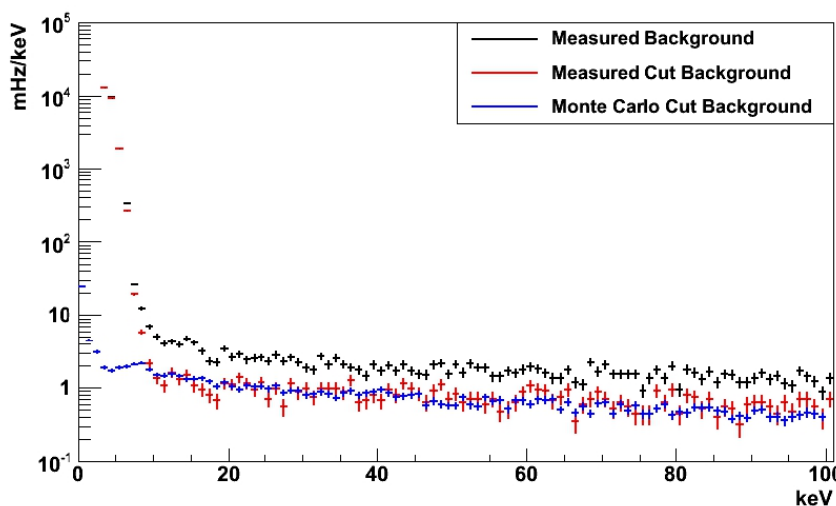


Figure 1.1.2-2. Simulated and measured background spectra at the University of Washington.

The engineering goal for background was  $\leq 1$  mHz in the region of interest, but measured background in the region of interest was 5.4 mHz (see Fig. 1.1.2-2). This is due to optimization of the figure of demerit favoring high efficiency and a large region of interest over low background. Background in the region of interest is expected to be 1.2 mHz with 10 kV of post-acceleration once the rear blank-off flange is removed.

Pressures in the high-vacuum and extreme-high-vacuum systems were measured down to  $3 \times 10^{-7}$  mbar and  $7 \times 10^{-10}$  mbar respectively, meeting the design specifications of  $1 \times 10^{-6}$  mbar and  $1 \times 10^{-9}$  mbar.

The post-acceleration electrode design goal was 30 kV but it was only able to attain 12 kV before breakdowns occurred. While investigation into the cause of the breakdowns is ongoing, the system still meets the minimum performance specification of 1 kV. The post-acceleration electrode previously deformed by about 1 cm under differential pressure stress. After several pressure cycles the creep rate was found to be negligible and the post-acceleration electrode was used for commissioning (see Sec. 1.1.4).

The detector-section magnets were measured to drift less than 200 ppb/hr, well under the design goal of 0.1% per month (1 ppm/hr). Both were able to reach 6 T.

The veto mode was not yet implemented on the DAQ system, but offline veto cuts were performed on the data.

### 1.1.3 Installation and commissioning at KIT

L. I. Bodine and D. S. Parno

In May and June of 2011, we disassembled the focal plane detector (FPD) system and shipped it to Karlsruhe in 21 crates with a gross weight of 7400 kg. Seventeen crates or pallets were custom-built by Commercial Crating, Ltd; the others were the original crates from the manufacturers. The goods were transported via air-ride trucks and airplanes under the management of Expeditors International. Excluding the labor of CENPA personnel, the operation cost about \$40,000.

Inside the crates each item was protected by some combination of foam, bubble wrap, stretch wrap, anti-static bags, and internal wooden blocking. On uncrating at KIT we observed only two instances of new damage, both to the magnets. The standoff for the detector-magnet pulse tube cooler rotary valve broke at the weld joint causing stress in the helium lines. The standoff was repaired and no subsequent issues were observed. The indium-seal pinch-magnet fill-line feedthrough was shaken loose causing a leak in the helium space. The seal was remade with additional indium and remains leak-tight.

Some items were sent separately. The DN250 gate valve was sent to the manufacturer for repairs and then shipped to KIT from there. The PULCINELLA electronics and photoelectron disk were held for improvements and sent via FedEx later in the summer. The  $^{241}\text{Am}$  calibration source was sent to MIT, its owner of record, for shipment to Karlsruhe.

The FPD system was installed on the detector platform of the KATRIN spectrometer hall from June to October of 2011. CENPA personnel led this effort while training KIT personnel in installation, operation, and maintenance. The system required some adaptation to its new environment. Among other factors, the voltage and frequency of the mains power changed, as did the height of the rails on which the system rests. The performance of the cooling and vacuum systems is comparable to that attained in the UW setup but the in-vacuum electronics run about 5° C hotter than at UW, probably due to variations in the assembly of the thermal conduction chain. The post-acceleration electrode can maintain a stable potential of up to 9 kV. Due to delays sending the strong  $^{241}\text{Am}$  calibration source

from MIT to KIT,  $\gamma$  calibration must be performed with a borrowed source that is much weaker, and a full calibration thus takes two days instead of two hours. Improvements to the illumination assembly for the photoelectron source and to PULCINELLA are ongoing. We are also integrating our analysis software (see Sec. 1.1.5) and slow-controls systems with the KATRIN database and software frameworks.

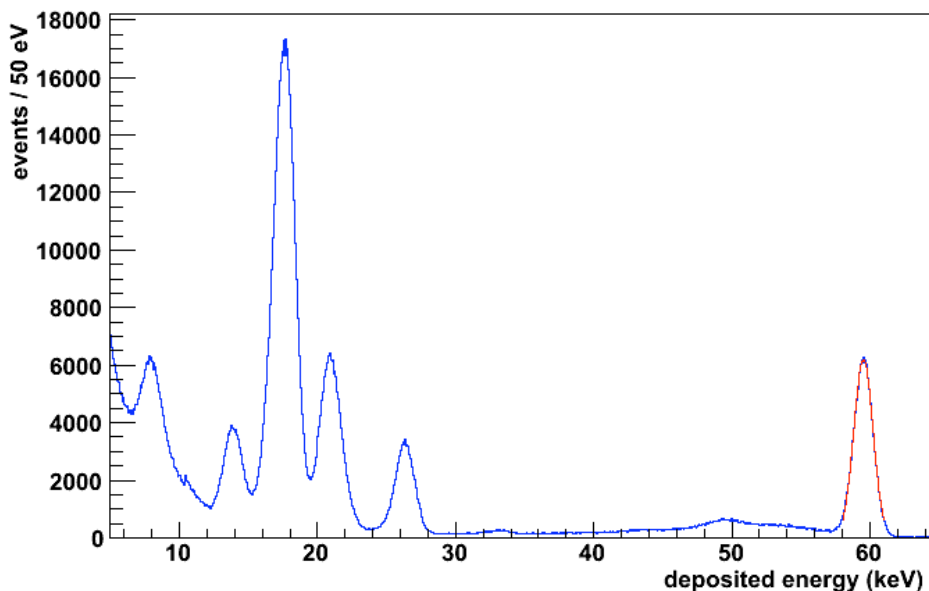


Figure 1.1.3-1.  $^{241}\text{Am}$   $\gamma$  spectrum, averaged over 128 working signal channels measured at KIT with a weak source. A fit to the 60-keV line is shown in red. The corresponding energy resolution is  $1.637 \pm 0.004$  keV (FWHM).

A new set of in-vacuum readout electronics was installed at KIT in the fall. As Fig. 1.1.3-1 shows, we achieved an energy resolution comparable to the setup at UW. Due to wiring and mechanical problems in the new cable harness, however, the system was commissioned with slightly fewer working signal channels.

The magnets have been successfully run with 6 T at the center of each magnet, and KIT personnel have been independently operating them since October, 2011. During the first ramp of the magnet pair at KIT a training quench occurred in the detector magnet when both magnets reached 6 T. The magnet was recooled and both magnets were ramped to 6 T without further incident. Axial and radial field scans with Hall probes show the magnetic axis is within 2 mm of the mechanical axis as measured at the manufacturer and at UW. NMR probe measurements show magnetic drift of  $10^{-5}$  over 30 days, well within the specification of 0.1% per month.

The liquid-helium-level sensors do not operate correctly in the KIT lab environment where they intermittently pump large amounts of heat into the cryostat. This has caused cryogen boiloff, including a full loss of liquid helium in the detector magnet. The microprocessors on the units appear to be susceptible to damage. After several returns to the manufacturer the issue is still being investigated. At present, the level sensors are used intermittently to confirm no boiloff has occurred.

The helium recondenser controller units, which are designed to maintain positive pressure in the vessels, also malfunctioned. The pressure-sensor calibrations drift on a several-day time scale causing an apparent drop in the vessel pressure and unnecessary concern over cryostat performance. To provide robust measurements, additional pressure sensors were installed. A separate control system is being constructed within ZEUS slow controls.

Small leaks in the magnet cryostats were fixed by replacing degraded O-rings on the quench relief valves and removing unnecessary low-pressure relief valves. Permanent magnet stands were constructed for easy access to the necessary cryostat hardware.

The entire system is currently being disassembled for upgrades (see Sec. 1.1.4) prior to main-spectrometer commissioning.

#### 1.1.4 Detector system upgrades

J. F. Amsbaugh, N. M. Boyd, P. J. Doe, S. Enomoto, and R. G. H. Robertson

##### *Electronics*

A noise waveform analysis with the UW detector setup showed that the detector energy resolution is basically determined solely by noise, and at an optimal shaping length of 6.4  $\mu$ s a large fraction of the noise originates from the white and 1/f noise of the FET.

A lower-noise FET, BF862 from Philips Semiconductor, was tested at CENPA with test preamplifier cards that mount the new FET on half of the channels of a card. With this a  $\sim 40\%$  reduction of white noise was observed. The reduction of the white noise not only improves the energy resolution, but also improves the timing resolution because of both the lower noise and a shorter optimal shaping length.

Based on this result a full set of new preamplifier cards with the low noise FET have been produced by the IPE group at KIT. At the same time some minor modifications were also made for troubles observed during the detector re-commissioning at KIT this year, such as oscillations and abnormally large noise, which were later identified as caused by insufficient supply voltages and possibly faulty voltage regulators.

A complete replica of the detector electronics and DAQ system, *Iron Bird*, was constructed by the IPE group. This is now being used for testing and characterizing the entire system, including the new preamplifier cards, prior to scheduled installation into the detector.

##### *Reduction of background from glass feedthroughs*

Materials with low radioactivity have been used throughout the KATRIN detector system in order to minimize backgrounds. The detector pixels in the ultra-high vacuum are electrically connected to preamps in the high-vacuum system via a custom multipin feedthrough flange made by Ametek with Inconel pins passing through glass seals in an Inconel plate. The glass contains only about 1 ppm each of U and Th but is relatively high in potassium, 3.6(1)% by weight, and thus contributes to detector background. Because the detector is thin and made

of low- $Z$  material, it is not the  $\gamma$ s but rather the  $\beta$ s that are most important. In the presence of the nominal 3.6-T magnetic field, the  $\beta$ s from the glass seals follow field lines and travel from the seal to the associated detector pixel (Fig. 1.1.4-1).

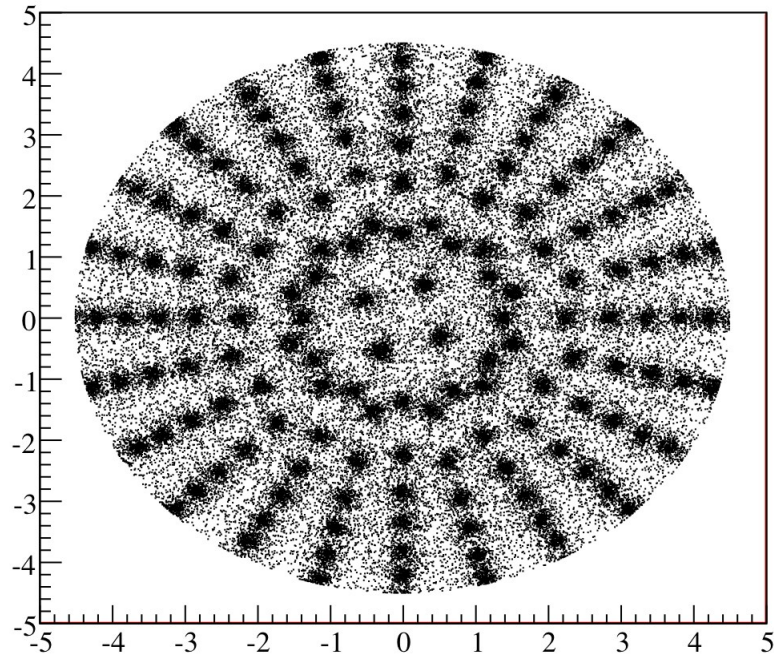


Figure 1.1.4-1. GEANT-4 simulation showing background in the silicon detector for KATRIN. The concentration of events around each pin is caused by the potassium content of the glass in the feedthrough seals. The axes are in cm. Calculation by Michelle Leber.

To intercept the  $\beta$ s before they strike the detector, small copper cylinders (dubbed ‘donuts’) 3.2 mm high and 3.5 mm in diameter have been machined to fit tightly on the pogo-pin interface adapters, which are themselves small connectors that slip over the Inconel feedthrough pins. It is expected that the donuts will reduce the background contribution of 0.06 mHz (in the GEANT simulation) by at least an order of magnitude, to negligible levels. There is a concomitant increase in capacitance, but the effect on the preamp series noise is at the percent level and the effect on crosstalk is parts in  $10^4$ .

#### *Heat pipe cooling system*

The focal plane detector is cooled by a single-stage pulse tube cryocooler<sup>1</sup>. The cryocooler’s specified heat removal-rate at 80 K is 60 W for 60 Hz operation (50 W for 50 Hz). The expected heat load is about 25-35 W depending on the ultimate temperature achieved. Since the cryocooler cannot tolerate high magnetic fields, it is mounted 1.2 m from the magnetic axis and is thermally connected via a 2.5-cm diameter, 0.760-m long copper cold finger and 25 flexible braids. We have designed a nitrogen-filled heat pipe to replace the cold finger,

<sup>1</sup>Model PT-60 UL/ CP830, Cryomech Inc., Syracuse, NY.

braids, and their mechanical thermal joints to eliminate the significant thermal resistance. A prototype has been built using a minimum 60-W heat-removal rate as the design requirement and we are currently testing it.

The heat pipe consists of a condenser, a 0.78-m long adiabatic section, and an evaporator. The evaporator is connected to a heat-load plate. The condenser is a slitted copper cone bolted to the cold flange of the PT-60. Condensed nitrogen flows down the cone and drips into a 3-mm diameter stainless steel tube centered in a 25-mm tube, which is the adiabatic region of the heat pipe. The smaller tube delivers liquid to the evaporator. The nitrogen vapor returns to the condenser in the space between the tubes at a velocity less than 0.16 m/s. Assuming complete immersion and a heat flux rate of  $6200 \text{ W/m}^2$ , the evaporator's area of  $0.0108 \text{ m}^2$  is large enough to support a 60-W boiling rate. This heat flux rate is the film boiling minimum measured in a study of a stainless steel block immersed in liquid nitrogen<sup>1</sup>. A spiral tube with low thermal conductance connects the condenser to an external tank at room temperature. The total  $\text{N}_2$  volume is 4.1 L, of which 0.36 L is the heat pipe and 3.7 L is the tank. The system is evacuated and filled with 4.7 grams of  $\text{N}_2$  (1015 mbar nitrogen at 295 K). The system includes a  $\text{N}_2$  gas pressure sensor<sup>2</sup> mounted near the tank

and platinum resistance temperature sensors bolted on the condenser, evaporator, and test heat load plate. A silicon diode temperature sensor and six power resistors are also mounted on the test load plate. Two power resistors are installed on the condenser. The prototype was installed without any superinsulation on the CENPA e-gun vacuum chamber since the PT-60 cooling rate easily removes the heat load from black-body radiation. The ORCA script and

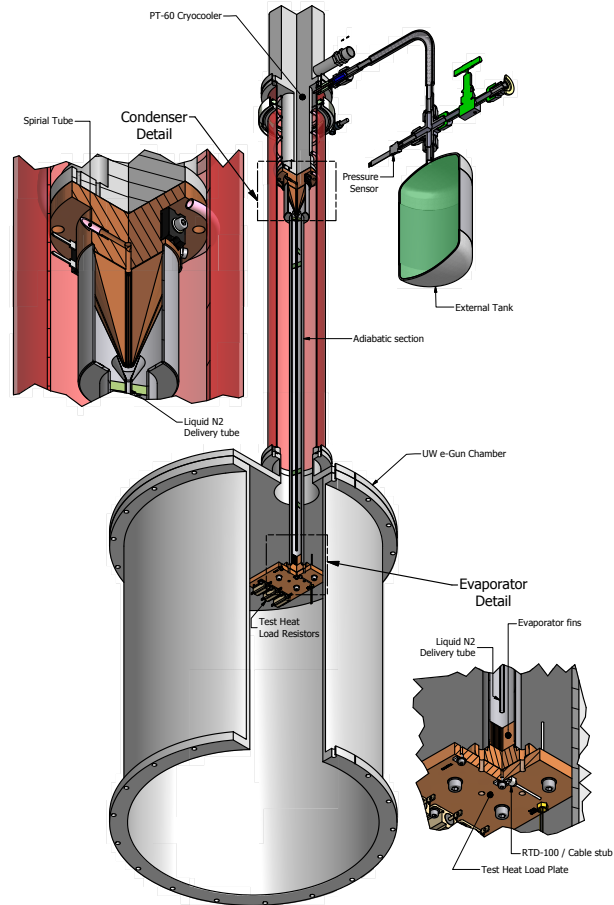


Figure 1.1.4-2. 3/4 section of heat pipe prototype installed in UW e-gun chamber with condenser and evaporator details.

<sup>1</sup>Tao Jin, Jian-ping Hong, Hao Zheng, Ke Tang, Zhi-hua Gan, Journal of Zhejiang University SCIENCE A 2009 10(5):691-696.

<sup>2</sup>Honeywell 19C015PA4K, available from Digikey Corp., Thief River Falls, MN.

electronics originally used for the UW detector commissioning tests<sup>1</sup> were adapted in order to monitor the pressure and temperature.

In Fig. 1.1.4-3, one can clearly see the various stages of cooling. The initial nitrogen gas pressure of 1015 mbar falls to 996 mbar as the gas and adiabatic section are inefficiently cooled. When condensation begins after 15 minutes, the pressure drops rapidly as the condenser temperature approaches 77 K (point A in Fig. 1.1.4-3). Once liquid has cooled the delivery tube and passes down the adiabatic section, the evaporator and test plate begin to cool. Since this initial test does not have a heat load at the evaporator, which would simulate the standing loads of the apparatus, the evaporator and test plate cool quickly. As the temperature of the evaporator enters the realm of liquid-nitrogen film boiling (Fig. 1.1.4-3 point B), the increased heat-transfer rate cools it to the liquefaction point, which reduces boiling. The reduced condensation rate allows the condenser temperature to reach the nitrogen freezing point. All the nitrogen freezes within minutes as can be inferred from the plummeting pressure. Once the heat pipe ceases transferring heat, the evaporator and test plate steadily warm (Fig. 1.1.4-3 points B to C). Approximately 100 W of condenser heating is required to overcome the PT-60 cooling and raise the temperature enough to melt the nitrogen. As the nitrogen melts, the pressure rises, the heat of fusion warms the condenser, and the melt cools the evaporator and test plate (Fig. 1.1.4-3 points C to D).

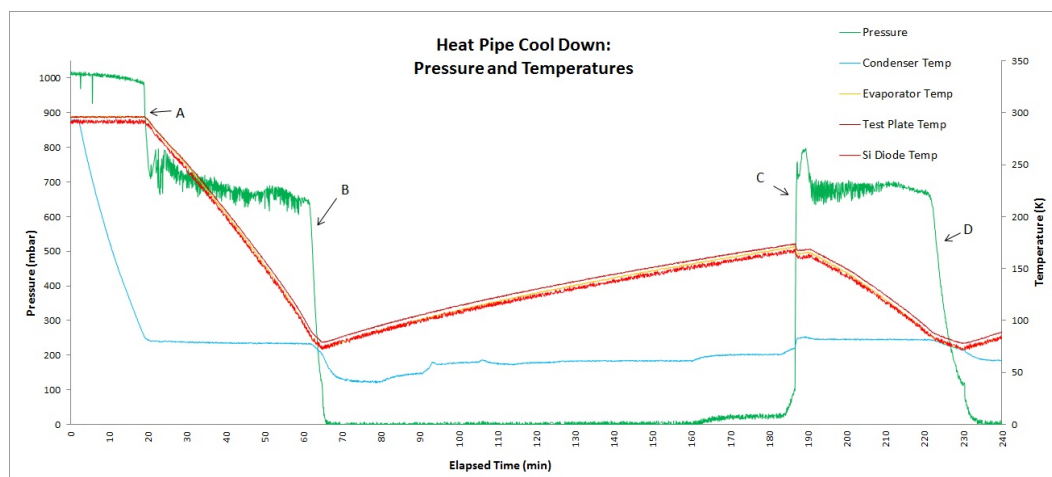


Figure 1.1.4-3. Heat pipe data acquired on 11 April, 2012, for the initial test showing the start of  $N_2$  condensation (point A),  $N_2$  freezing (points B,D) and  $N_2$  melting (point C). The various heaters were controlled manually.

An automatically tuning PID temperature controller<sup>2</sup> will be used to control the condenser temperature and prevent nitrogen freeze-out. We will determine whether regulating temperature, pressure, or both is necessary for system stability. In an initial test with 64.8 W of condenser heating, the heat pipe removed a 15-W heat load from the test plate for a period of 25 minutes, without regulation. The nitrogen pressure was 660 mbar, and the temperature of the evaporator was 100 K with a 4% downward trend. This demonstrates the heater power

<sup>1</sup>CENPA Annual Report, University of Washington (2009) p. 16.

<sup>2</sup>Model CNI16D22-EI, Omega Engineering Inc., Stamford, CT.

required for control. Further analysis will compare the performance of the heat pipe with the existing copper rod assembly using appropriate test heat loads to approximate the actual apparatus. We are currently modifying the design aspects of the heat pipe that are specific to the UW e-gun setup so that this apparatus can be installed at KIT.

*Post-acceleration electrode*

Should low-energy backgrounds prove to be a problem the detector system has the ability to raise the signal above these backgrounds by floating the detector and readout electronics to a high potential using one of the electrodes shown in Fig. 1.1.4-4



Figure 1.1.4-4. The new (left) and the old (right) post-acceleration electrodes. Sensors and hardware are being transferred to the new electrode prior to installation into the vacuum chamber at KIT. The deformed thermal break can be seen outside the white ceramic insulator at the base of the old electrode.

The post-acceleration electrode has to satisfy a number of criteria. It must withstand a potential of up to 25 kV, it must conduct away the heat from the detector front end electronics, and it must be able to tolerate approximately 1 ton of atmospheric loading should the vacuum in the electronics space be brought up to atmosphere. During vacuum testing the atmospheric loading caused the stainless steel thermal break to deform. Investigation revealed that the spinning process used to manufacture the component caused the material to be thinned beyond specification. A new thermal break was designed and tested and is now used in the replacement post-acceleration electrode currently being installed in the detector system.

### 1.1.5 Analysis tools

S. Enomoto

Along with the detector system shipping from UW to KIT, all the detector analysis software was moved from the UW local environment to the KATRIN standard analysis platform. The KATRIN analysis platform currently under active development is an integrated environment for all the KATRIN software including data access, analysis, and simulation. It provides a single-point interface to all collected data. The data interface of the new analysis platform is quite different from the one used for the UW detector commissioning and virtually all the detector analysis programs had to be re-written according to the new platform design.

The existing analysis tools developed for the UW detector commissioning were, although providing quite comprehensive coverage of all necessary tasks, a random collection of single-purpose programs written by various people and not suitable for general use by the entire KATRIN group. We took the opportunity of re-writing everything for the new platform to re-organize the collection into general KATRIN analysis tools.

Many of the existing programs were written for single use during the detector commissioning. In contrast, the new analysis tools were designed for general use by various one-time commissioning analyses (mostly for trouble-shooting), near-time analyses during various KATRIN measurements (mostly for monitoring purposes), routine analyses for normal KATRIN operation (calibration, data processing, etc.), and the final neutrino mass analysis. Former applications generally require quick turnaround for various conditions, while latter applications tend to grow steadily. To meet both requirements at the same time without source code modification, we developed a simple and flexible scheme of detector data analysis, namely, building analysis sequences by dynamically combining configurable analysis task elements. Sequences can be built with a GUI by dragging and dropping of elements, and result plots will be obtained on the fly, which is suitable for quick-and-dirty applications. Sequences can also be described programmatically, with customized analysis elements if necessary, and users can do further analysis on the sequence execution results within the same program, which is suitable for higher level analyses.

The KAFFEE automation tool, originally developed to automate routine software tasks of the UW detector commissioning, was extended for general software workflow automation and also for interactive operation on the workflow. The interactive operation extension will be particularly useful for near-time analysis if combined with the on-the-fly analysis sequence construction of the new analysis tools. The workflow automation can be used for the general data analysis chain by end users, as well as programmed automatic analysis for routine data collection and processing, such as for calibration runs.

### 1.1.6 Tritium recoil-ion mass spectrometer

L. I. Bodine, D. S. Parno, and R. G. H. Robertson

The Tritium Recoil-Ion Mass Spectrometer (TRIMS) experiment is designed to measure the  $T_2$   $\beta$  decay branching ratio to the bound molecular ion  ${}^3\text{HeT}^+$ . This branching ratio is a litmus test of the molecular final state distribution used in the KATRIN analysis. The numerical calculations of Saenz, *et al.*<sup>1</sup>, are in stark disagreement with the measured branching ratios of Snell, *et al.*<sup>2</sup>, and Wexler<sup>3</sup>. The discrepancy must be resolved to provide confidence in the molecular models used in KATRIN.

The TRIMS apparatus consists of a time-of-flight mass spectrometer with a pair of silicon detectors at each end: one for  $\beta$  detection and one for ion detection. The spectrometer is filled with high-purity molecular tritium gas at a pressure of  $\sim 10^{-7}$  mbar. A potential difference of  $\sim 50$  kV is maintained between the two detectors for accelerating the ions and  $\beta$ s above detection threshold. An axial magnetic field of  $\sim 0.2$  T guides the charged particles to the detectors.

The signal consists of the prompt  $\beta$  charge pulse and a time-delayed recoil-ion charge pulse. The relative timing of the pulses depends on the longitudinal location of the decay and on the ion mass. Since all ions produced in the decay have low energy, their kinetic energy upon arrival at the detector is fixed by the location of the decay relative to the ion detector. Combining the time-of-flight and energy information allows for determination of the ion mass and hence the branching ratio to the bound ion.

The preliminary design has been completed and is currently under review. A tritium-compatible ultra-high vacuum system has been designed. The magnetic field will be provided by four copper coils operated in a double Helmholtz setup. Low-leakage-current, 45-mm<sup>2</sup> versions of the Canberra PIPS silicon detectors have been ordered. Custom front-end electronics are being designed by the CENPA Electronics Shop. Much of the hardware is being recovered from previous generations of experiments, including the vacuum pumps and two magnet coils.

A TRIMS simulation was written using the ROOT framework and Stopping Radiation in Matter software<sup>4</sup>. Initial simulations show adequate separation of the mass peaks in the energy vs time of flight spectrum for reasonable experimental parameters and resolutions. The simulations were essential in tuning the experimental design.

---

<sup>1</sup>Alejandro Saenz, Svante Jonsell and Piotr Froelich, Phys. Rev. Lett. **84**, 242-245 (2000).

<sup>2</sup>Arthur H. Snell, Frances Pleasanton and H. E. Leming, J. Inorg. Nucl. Chem. **5**, 112-117 (1957).

<sup>3</sup>S. Wexler, J. Inorg. Nucl. Chem. **10**, 8-16 (1958).

<sup>4</sup>James F. Ziegler, Nucl. Instr. Meth. B **219-220**, 1027-1036 (2004).

## MAJORANA

### 1.2 Overview of the MAJORANA DEMONSTRATOR

J. F. Amsbaugh, N. M. Boyd, T. H. Burritt, P. J. Doe, G. C. Harper, A. Knecht,  
 J. Leon, M. L. Miller\*, J. D. Mulligan, D. A. Peterson, R. G. H. Robertson,  
 A. G. Schubert, T. D. Van Wechel, J. F. Wilkerson<sup>†</sup>, and D. I. Will

The MAJORANA collaboration is performing the necessary R&D towards building a 1-tonne array of enriched  $^{76}\text{Ge}$  detectors capable of searching for neutrinoless double beta decay ( $0\nu\beta\beta$ ) in the inverted mass hierarchy region ( $\sim 30$  meV). A first step is the construction of the MAJORANA DEMONSTRATOR, a detector array consisting of 40 kg of germanium detectors of which up to 30 kg are enriched. This will address all the technical challenges on the way towards a 1-tonne experiment. The goals of the demonstrator are: (i) the achievement of a radioactive background of 4 counts/tonne/year around the 4 keV region of interest, (ii) testing a claim of  $0\nu\beta\beta$  detection<sup>1</sup>, (iii) successful long-term operation, and (iv) alternate low-energy physics measurements such as the search for low-mass dark matter particles.

The project is at a very exciting stage as the first prototype module will be operational underground by the end of this year. Occupancy at the 4850-foot level at the Sanford Underground Research Facility (SURF) has started and more and more equipment is currently being brought underground. The collaboration passed CD-2 in the past year and is currently preparing for CD-3.

The MAJORANA group at the University of Washington is contributing to the effort on several levels:

- We have extracted 3500 lead bricks (approximately 50 tonnes) from a decommissioned laboratory at the University of Washington. The bricks were carefully packaged, hoisted up to the ground and shipped in 2.5 truck loads to Black Hills State University, SD for further cleaning. They will form the innermost layer of the lead shield surrounding the detectors.
- Using the expertise of our technical staff the MAJORANA single-string test cryostats were designed and built at CENPA. Two of a total of 7 have been constructed and delivered to Los Alamos.
- Our technical staff has been actively involved in the machining of electroformed mandrels both here at our shop at CENPA and in the newly built workshop in Rapid City, SD, dedicated to low-background machining. In addition, many design challenges within the collaboration profit from their expertise.

---

\*Presently at Cloudant, Inc., Seattle, WA.

<sup>†</sup>University of North Carolina, Chapel Hill, NC.

<sup>1</sup>H. V. Klapdor-Kleingrothaus, I. V. Krivosheina, A. Dietz, and O. Chkvorets, Phys. Lett. B **586**, 198 (2004).

- Over the past years we have developed low-background parylene cables<sup>1</sup> to connect to the sensitive germanium detectors. As they currently do not meet the electrical requirements of the preamplifiers to be used in the first stages, a commercial option has been chosen and is currently being evaluated. At later stages, however, parylene cables could again be used and so we continue our R&D and tests of such cables.
- We have updated the design of our connectors<sup>1</sup> to adapt to the commercial cables. A first batch is currently under construction and will be used for tests at UW and LBNL and, later, in the string test cryostats. The construction of the connectors for the prototype module will start soon.
- Benefiting from our parylene know-how we have fabricated low-background parylene gaskets that will be used to seal the detector cryostats.
- Part of the UW MAJORANA group is engaged in the CoGeNT (Coherent Germanium Neutrino Technology) collaboration which is operating a low-threshold germanium detector underground searching for dark matter. One important benefit of this symbiosis is our experimental work, simulation, and analysis of slow-rising pulses that originate in the dead layer on the surface of PPC detectors. We are developing a novel preamplifier featuring ultra-low noise. This will allow for a lower threshold leading to an improved low-energy analysis and the possibility to veto harmful decays for the  $0\nu\beta\beta$  measurement as well.
- We take an active part in analysis and software tasks within the collaboration by contributing to the overall Monte Carlo code development and its validation.

### 1.2.1 Preamplifier with forward biased reset for CoGeNT and MAJORANA

A. Knecht, J. Leon, D. A. Peterson, R. G. H. Robertson, and T. D. Van Wechel

Development work continues on a charge-sensitive preamplifier continuously reset by the forward biased gate-to-source junction of the input JFET. The DC stabilization of a conventional charge-sensitive amplifier is provided by a high-value feedback resistor in parallel with the feedback capacitor. This resistor provides a DC path for the net input bias and detector currents at the amplifier input so that the feedback capacitor does not eventually charge to the output saturation voltage. It would be advantageous to eliminate the feedback resistor as it is a major noise source.

It is possible to operate a JFET with zero volts on the control gate, or even a small forward bias. A JFET has an operating point where the current of the forward biased gate cancels the reverse leakage current. The detector leakage of a positively biased detector can also be canceled by the forward biased gate current. If the DC operating point of the JFET could be stabilized so that the forward biased gate current is equal to the sum of the gate leakage current and the detector leakage current, the feedback resistor and its noise contribution

---

<sup>1</sup>CENPA Annual Report, University of Washington (2011) p. 18.

could be eliminated. Only the feedback capacitor would then be required to provide charge feedback.

We are using a tetrode JFET that has superior noise performance and provides a means of DC stabilization without a DC connection to the control gate. A tetrode JFET has two gates, a control gate that has low input capacitance for improved noise performance and a second gate, the substrate gate, that can be used to set the drain-source current  $I_{DS}$ . There are two feedback loops. A low-pass feedback loop is connected to the substrate gate, to stabilize the DC operating point so that the average net charge at the input is zero. The second feedback loop, a feedback capacitor between the preamplifier output and the control gate, provides charge feedback in the preamplifier passband.

Noise tests of several Moxtek JFETs have been performed in the past year. We have developed LabView programs that use data from a digital oscilloscope to measure the noise spectral density of the preamplifier output and also the equivalent noise charge (ENC) versus peaking time. So far the MX-30 JFET has had the best noise performance. Tests with an MX-30 JFET with an open input have shown noise levels of less than 6 electrons RMS. We plan further tests with MX-35 and MX-40 JFETS since they would require a lower substrate voltage for the desired operating point based on power dissipation.

Noise tests have also been made with capacitors of various dielectrics on the order of 1 to 2 pf to match the expected detector capacitance at the input. Surprisingly, a fused silica dielectric capacitor showed about the same dissipation noise as a silver mica capacitor. The test capacitor has a NiCr layer under the top Au layer. The reason for the NiCr base layer is to provide an adhesion layer for the Au and to form the resistors of the preamplifier circuit. The Au is deposited onto the NiCr where the conductive circuit traces are desired. Further tests of fused silica dielectric capacitors with different materials for the adhesion layer are planned to determine if the NiCr layer causes excessive dissipation noise. Tests will also be made with an air dielectric capacitor at the input as a comparison.

Tests with a low-capacitance Si photodiode at the input have recently commenced. This is to provide a more realistic, unidirectional charge input signal (from LED light pulses), than charge injection through a test input capacitor provides. This will allow rate-dependence studies. So far the initial photodiode tests have shown excessive current noise.

In the near future we plan to construct a prototype on a fused silica substrate with bare die semiconductors and NiCr deposited resistors. We plan to take it to Berkeley Labs to test with an actual BeGe detector, so it needs to be dimensioned to fit the Berkeley test fixture. A new post-amplifier will need to be developed and constructed to match the Berkeley setup.

### 1.2.2 Cross-talk studies with parylene cables

A. Knecht, J.D. Mulligan, and T. D. Van Wechel

We are performing a study of the electrical crosstalk between channels of a parylene-coated cable for the MAJORANA DEMONSTRATOR experiment. Parylene is a vapor-deposited polymer with very low radioactivity necessary for low radioactive backgrounds in the MAJORANA DEMONSTRATOR experiment. As neutrinoless double beta decay ( $0\nu\beta\beta$ ) is hypothesized to be an extremely rare process, a thorough understanding of the electrical crosstalk is necessary to adequately interpret the measured signals. Moreover, we seek to measure the magnitude of crosstalk in order to determine if parylene cables, along with accompanying shielding and connectors, are viable for the MAJORANA DEMONSTRATOR experiment.

The study consists of three cable configurations: unshielded parylene cable, copper-shielded parylene cable, and copper-shielded parylene cable with connectors. In each case, the parylene cable consists of 10 channels. We have taken data for the first two configurations.

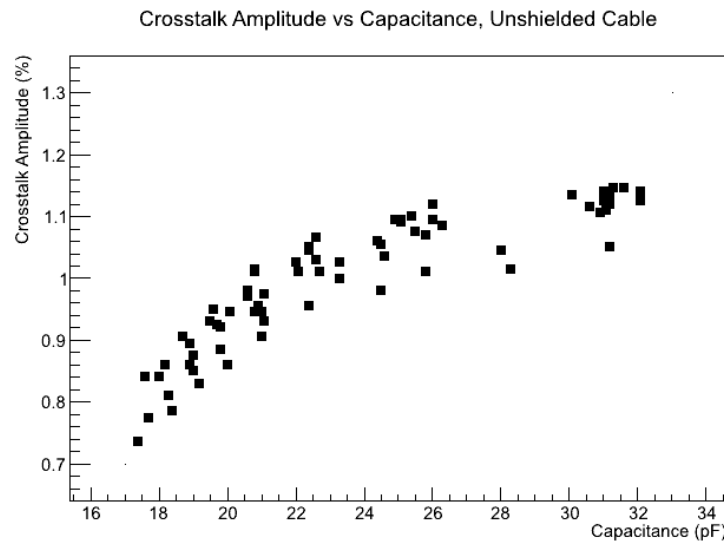


Figure 1.2.2-1. Crosstalk amplitude (as a percent of input pulse amplitude) vs. capacitance for pairs of wires in the unshielded 10-channel parylene cable.

Our principal method is to provide an input voltage pulse of a given rise time on one channel and measure the resultant crosstalk amplitude on each of the other channels. We also measure the capacitance between each pair of channels and the crosstalk amplitude as a function of the rise time of the input pulse, as well as the crosstalk output for a sinusoidal input. For unshielded parylene cable and parylene cable shielded with copper tape, we have performed these measurement for all combinations of inputs and outputs. A plot of the crosstalk amplitude as a function of capacitance for the unshielded cable is given in Fig. 1.2.2-1. We are further investigating these results using simulations.

In addition to interpreting our current data, we will insert connectors into the shielded parylene cable and repeat our previous procedures in order to measure the additional crosstalk introduced by the connectors.

### 1.2.3 MAJORANA single-string test cryostat

M. D. Busch\*, M. P. Green\*, G. C. Harper, and M. L. Miller<sup>†</sup>

String test cryostats have been designed to test, characterize, and store assembled Ge detector strings until ready to install in the MAJORANA DEMONSTRATOR cryostats<sup>1</sup>. Parts for two such units (Fig. 1.2.3-1) were fabricated at UW and shipped to UNC for assembly and testing.

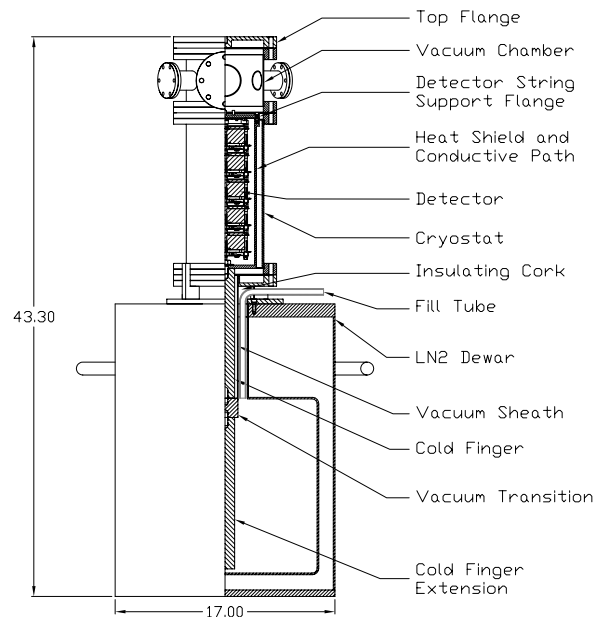


Figure 1.2.3-1. Cross-sectional sketch of the MAJORANA single-string test cryostat.

The string-test cryostat is based on a standard commercial detector dipstick cryostat but is large enough to accommodate a full single string and uses all metal seals to prevent diffusion of radon into the vacuum space. A high-conduction thermal path is provided via a 4 cm diameter copper cold finger structure and a thick-walled copper heat shield. The copper parts for the test cryostat are currently being cleaned and passivated at UNC. They will be tested there before being shipped to the SURF in Lead, South Dakota. The Ge crystals are expected to cool to a temperature below 90 K in the test cryostats.

\*University of North Carolina, Chapel Hill, NC.

<sup>†</sup>Presently at Cloudant, Inc., Seattle, WA.

<sup>1</sup>Final Design Report, The MAJORANA DEMONSTRATOR, The MAJORANA Collaboration, February, 2012.

#### 1.2.4 Preparation and shipping of Pb bricks for the MAJORANA shield

N. M. Boyd, A. Knecht, J. Leon, M. L. Miller\*, R. G. H. Robertson, and D. I. Will

We have extracted 3500 lead bricks from a sub-basement laboratory of the University of Washington's Atmospheric Sciences-Geophysics building (ATG). The bricks were carefully packaged, hoisted up to the ground, and shipped in 2.5 truck loads to Black Hills State University, SD, for further cleaning. They will form the innermost layer of the MAJORANA lead shield surrounding the detectors.



Figure 1.2.4-1. A. Knecht and J. Leon hoisting one full pallet of lead from the sub-basement.

---

\*Presently at Clodant, Inc., Seattle, WA.

Lead that is free of radioactive contaminants fulfills the need to shield our detectors from  $\gamma$  rays without introducing further backgrounds. This means the lead must be old enough to allow for embedded  $^{210}\text{Pb}$  to decay to acceptable levels. We previously reported on a promising collection of lead bricks found in ATG and the lead-etching procedure used to clean their surfaces of radioactive contaminants and mercury<sup>1</sup>. Assay results of these bricks show that they do in fact have suitably low levels of U/Th/K radiation, while also confirming the absence of  $^{210}\text{Pb}$ .

The recovery of the lead bricks consisted of packing specially made heavy-duty pallets with 80 bricks each and transporting these from their underground location in ATG. Special care was taken to ensure safe working conditions. Concerns regarding exposure to lead and mercury vapor while packing were met by using protective gear and actively monitoring the air at all times. The personal protective gear consisted of Tyvek suits, shoe booties, latex gloves, leather gloves, and dust masks. In the summer of 2010 a test run was completed where we removed three full pallets and showed that we were below the legal 8-hour exposure limit for both mercury and lead. This was followed by a full-scale project to extract all 48 tons of lead beginning in early 2011. Results of air monitoring during the full recovery confirmed that working conditions met the legal requirements.

Packing and hoisting of the lead bricks was completed in approximately 20 days by a small group of CENPA personnel consisting of staff members, a postdoc, and a graduate student. The bricks were packed in two layers of 40 bricks each and double-wrapped in Visqueen which provided shielding from the environment during transit. Prior to final shipment, all 46 pallets were tested for residual mercury contamination and were found to have none. The entire load was shipped to Black Hills State University before the end of March, 2012.

### 1.2.5 Searches for dark matter with a MAJORANA prototype

J. I. Collar\*, A. Knecht, J. Leon, M. G. Marino<sup>†</sup>, M. L. Miller<sup>‡</sup>, J. L. Orrell<sup>§</sup>, and J. F. Wilkerson<sup>¶</sup>

Following the challenges laid out in last year's report<sup>2</sup>, we have examined 442 days of data from a low-threshold germanium detector for indications of an annual rate modulation. The P-type point contact (PPC) germanium detector operated in a low-background setting underground at Soudan Underground Laboratory in Soudan, MN. Along with superb resolution, this PPC has demonstrated a low threshold of  $0.5 \text{ keV}_{ee}$ , which makes it sensitive to light-WIMP dark matter models. We report on the presence of a modulated component compatible with a light-mass WIMP scenario<sup>3</sup>.

---

\*University of Chicago, Chicago, IL.

<sup>†</sup>Technische Universität München, Excellence Cluster Universe, Munich, Germany.

<sup>‡</sup>Presently at Cloudant, Inc., Seattle, WA.

<sup>§</sup>Pacific Northwest National Laboratory, Richland, WA.

<sup>¶</sup>University of North Carolina, Chapel Hill, NC.

<sup>1</sup>CENPA Annual Report, University of Washington (2010) p. 21.

<sup>2</sup>CENPA Annual Report, University of Washington (2011) p. 19.

<sup>3</sup>C.E. Aalseth *et al.*, Phys. Rev. Lett. **107**, 141301 (2011).

The 442 days of livetime data presented here were collected from December 4, 2009 until March 6, 2011. X-ray peaks from electron capture (EC) decays are expected to contribute in the low energy region. After subtracting both this predicted contribution and a flat spectral component, an exponential-like background is still present (Fig. 1.2.5-1). Hypothetical signals from a light-WIMP are also displayed for reference. One distinct feature of a putative WIMP-nuclei interaction signal is that its event rate is predicted to exhibit an annual modulation. Our device maintained exceptional low-energy stability which made it possible to look for such a modulation. Fig. 1.2.5-1 shows the rate versus time in the energy region where the statistical significance for this modulation is maximal. The statistical significance of the modulation is  $2.8\sigma$ , limited by short exposure and low fiducial mass. No indication of a modulation was observed for energies beyond this region.

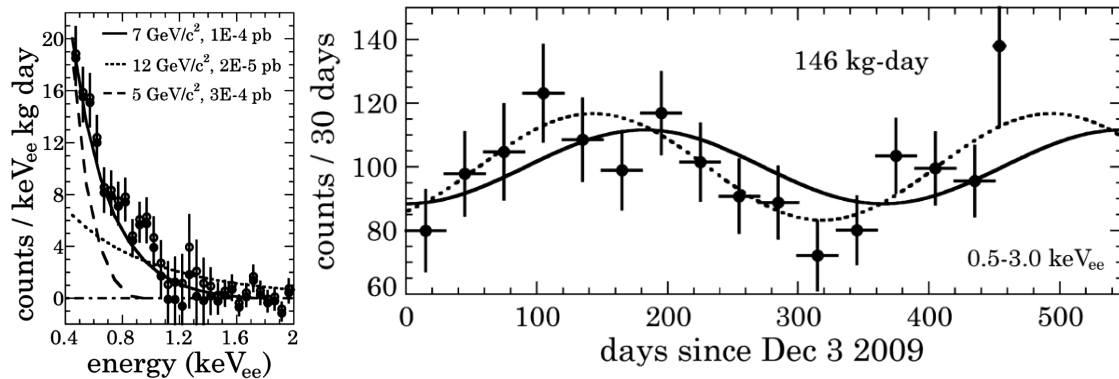


Figure 1.2.5-1. Left: Spectra stripped of  $L$ -shell EC contribution and flat background component. Examples of light-WIMP signals are overlapped. Right: Rate vs. time for the energy region  $0.5\text{--}3.0\text{ keV}_{ee}$ . Dotted line denotes the best-fit modulation and the solid line represents a prediction for a  $7\text{ GeV}/c^2$  WIMP with standard galactic halo parameters.

### 1.2.6 A Monte-Carlo model of the background energy spectrum of the MALBEK detector

P. Finnerty\*, G. K. Giovanetti\*, R. Henning\*, M. L. Miller<sup>†</sup>, R. G. H. Robertson, A. G. Schubert, and J. F. Wilkerson\*

A good understanding of the MAJORANA DEMONSTRATOR background energy spectrum will be required to interpret results of a  $0\nu\beta\beta$  search and to project background rates for a tonne-scale germanium experiment. A modified Canberra Broad-Energy Germanium (BEGe) detector is deployed in a low-background shielded environment at the Kimballton Underground Research Facility (KURF) near Ripplemead, VA. We simulated the energy-spectrum response of this detector, the MAJORANA Low-background BEGe at KURF (MALBEK), to expected backgrounds and compared the results to an energy spectrum collected at KURF in 2010.

\*University of North Carolina, Chapel Hill, NC.

<sup>†</sup>Presently at Cloudant, Inc., Seattle, WA.

This work validates our understanding of backgrounds and our ability to model the energy spectrum of the detector response.

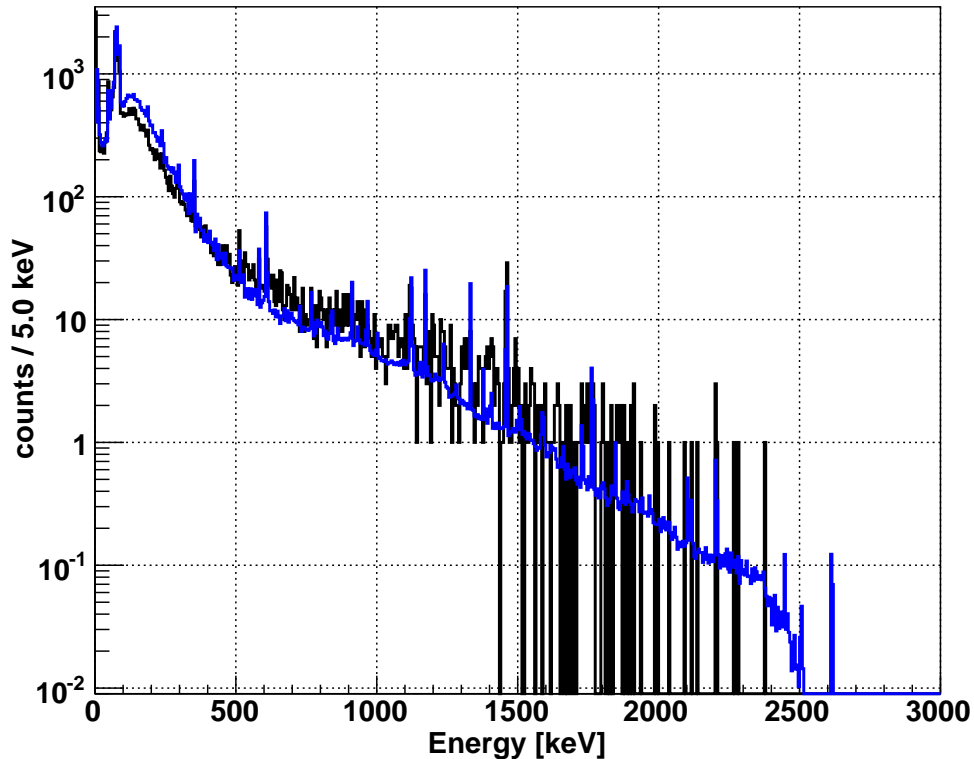


Figure 1.2.6-1. A 55-day background energy spectrum, collected with MALBEK at KURF in 2010 (black), is compared to a MAGE model of the energy spectrum (blue).

The geometry of the MALBEK detector and shielding is described in MAGE, a Monte Carlo software toolkit developed by the MAJORANA and GERDA collaborations and based on the physics simulation package GEANT4. We used MAGE to simulate the MALBEK response to decays of radioactive isotopes expected from cosmogenic activation and primordial contamination of the cryostat and shield. Most simulations were performed on the CENPA-Rocks cluster. The spectrum resulting from each simulation was normalized to the number of counts expected in the KURF data according to the number of simulated decays, MALBEK's history of cosmogenic exposure, live-time, and material radiopurity data. The spectra were added to create a model of the MALBEK background energy spectrum. Many features of the spectrum collected at KURF are well reproduced by the MAGE-based model, shown in Fig. 1.2.6-1.

## SNO+

### 1.3 Overview of the SNO+ experiment and CENPA's contribution

J. Kaspar, T. J. Major, N. R. Tolich, and H. S. Wan Chan Tseung

SNO+ is a large-volume underground liquid scintillator neutrino experiment presently under development at the SNOLAB facility, in Sudbury, Ontario, Canada. It is a multi-purpose detector whose reach extends to the following areas of neutrino physics: neutrinoless double beta decay ( $0\nu\beta\beta$ , with Nd-loaded scintillator), geo-neutrinos, and reactor and low-energy solar neutrinos. In addition, a large liquid scintillator detector serves as an excellent supernova neutrino monitor.

SNO+ will use a lot of the infrastructure left behind by the completed Sudbury Neutrino Observatory (SNO) experiment, including the acrylic vessel (AV), photomultiplier tubes (PMTs) and most of the electronics. The main engineering work concerns the AV, which will have to be anchored to the floor after scintillator filling. A hold-down system has been designed, and the ropes are now being manufactured. Data-taking is scheduled to start in mid-2013.

In SNO+ the data rate is expected to be two orders of magnitude higher than in SNO, and therefore updates to the SNO electronics and data acquisition (DAQ) system are needed. CENPA is responsible for updating the DAQ into a faster, ORCA-based system compatible with the electronics upgrades that are being planned by the University of Pennsylvania. These include new XL3 cards for controlling the 19 data crates. Software for operating the XL3s through ORCA has been written and tested at the typical rates expected from SNO+. The full DAQ system was commissioned this year (see Sec. 1.3.1). CENPA is also responsible for the SNO+ slow-control system which records and monitors a large number of detector-related variables at a rate of  $\sim 1$  Hz. This system was installed and commissioned this year (see Sec. 1.3.2).

The proposed scintillator is linear alkyl benzene (LAB) with  $\sim 3$  g/L of 2,5-diphenyloxazole (PPO). To achieve the goals of the experiment, it is imperative to understand the optical properties of this scintillator. At CENPA, we developed an experiment to study scattering in LAB-PPO (see Sec. 1.3.3).

#### 1.3.1 Commissioning of the SNO+ data acquisition software

M. A. Howe\*, J. Kaspar, N. R. Tolich, and J. F. Wilkerson\*

The SNO+ DAQ software is based on ORCA, a general-purpose, highly modular, object-oriented, acquisition and control system. The DAQ pulls data from the VME trigger crate, and nineteen data crates operating in an independent asynchronous way push data into the DAQ system. On the ORCA side, XL3s, the data crate controllers, are served by circular

---

\*University of North Carolina, Chapel Hill, NC.

buffers running in parallel in independent threads. A data manager pulls data from the buffers and serializes them into the data stream. The SNO+ design data rate is 450 Mbit/sec.

This year, control of HV power supplies and HV relays was added into DAQ. The HV feedback loop monitors voltages, charge rates, and PMT base currents. The HV management is complicated by multiple HV power supplies controlling PMTs in a single data crate while a single HV power-supply may control PMTs in multiple crates. The analog part of the trigger system was integrated into DAQ to tweak trigger pulses coming from individual data crates. The implementation relies on LabJacks hooked to the single board computer mastering the trigger system. Work on integration of the LED and laser calibration system into DAQ was started, and prototype boards were successfully tested. The final pieces of hardware to be merged are power control of data crates, an emergency stop box, and an uninterruptible power supply (UPS).

A polling loop to monitor hardware status is to be the next addition to DAQ this year. Information on raw PMT charge rates (numbers of charge pulses crossing a preset channel threshold), FIFO hardware buffers to collect PMT data from 32 channels, XL3 memory buffers, PMT base currents, and front-end voltages is passed to monitoring tools through a CouchDB server. Our work on monitoring tools will continue this year to highlight the most relevant pieces of information to ease detector operations. Dedicated user dialogs that are focused on common detector operations (ramping HV and time and charge calibrations) are part of this effort.

We contributed an ORCA-to-ROOT decoder for the event builder and finalized the file format for data storage. Work on a threaded ROOT-tree writer capable of writing tree branches into a data file in parallel faster than 1 Gb/sec was finished. The detector setup parameters come from multiple CouchDBs (ORCA, electronics calibration, defects, and test-stand DBs). This year we will work on a flexible way to mix parameters from these DBs.

The final ORCA DAQ commissioning took place during the first air-fill run in March, 2012. Most crates were ramped to HV for two weeks for the first time after four years of electronics upgrades and DAQ development. We took a couple of TBs of data and trained new operators. The data are being analyzed to further optimize electronics and software. The new XL3 controllers and DAQ were both proven stable and reliable. Two more air-fill runs are scheduled in the summer followed by a water-fill run to start at the end of the year. A detector operator manual will be written.

### 1.3.2 SNO+ detector and slow-control monitoring tools

J. Kaspar, N. R. Tolich and H. S. Wan Chan Tseung

In this section, we report on the high-level detector user interface and monitoring tools in ORCA, as well as a web browser-based monitor for slow controls.

The SNO+ detector monitor in ORCA is designed to be independent of the low-level hardware controls so as not to affect the performance of the DAQ code. Every two seconds

ORCA pushes XL3 card parameters such as CMOS rates, PMT base currents, and front-end card voltages to a CouchDB server. These are then read back periodically in ORCA and displayed graphically according to a color scale. Fig. 1.3.2-1 (bottom window) shows a view of the CMOS rates, with actual data taken during air-fill runs in March, 2012.

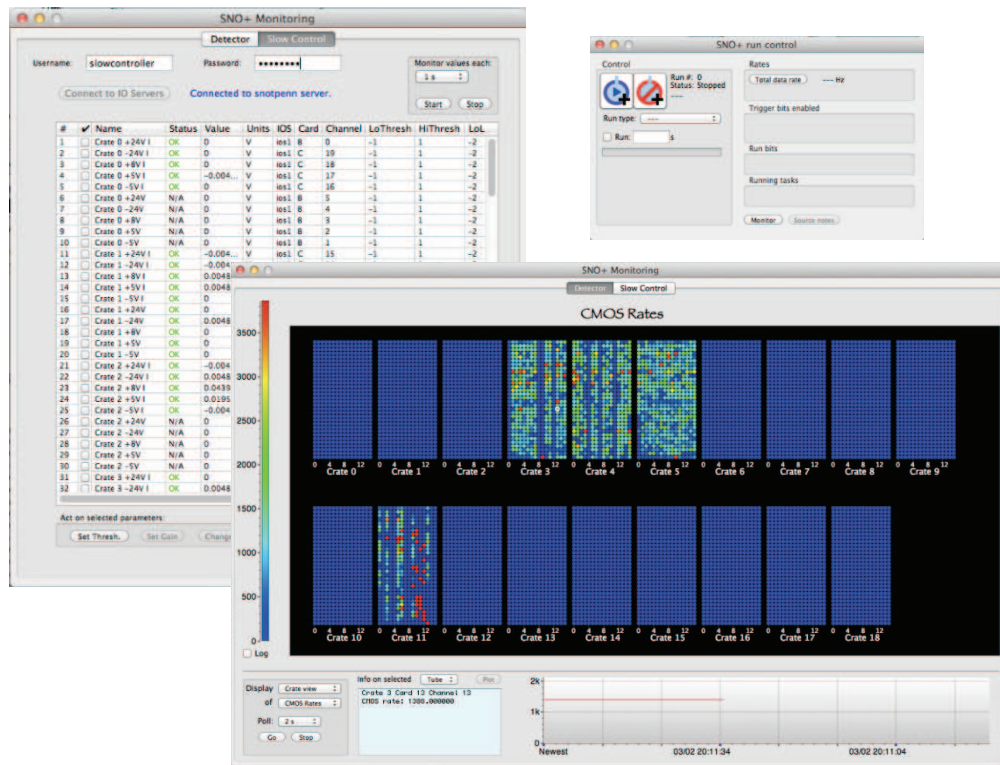


Figure 1.3.2-1. Left window: ORCA slow-control monitor. Top right window: SNO+ run-control interface. Bottom window: SNO+ detector monitor in ORCA, showing air-fill data from March, 2012.

The slow control monitor in ORCA (Fig. 1.3.2-1, left window) displays the I/O server hardware map and the latest value, status, and thresholds of each variable. Parameter thresholds can be altered using this interface.

The purpose of the web-based slow-control monitor is to provide graphical display of slow-control parameters over an extended period of time. It pulls data at a specified frequency from the I/O servers and stores them in a CouchDB server. The size of this database is estimated to be around 8 Gb for one week of data. The slow-control variables from each I/O channel are then displayed graphically with a JavaScript CouchApp. A set of maintenance scripts refreshes the CouchDB views and compresses the database on a periodic basis.

### 1.3.3 Scattering of visible light in liquid scintillator

T. J. Major and N. R. Tolich

The SNO+ experiment will utilize approximately one kiloton of linear alkyl benzene (LAB) inside an acrylic sphere surrounded by light water. Because LAB is a liquid scintillator, hundreds of photons are emitted approximately isotropically when an event such as a  $\gamma$  ray or  $\beta$  decay occurs inside its volume. Since SNO+ will measure the timing, position, and number of detected photons, it is critical to understand the scattering properties of LAB. In particular, the extent to which photons generated in the LAB will undergo Rayleigh scattering (RS) versus scattering by absorption and reemission (AR) is unknown.

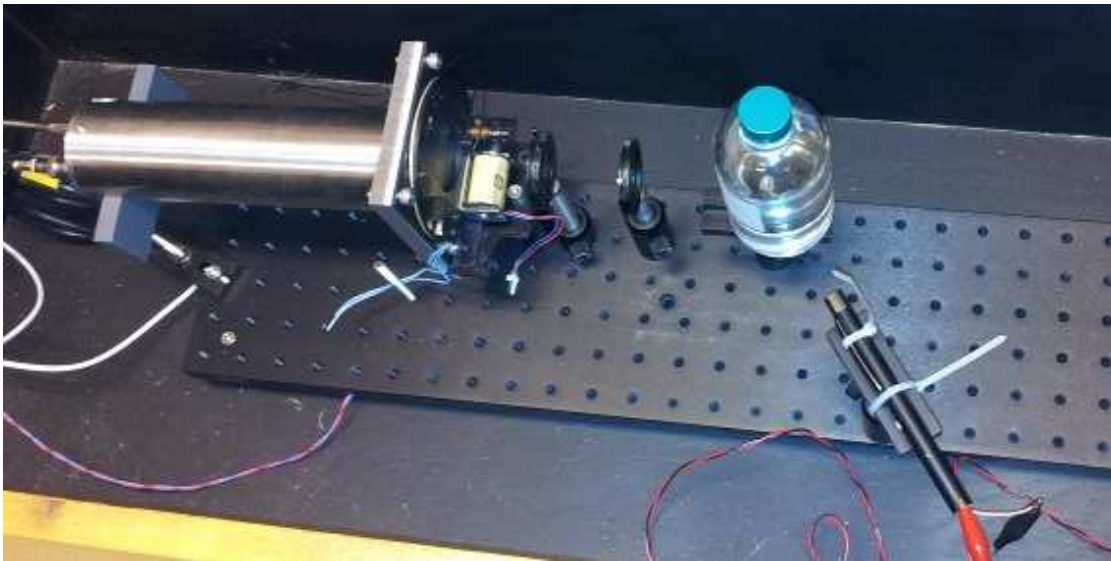


Figure 1.3.3-1. Apparatus for measuring light scattered from LAB. On the left is a PMT enclosed in a canister with a shutter. On the upper right is a jar of LAB and on the lower right is the movable laser.

In order to measure the relative prevalence of these scattering processes, we have constructed an apparatus (see Fig. 1.3.3-1) which uses a photomultiplier tube and a movable diode laser to measure the intensity of light scattered by LAB as a function of angle. By using polarizing filters and lasers of different wavelengths we expect to be able to compare the measured distribution of scattered light with expected RS and AR distributions. Refinements to the apparatus are still being constructed.

## Project 8

### 1.4 Status of the Project 8 neutrino mass measurement prototype

L. I. Bodine, R. F. Bradley\*, P. J. Doe, J. A. Formaggio<sup>†</sup>, D. L. Furse<sup>†</sup>, R. A. Johnson<sup>‡</sup>, J. Kaspar, J. N. Kofron, M. L. Leber<sup>§</sup>, L. L. McBride, M. L. Miller<sup>¶</sup>, B. Monreal<sup>§</sup>, M. F. Morales, R. G. H. Robertson, L. J. Rosenberg, G. Rybka, W. A. Terrano, T. Thuemmler<sup>||</sup>, and B. A. VanDevender\*\*

Existing experimental constraints on neutrino mass come from oscillation experiments ( $m_\nu \geq 0.02$  eV) and the Mainz experiment ( $m_\nu < 2.2$  eV). The KATRIN experiment is designed to probe the neutrino mass with a sensitivity of about 0.2 eV with a MAC-E spectrometer similar to that used at Mainz. The Project 8 collaboration is exploring the possibility of performing a neutrino mass measurement based on a low-temperature radiometry technique which promises sensitivity to the  $0.02 \text{ eV} \leq m_\nu \leq 0.2 \text{ eV}$  region.

The technique hinges upon the passive detection of cyclotron radiation emitted from a trapped electron with energy near the endpoint energy of the  $\beta$  decay spectrum<sup>1</sup>. Construction and testing of a prototype experiment has been underway for approximately one year in order to characterize the response and possible systematic uncertainties associated with such a technique.

In order to anticipate the possibility of scaling a small ‘table-top’ electron spectrometer to a full neutrino-mass-measurement facility, the prototype takes the form of a magnetic bottle made of a section of WR42 waveguide. The power emitted by the electron into the waveguide in such an experiment obeys the relationship  $P \propto \int_X \vec{j} \cdot \vec{e}_{TE01}$ , which is identical to the coupling term expected in a large-scale cavity experiment. The waveguide is then suspended in a strong background magnetic field of  $\approx 1$  T and a carrier-free gas of  $^{83m}\text{Kr}$  is injected via gas lines. The waveguide is coupled in either direction to waveguide inputs of low noise-temperature amplifiers on loan from the National Radio Astronomy Observatory. The amplifiers are maintained at a temperature of  $\approx 30$  K.

In order to facilitate in-situ measurements of the total magnetic field at the trap position, a sample of 2,2-diphenyl-1-picrylhydrazyl (DPPH) is located on the trap axis a short distance away. The existence of an electron paramagnetic resonance signal from the DPPH then allows the magnetic field at the sample to be measured. In order to scan the magnetic field at many source positions, a dynamic piston seal is being designed and manufactured by CENPA

---

<sup>1</sup>B. Monreal and J. Formaggio, Phys. Rev. D **80**, 051301, (2009).

\*National Radio Astronomy Observatory, Charlottesville, VA.

<sup>†</sup>Massachusetts Institute of Technology, Cambridge, MA.

<sup>‡</sup>University of Colorado, Boulder, CO.

<sup>§</sup>University of California, Santa Barbara, Santa Barbara, CA.

<sup>¶</sup>Presently at Cloudant, Inc., Seattle, WA.

<sup>||</sup>Karlsruhe Institute of Technology, Karlsruhe, Germany.

\*\*Pacific Northwest National Laboratory, Richland, WA.

engineers to allow the experiment to be translated in the z direction (vertically) during the course of a run.

The signal-to-noise ratio for this experiment is currently estimated at 10. Engineering efforts are presently underway, with data-taking anticipated in late Spring, 2012.

## HALO

### 1.5 The HALO supernova detector

T. H. Burritt, C. A. Duba<sup>\*</sup>, F. Duncan<sup>†‡</sup>, J. Farine<sup>‡</sup>, A. Habig<sup>§</sup>, A. Hime<sup>¶</sup>,  
M. A. Howe<sup>††</sup>, C. Kraus<sup>‡</sup>, D. A. Peterson, R. G. H. Robertson, K. Scholberg<sup>||</sup>,  
M. Schumaker<sup>‡</sup>, J. Secrest<sup>\*\*</sup>, T. D. Van Wechel, C. J. Virtue<sup>‡</sup>, J. F. Wilkerson<sup>††</sup>,  
S. Yen<sup>‡‡</sup>, and K. Zuber<sup>§§</sup>

HALO (Helium and Lead Observatory) is nearing ‘first light’ at SNOLAB. It will be a detector of supernova neutrinos with sensitivity covering most of the galaxy, but nevertheless compact, low in cost, and low in maintenance. These features are obtained through the use of Pb as a neutrino target. Neutrino interactions on Pb, both charged-current and neutral-current, populate neutron-unstable states in product nuclei, and the neutrons emitted can be moderated and detected in <sup>3</sup>He-filled proportional counters. The counters are the ones used in the final stage of the SNO experiment to detect neutrons produced by the neutral-current interaction of solar neutrinos on deuterium. The 79 tonnes of Pb are also reused, originally a part of a cosmic-ray neutron monitor array sited at Deep River. Steady progress has continued over the past year (Fig. 1.5-1 left).

All of the remaining intercounter welds joining individual counters (‘NCDs’) have been cut apart using a special cutter made at UW, and the counters have been installed in the lead matrix. New stainless-steel endcaps and connectors made on our CNC lathe have been successfully installed and cabled to preamps. Seventy of the original current-mode preamps have been modified for charge-mode readout to reduce sensitivity to impulse noise and improve resolution. These have been shipped to Sudbury and successfully tested.

Tests on the best shaping time to use in the VME-based shaper-ADCs have been carried out, with an interesting and somewhat unexpected result (see Fig. 1.5-1 right).

---

<sup>\*</sup>Digipen Institute of Technology, Redmond, WA.

<sup>†</sup>SNOLAB, Sudbury, ON, Canada.

<sup>‡</sup>Laurentian University, Sudbury, ON, Canada.

<sup>§</sup>University of Minnesota Duluth, Duluth, MN.

<sup>¶</sup>Los Alamos National Laboratory, Los Alamos, NM.

<sup>††</sup>University of North Carolina, Chapel Hill, NC.

<sup>||</sup>Duke University, Durham, NC.

<sup>\*\*</sup>Armstrong Atlantic State University, Savannah, GA.

<sup>‡‡</sup>TRIUMF, Vancouver, BC, Canada.

<sup>§§</sup>TU Dresden, Dresden, Germany.

Drift time in the  $^3\text{He}\text{-CF}_4$  gas can be up to  $3\ \mu\text{s}$ , and long shaping times give, as expected, the best energy resolution on the 764-keV full-energy neutron-capture line. Shorter shaping times around  $1\ \mu\text{s}$ , however, do a better job of separating the low-energy  $\gamma$  background tail from the 190-keV ‘proton edge’ that marks the lower end of the neutron-capture spectrum. At the proton edge the neutron-capture event consists of a short triton track sticking out of the wall into the gas, the proton having been absorbed in the wall. In contrast,  $\gamma$  events generally must traverse the entire counter diameter to deposit enough energy to compete with the triton. The  $\gamma$  events therefore can be effectively discriminated against with a short shaping time. The loss of energy resolution at the full energy peak is of little consequence, since (for efficiency), the entire range from 200 to 764 keV will be taken as a candidate neutron signal.

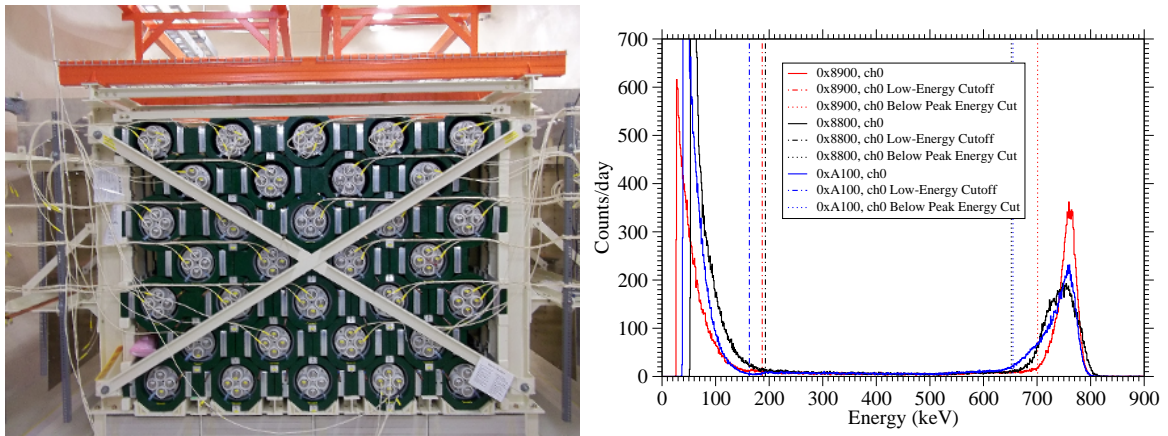


Figure 1.5-1. Left: Face of the HALO detector as of December, 2011, showing 4 NCDs in each cavity in the lead matrix. Right: Spectra from neutron counters with three different shaper-ADC versions. The black curve is from an unmodified SNO shaper-ADC, which is still configured for current mode and lacks a differentiator. The red and blue curves are charge-mode cards with  $4\text{-}\mu\text{s}$  and  $1\text{-}\mu\text{s}$  shaping times, respectively. Data and plots by Michael Schumaker.

Hardware for a pulser distribution system has been recovered from the SNO NCD electronics and work has started on a continuous calibration and monitoring task that will run within the ORCA data-acquisition program. An initial survey of the lead array has been completed and 16 of the lead rings have been instrumented with linear potentiometers to record any creep in the lead array. The calibration tubes for moving sources to various locations inside HALO have been installed and tested. One foot of water shielding has been placed around the HALO detector leaving only the front face unshielded at present. Some calibration data will be recorded in this shielding configuration and shortly the full neutron shielding will be completed. It is anticipated that all channels will be operational by summer, 2012, and that HALO will join the Supernova Early Warning System later in the year.

## 2 Fundamental symmetries and non-accelerator-based weak interactions

### Torsion-balance experiments

#### 2.1 Overview of the CENPA torsion-balance experiments

E. G. Adelberger

A surprisingly large number of ideas for solving open problems in fundamental physics, many of which are directed at unifying gravity with the rest of physics, predict new ultra-weak forces mediated by conjectured low-mass particles. String-theory ideas are particularly prolific in this regard, as the conjectured extra dimensions and the large number of low-mass particles all produce new forces. The discovery of such forces would have a revolutionary impact, and sufficiently sensitive upper bounds on the forces severely constrain the theories.

Motivated by these considerations, the CENPA Eöt-Wash group develops advanced torsion-balance techniques for sensitive mechanical measurements and applies them to address problems of current interest. We have produced the most sensitive tests of the equivalence principle<sup>1</sup>, tested the Newtonian inverse-square law to the shortest distances<sup>2</sup>, and tested certain Lorentz-violating properties of electrons five orders of magnitude below the Planck scale and non-commutative geometry at the  $10^{13}$ -GeV level<sup>3</sup>. We currently operate 7 different torsion-balance instruments. Each one is devoted to a particular topic and is often the thesis project of an individual graduate student. At this moment one of the instruments is used for tests of the equivalence principle, two are used to probe short-range gravity, two are used to search for new electron-spin-dependent forces, and two are dedicated to investigating the subtle factors that limit the sensitivities of delicate mechanical experiments. The gravity group's expertise with mechanical systems and small forces has led to involvement in the gravitational-wave detectors LIGO and LISA. For advanced LIGO we are developing a beam balance to measure ground tilt. The contributions below outline our progress in this area during the past year.

This work is primarily supported by NSF grant PHY-0969199 and the salaries, etc. of faculty, students and postdocs are covered by the NSF. Costs of some equipment used in both NSF- and DOE-sponsored research are shared between the two funding sources.

---

<sup>1</sup>S. Schlamminger *et al.*, Phys. Rev. Lett. **100**, 041101 (2008).

<sup>2</sup>D. J. Kapner *et al.*, Phys. Rev. Lett. **98**, 021101 (2007).

<sup>3</sup>B. R. Heckel *et al.*, Phys. Rev. D **78**, 092006 (2008).

### 2.1.1 Rotating torsion-balance test of the equivalence principle update

E. G. Adelberger, J. H. Gundlach, B. R. Heckel, S. Schlamminger\*, H. E. Swanson, and T. A. Wagner

This year an improved source model for the earth was developed allowing exclusion limits on Yukawa potentials with ranges from 20 km to 1000 km for the first time. We also improved the data acquisition and control loops for the torsion balance and expanded the number of sensors available. We expect to complete our upgrades during the summer of 2012.

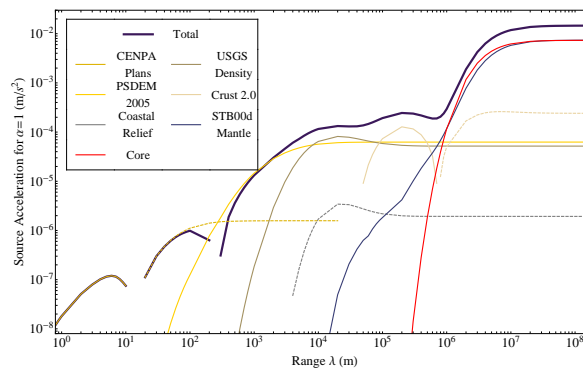


Figure 2.1.1-1. The contributions to the overall north component of the source integral for  $\tilde{q} = B$  by model. Solid and dotted lines indicate the acceleration of a  $+B$  “charge” toward north and south, respectively.

The source model must accurately describe the direction of forces due to a hypothetical new Yukawa force. For interaction ranges longer than  $\sim 1$  km, the subsurface density contributes substantially. The rock density primarily determines this with the specific composition playing a role around the  $\sim 10\%$  level. The range between a few km and 1000 km depends heavily on the local subsurface geology which is difficult to model. Fortunately, the complex geology of Puget Sound has been the subject of intensive research for seismic activity which resulted in the production of high-quality density models of the regional crust. The new source model includes updated high-resolution topography<sup>1</sup>, regional crustal density<sup>2</sup>, and whole-earth geological models<sup>3,4,5</sup>. The model contributions are illustrated in Fig. 2.1.1-1.

The new data-acquisition system will expand the number of analog to digital channels from 16 to 32. The torsion pendulum signal shows repeatable structure due to turntable irregularities. The previous control loop addressed the first nine harmonics of the rotation

\*National Institute of Standards and Technology, Gaithersburg, MD.

<sup>1</sup> D. Finlayson, “Combined bathymetry and topography of the Puget lowlands, Washington state,” <http://www.ocean.washington.edu/data/pugetsound/> (2005).

<sup>2</sup> W. J. Stephenson, “Velocity and density models incorporating the Cascadia subduction zone for 3d earthquake ground motion simulations, version 1.3,” Open-File Report 2007-1348, U.S. Geological Survey, Earthquake Hazards Ground Motion Investigations (2007).

<sup>3</sup> G. Laske, A. Dziewonski, and G. Masters, “Reference Earth model,” <http://igppweb.ucsd.edu/~gabi/rem.html> (2011).

<sup>4</sup> A. M. Dziewonski and D. L. Anderson, *Phys. Earth. Planet. Inter.* **25**, 297–356 (1981).

<sup>5</sup> B. Steinberger, *Phys. Earth Planet. Inter.* **118**, 241–257 (2000).

frequency and some high-frequency components due to the angle encoder. While the systematic effect at the turntable rotation frequency has been shown to be stable over time, the higher-frequency components introduce additional noise into the system. A prototype control loop that runs on a fast computer is being developed to investigate control strategies while a field-programmable gate array (FPGA) device has been selected to run the updated control loop with guaranteed timing and real-time loop updates. The existing tilt stabilization control loop was closely integrated with the data acquisition and output. The new hardware supports faster sampling rates which will reduce the need to adjust the base sampling frequency and the resulting transient events as the control loops are adjusted.

### 2.1.2 First data from a hydrogen-rich equivalence-principle pendulum

E. G. Adelberger, B. R. Heckel, and W. A. Terrano

We have begun taking data with the prototype hydrogen-rich pendulum designed to probe non-gravitational interactions with dark matter<sup>1</sup>. The larger size of this pendulum, due to the low density of polyethylene (PE) and the need to offset the large passive mass of the aluminum shielding, required altering the optical path of the autocollimator. We added a second mirror so that the total optical path length remained constant. We vacuum baked the pendulum at 65° C for 10 days to reduce outgassing from the polyethylene to a rate which the ion-pump could handle.

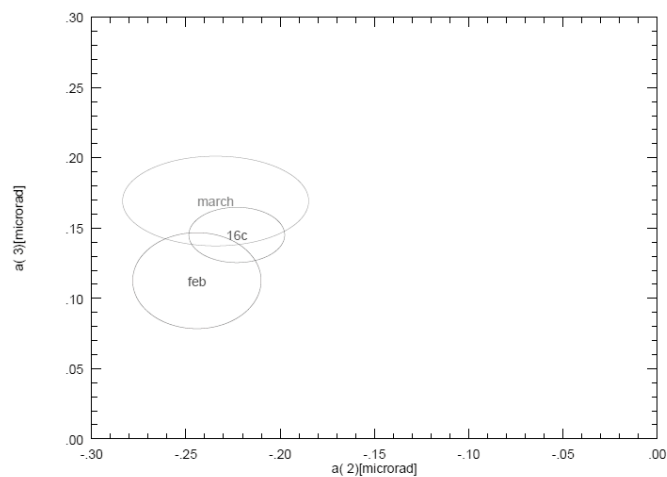


Figure 2.1.2-1. Plot of the 2 components of the q21 signal. Circles marked “march” and “feb” were data taken about a month apart for which there is no resolved change. The temperature was 20.5° C for both. The other circle corresponds to data taken at 16.5° C.

<sup>1</sup>CENPA Annual Report, University of Washington (2009) p. 31.

The gravitational moments of the pendulum appear to be stable. By rotating a turntable with a large Q21 moment (used to cancel the ambient gradients), we can measure the q21-Q21 gravitational coupling of the pendulum. The q21 moment of the pendulum changed significantly following the baking, indicating that the heating had caused some components to move. Measuring the q21 moment of the pendulum at 20.5° C and 16.5° C allows us to constrain thermal systematics related to the large coefficient of thermal expansion of polyethylene. We observe a change in the q21 of  $16 \pm 23$  nanoradians (nrad) with a 4 K temperature change. The diurnal temperature variation is of order 10  $\mu$ K, so this effect should be minimal. We also measured the q21 moment in February and again in March to verify that there is no significant mechanical creep in the system (see Fig. 2.1.2-1).

The data is much noisier than with previous pendula, especially on weekdays. Weekends show reasonable performance of 6 nrad in a day compared with 2 nrad in a day with the last pendulum used in this apparatus. This suggests that the ongoing construction in the area may have significantly increased the seismic activity at the lab. We have begun making a dummy pendulum of the same size, mass, and moment of inertia, but without polyethylene and more rigidly assembled, to investigate the sources of the additional noise.

### 2.1.3 Development of a second-generation hydrogen-rich equivalence-principle pendulum

E. G. Adelberger, B. R. Heckel, J. Lee, and W. A. Terrano

We are developing a second-generation hydrogen-rich equivalence-principle pendulum using what we have learned from our prototype (see Sec. 2.1.2). The major improvements involve reducing the mass and gravitational moments of the pendulum and designing test bodies which are removable and more rigidly secured to the frame.

To have a reasonable active/passive mass ratio while enclosing the polyethylene (PE) in metal, the prototype pendulum is large and massive<sup>1</sup>. Reducing the mass from 127 grams to 70 grams allows us to go from a 30  $\mu$ m-diameter tungsten fiber to a 20- $\mu$ m thick fiber. This drops the torsion constant by a factor of  $\approx 5$  and the thermal noise of the fiber by about a factor of two. The thinnest available encasing shield, regardless of structural concerns, is 0.020" thick extruded aluminum. This alone would weigh about 30 grams.

The complex internal structure<sup>1</sup> makes it sensitive to high-order gravitational gradients. These are irrelevant when looking at long-range interactions with dark matter or the Sun which are modulated daily, but make it very difficult to use lab-fixed sources such as the Earth. Since the Earth's field is 2-6 times larger than that of the Sun (depending on the charge of the new interaction), reducing the higher-order moments will allow us to improve existing constraints on  $Z$ - or  $N$ -coupled interactions

A major step was gold-coating a piece of PE, accomplished by sputtering chromium on as an adhering layer. The thin gold layer from sputtering may not be sufficient to shield

---

<sup>1</sup>CENPA Annual Report, University of Washington (2009) p. 31.

electromagnetic effects, however. Our experience with the prototype pendulum suggests that out-gassing from the PE will pose a difficult systematic effect without an azimuthally symmetric screen. We are attempting to electroplate the PE and seal it from out-gassing with a vacuum-leak sealant. Our current design is shown in Fig. 2.1.3-1.

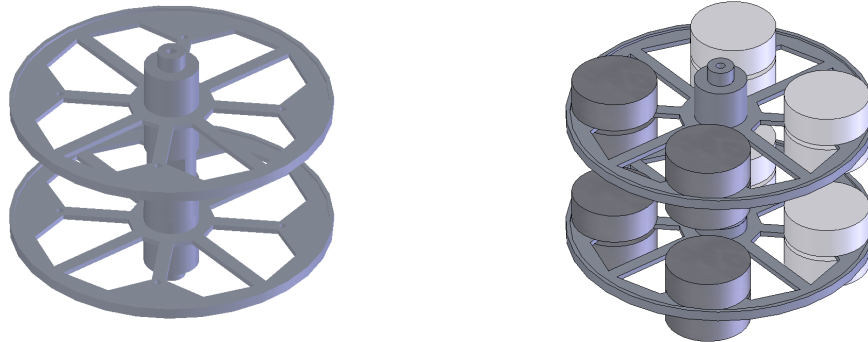


Figure 2.1.3-1. Schematics of a new pendulum design. On the left is the aluminum frame with cutouts to reduce mass. 1/8" holes are used to mount test bodies from their combined center of expansion, as illustrated on the right.

#### 2.1.4 Wedge-pendulum test of short-range gravity

E. G. Adelberger, T. S. Cook, and H. E. Swanson

This past year we have taken the third complete set of data with the wedge pendulum. A number of insights and improvements of both apparatus and modeling accompanied this set. It will likely be the last with the pendulum and attractor in their current configuration.

Before collecting data, much effort was spent accurately aligning and measuring the attractor. The laser attachment on our OGP ZipLite measuring microscope was invaluable as a tool to verify alignment with sub-micron precision. New techniques were pioneered for inspecting the attractor with the scope, adjusting the attractor mount to be centered and perpendicular to the axis of rotation, aligning the stretched copper screen above the attractor disk, and detecting whether the attractor makes contact with the screen. These efforts allowed us to confidently set the attractor-to-screen distance approximately  $5 \mu\text{m}$  closer than previously achieved, to a separation of  $14 \mu\text{m}$ .

An overhaul of our gravitational and capacitance modeling was also completed. We determined that a simple, flat model of the tungsten wedges and glue was inadequate to describe our geometries. Detailed inspections of the pendulum and attractor show a cone shape to the pieces, as well as the existence of a parasitic 18-fold mass distribution on the outside rim of the pieces<sup>1</sup>. New models now use multiple smaller wedges of varying sizes and offset heights to better account for the geometry (see Fig. 2.1.4-1).

<sup>1</sup>CENPA Annual Report, University of Washington (2011) p. 36.

Lastly, new tungsten foils have been manufactured for the next iteration of the experiment which will employ pieces 100- $\mu\text{m}$  thick instead of 50- $\mu\text{m}$  thick. We hope to achieve better overall flatness with these foils and we are modifying our mounting technique to eliminate the problem of the outside rim.

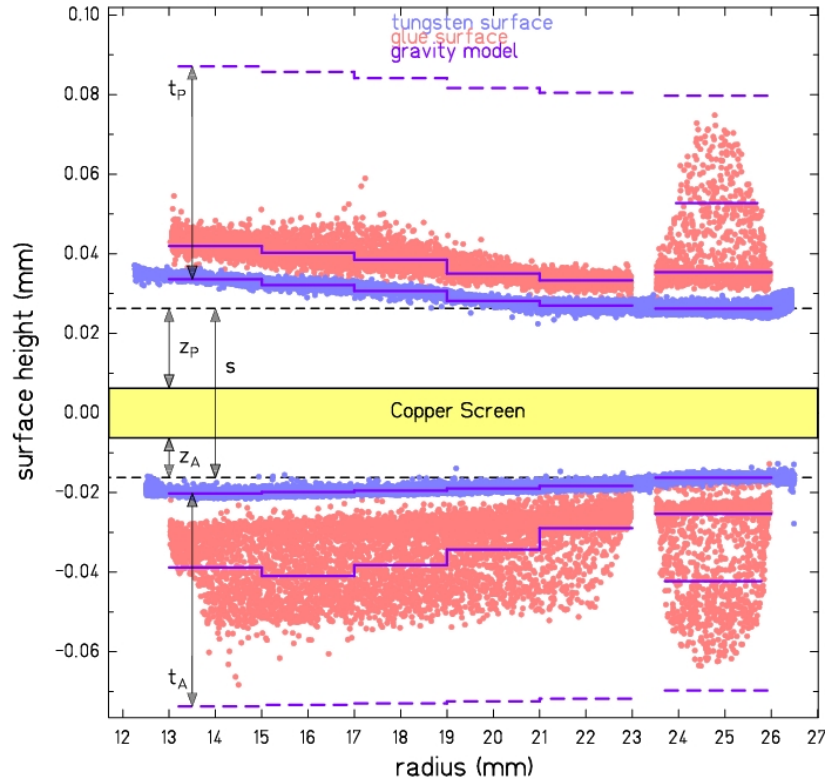


Figure 2.1.4-1. Data from laser scans now form a more detailed gravitational model of the pendulum and attractor. The same data are also used in new capacitance models for determining  $z_P$  and  $z_A$ .

### 2.1.5 Parallel-plate inverse-square-law test update

J. H. Gundlach, C. A. Hagedorn, and M. D. Turner

A parallel-plate geometry is the most efficient signal-to-mass arrangement for a test of the gravitational inverse-square law. Parallel plates are first-order insensitive to systematic effects from Newtonian gravity. Work on our parallel-plate inverse-square-law test at sub-millimeter scales continues.

The 660-nm fiber-coupled laser reported last year<sup>1</sup>, while it gave improved intensity and stability to the foil fiber interferometer, suffered from mode-hops. Attempts at stabilization

<sup>1</sup>CENPA Annual Report, University of Washington (2011) p. 34.

met with insufficient success, yielding mode-hops every few seconds. We opened the experiment and switched to 1330-nm optical fiber. With a distributed-feedback fiber-coupled laser and exclusively FC/APC fiber connections, the new beamsplitter and detector systems were selected to prevent mode-hopping. The interferometer now modehops less than once a week, as seen in Fig. 2.1.5-1. The present high-frequency noise limit may be polarization noise from changing stress in the optical fibers.

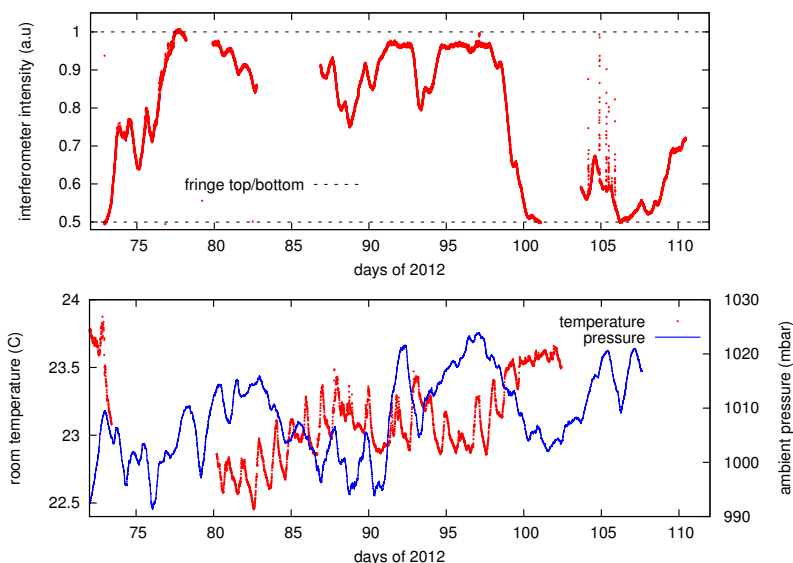


Figure 2.1.5-1. Interferometer stability (unregulated). Note lack of mode-hops (discontinuities). One fringe corresponds to 330 nm of foil displacement. Scatter near Day 105 caused by deliberate attractor/foil collisions. Temperature and air-pressure changes are the usual causes of drift. Drift may correlate with low-passed ambient temperature.

An on-line foil/attractor alignment system was designed, built, and installed. It permits full alignment of the experiment after bell-jar evacuation. This flexibility has improved the closest approach of the 75-mm-diameter attractor to the foil from 39  $\mu\text{m}$  to 15  $\mu\text{m}$ .

The pneumatic valves controlling the attractor bellows were replaced with automotive fuel injectors. These valves provide faster switching, lower leak rates, and better isolation than the ASCO valves they replaced. The new isolation valve allows shutdown of the pressure control system during each measurement (every 128 s). Closing a third (manual) isolation valve at the bell jar wall allows complete tests for electrical systematics without attractor motion.

Analysis improvements were made, with an independent re-write of data preprocessing using finite impulse response (FIR) filters instead of calibration fitting and drift subtraction. Bootstrapped uncertainty estimation is standard when making inferences from processed data.

We performed a pair of science runs. The first resolved a signal related to the impedances of current-limiting resistors connecting the attractor and foil to contact potential batteries. The second run is ongoing.

### 2.1.6 Development of dedicated gravity gradiometer systems

J. H. Gundlach, C. A. Hagedorn, S. Z. D. Plachta, and M. D. Turner

One of the leading systematic uncertainties in our group's current equivalence-principle test is due to the variation of the local gravitational gradient over time. Although we measure the gradient periodically by replacing the science pendulum with a dedicated gradiometer pendulum, continuous monitoring of the gradient would allow for either correction to the readout data or active compensation using actuated near-field masses. We have been developing a low-drift, low-cost gravity gradiometer to monitor the gradient over long periods.

In order to mitigate the effect of instrument and sensor drift, it is necessary to modulate the signal. Because the gradiometer is measuring the field due to natural surroundings, it is necessary to modulate some property of the torsion balance which has been done in our past and current experiments by continuously rotating the torsion balance. For this application we have instead been pursuing an active-mass torsion pendulum design where the gravitational moments of the pendulum itself can be modulated. Challenges involved in creating such a pendulum include using an actuator with a minimal amount of magnetic and ferromagnetic materials, supplying power and control signals to this actuator, and accurately monitoring and setting the position of the masses. We have investigated various solutions and are currently assembling a second-generation prototype.

In order to produce these gradiometer systems at low cost we have also developed a miniature autocollimator for readout of the angular deflection of the pendulum. This autocollimator's sensitivity and dynamic range are comparable with our standard autocollimators but it has a reduced component count and price. Analog-to-digital conversion of the readout signal is done on-board by a microcontroller and the same component is capable of providing a feedback signal or other analog output. This readout-and-control system is expected to be used for other modular torsion balance systems.

### 2.1.7 Progress on the development of a cryogenic torsion balance

E. G. Adelberger, F. Fleischer, B. R. Heckel and H. E. Swanson

We have continued to explore the noise performance and the mechanical losses of the cryogenic torsion balance which has been described in earlier annual reports<sup>1,2</sup>.

The magnetic shield, made from CO-NETIC AA<sup>3</sup>, has been mounted and its shielding factor for small external magnetic fields has been determined to be  $\sim 80$ . The addition of this shield has led to an observation of somewhat improved quality factors  $Q$  of the torsion balance at low temperature. Values of up to about 5000 could be obtained, still significantly lower than expected. While this confirms our previous assessment that the losses were dominated by eddy current damping, it is also a clear indication of the existence of another problem.

---

<sup>1</sup>CENPA Annual Report, University of Washington (2009) p. 28.

<sup>2</sup>CENPA Annual Report, University of Washington (2010) p. 40.

<sup>3</sup><http://www.magnetic-shield.com/products/conetic.html>

Dedicated test runs with a pendulum instrumented with a silicon diode temperature sensor connected via  $\sim 2$  m of low-thermal-conductivity phosphor bronze leads revealed that the cooling of the pendulum by thermal radiation and via the torsion fiber proceeds more slowly than originally estimated. This is in accordance with more detailed simulations of the cooling process. To solve this problem, a pressure-actuated clamp (operated with helium gas) was designed and built to act as a thermal switch. It was shown to enable rapid cooling of the pendulum to equilibrium temperature. Furthermore, we could show that room-temperature thermal radiation from the autocollimator viewport prevents us from operating the torsion balance anywhere near the target temperature of 5 K. We are working on mitigating this problem by adding cold infrared filters anchored to the thermal shields.

Regarding the noise, we have found that the autocollimator currently in use with this experiment does not perform as well as other, nearly identical ones used by our group. It seems that this is due to mode-hopping caused by light backreflected into the laser diode. If we achieve the high values of  $Q$  we are hoping for, an additional decrease in the autocollimator noise beyond the levels realized in our better-working autocollimators will be needed. We are currently investigating possible concepts for a new, more sensitive autocollimator.

In summary, we expect to be able to operate the torsion balance at its design temperature very soon and we expect to see substantial improvements in terms of  $Q$  value and thermal noise. We are planning to try other fiber materials besides tungsten, in particular beryllium copper and Al 5056. The latter two have been reported to yield very high values of  $Q$  at LHe temperature<sup>1</sup>. The next step should be an improvement in autocollimator noise level to be able to make full use of the improved thermal noise.

### 2.1.8 Progress on magnetic shielding for a search for short-range spin-coupled forces

E. G. Adelberger, B. R. Heckel, and W. A. Terrano

The torsion-balance experiment to measure spin-dependent forces<sup>2</sup> is nearly ready for commissioning.

Our pendulum has a large number of aligned spins in order to be sensitive to spin-coupled forces. This makes demonstrating that the magnetic couplings can be controlled an essential component to the experiment. We have improved our setup for measuring the residual magnetic fields<sup>3</sup>. It now includes an encoder allowing us to combine measurements from many rotations of the pendulum and a 3-axis translation stage for the probe so that we can scan the magnetic field at different heights and radii. Since our science signal has a 10-fold symmetry under rotation of the pendulum we are interested in the magnetic fields of the same symmetry, the  $10\text{-}\omega$  component. All magnetic-field amplitudes quoted are the  $10\text{-}\omega$  components of the field<sup>2</sup>.

---

<sup>1</sup>M. K. Bantel and R. D. Newman, *J. of Alloys and Compounds*, **310**, 233 (2000).

<sup>2</sup>CENPA Annual Report, University of Washington (2007) p. 38.

<sup>3</sup>CENPA Annual Report, University of Washington (2011) p. 32.

We retuned the magnetic field of the Alnico segments this time tuning each segment at three different radii. To do this we made a new yoke that would expose only an individual Alnico segment to a large magnetic field. Using shunts we could set the external magnetic field precisely and then insert the ring as far as needed to tweak the magnetization at a specific radius. The rings of magnets are then encased within high- $\mu$  cans made from annealed Conetic AA. The fields outside were small enough that we had to shield the stainless-steel bearing on the encoder and move it from the turntable to the motor shaft.

The leakage field outside of the shielded pendulum ring was  $\approx 150 \mu\text{G}$ , while the residual field of the shields alone was typically around  $15 \mu\text{G}$ , and as low as  $5 \mu\text{G}$  when degaussed. This suggests that our shielding can be improved. Degaussing the shielded pendulum ring at 1 Hz reduced the fields to  $90 \mu\text{G}$ . Adding a second set of shields brought us down to  $15 \mu\text{G}$ , the level of the Conetic itself. Absent other ways of reducing the residual magnetic field, we will probably need to run with two sets of shields on the pendulum.

The phase of the magnetic field depends only on the orientation of the outer shield. Combining two runs with the outer shield rotated by  $18^\circ$  with respect to the ring cancels most of the  $10\text{-}\omega$  signal:  $2 \pm 2 \mu\text{G}$ . The phase of the spin signal depends only on the orientation of the magnetic rings. This provides a method to separate magnetic and spin signals even below the intrinsic magnetization of the mumetal, although designing a system to rotate the outer shield in-situ is challenging.

The most important number is magnetic feedthrough from a singly-shielded attractor ring rotating underneath a static magnetic shield. We measure the component of the field at 10 times the rotation rate to be  $1.4 \pm 1 \mu\text{G}$ , although it rises to several  $\mu\text{G}$  toward the edge of the shield. Taking this into consideration, we have redesigned the foil mount to better enclose the source and separate it from the pendulum.

### 2.1.9 A precision tiltmeter for advanced LIGO

T. B. Arp, J. H. Gundlach, C. A. Hagedorn, M. D. Turner, and K. Venkateswara

We are developing a high precision-tiltmeter to improve seismic isolation in advanced LIGO (aLIGO) which is a next-generation gravitational-wave detector system. Gravitational waves are a prediction of Einstein's theory of general relativity. Direct detection of gravitational waves has been pursued over the last forty years culminating in the new generation of detectors which are expected to make first detections when turned on in 2015. aLIGO uses a Michelson-interferometer-based configuration with a laser, a beamsplitter, 4-km-long arms, and suspended mirrors at the ends. The dark port of the interferometer is sensitive to differential length changes between the arms which are caused by a passing gravitational wave. Initial LIGO had a sensitivity to differential length changes on the order of  $10^{-18}$  m.

A series of improvements and upgrades is expected to yield sensitivities better by nearly an order of magnitude in the 100-Hz to 1-kHz band while expanding the lower end of the bandwidth from 40 Hz to 10 Hz. Key among these improvements is a better seismic isolation system to cancel the effect of ground motion on the mirrors. This is done through an

active control system which measures the ground motion through seismometers and applies a corrective force on the optics platform. At low frequencies (10 mHz to 0.5 Hz), however, seismometers are strongly affected by ground rotation/tilt which can interfere with the ability to correct the motion. Thus, aLIGO needs a ground-rotation sensor or tiltmeter to accurately distinguish between horizontal motion and tilt. The requirements on the sensitivity of the tiltmeter are more than an order of magnitude more stringent than commercial tiltmeter sensitivities.

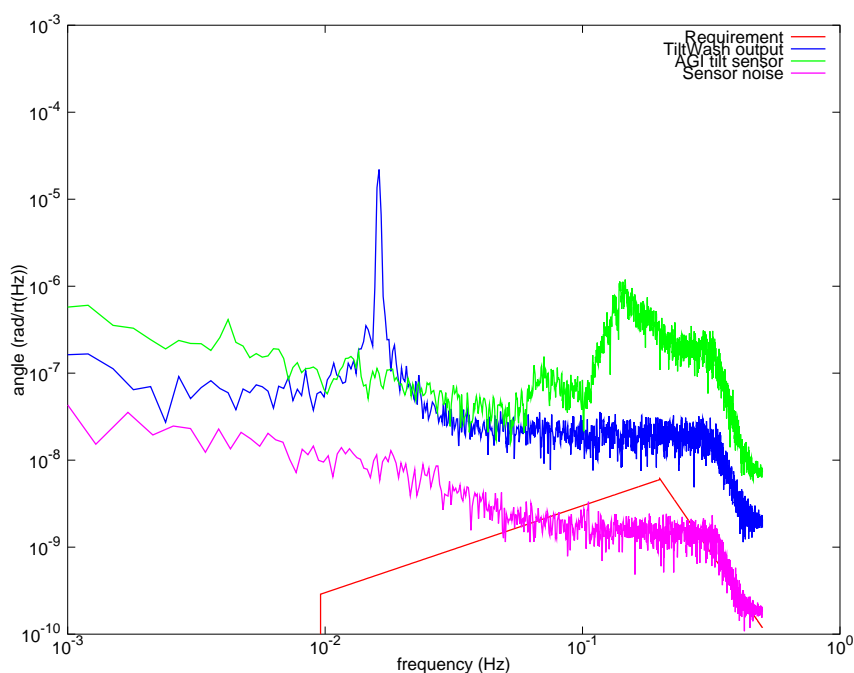


Figure 2.1.9-1. Plot showing the sensitivity of our tiltmeter compared to a commercial AGI tilt sensor.

Our tiltmeter consists of a very-low-frequency flexure beam balance and we measure its angle using an autocollimator mounted to the floor/platform. Above its resonance frequency the balance remains inertial and the autocollimator measures ground tilt. Horizontal ground motion is rejected by locating the center of mass at the pivot point of the flexure. The prototype beam consists of a 1.6-m aluminum tube with 1.3-kg brass weights attached at each end. It is suspended by two copper beryllium flexure hinges  $\sim 50 \mu\text{m}$  thick.

Fig. 2.1.9-1 is an amplitude-spectral-density plot of the autocollimator output compared with a commercial AGI tiltmeter. Our current sensitivity is  $\sim 10^{-8} \text{ rad}/\sqrt{\text{Hz}}$ . We are currently investigating various noise sources and are also developing a new autocollimator which promises better sensitivity.

### 2.1.10 Large-dynamic-range autocollimator

T. B. Arp, J. H. Gundlach, C. A. Hagedorn, S. Schlamminger\*, M. D. Turner, K. Venkateswara, and J. Walrath<sup>†</sup>

Non-contact measurement of rotation is essential to any torsion balance. We have developed an improved autocollimator design with dynamic range greater than  $10^7$ . The design permits  $\text{mrad}/\sqrt{\text{Hz}}$  sensitivity over  $1^\circ$  rotation. An optical-breadboard prototype was a successful proof of principle but could not be directly mounted on a balance. Furthermore, the prototype was not fully optimized for low-frequency performance.

We designed and constructed a practical version of the prototype. The apparatus was built with low-frequency stability in mind. The body, lens tubes, and flanges were constructed with thick aluminum walls for strength and thermal stability. The light source is fiber-coupled and readout electronics are external to the detector to remove heat sources from the instrument. Critical optical parts were made to  $\mu\text{m}$  tolerances from fused silica.

The primary machining was done in the UW physics shop by Larry Stark. His suggested use of taper pins for alignment made assembly easily repeatable.

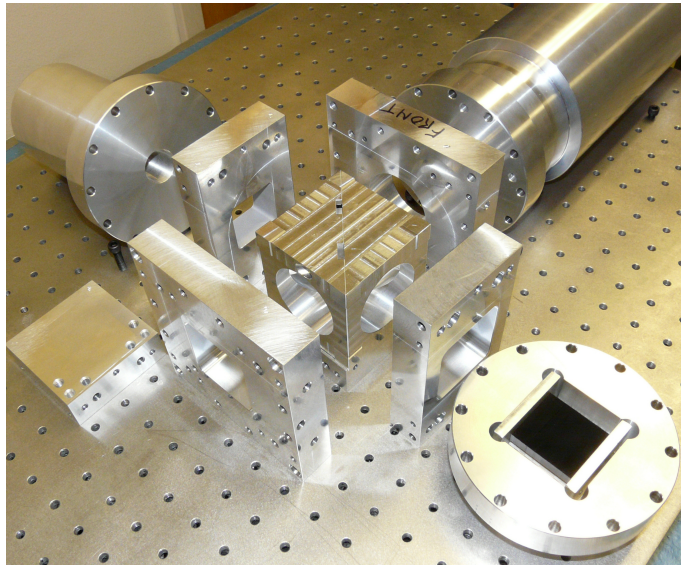


Figure 2.1.10-1. Autocollimator before optics assembly. Clockwise around beamsplitter cube from top left: Illumination optics, objective tube, razor beamstop, and readout mount.

Commissioning of the device is underway. After optimizing the autocollimator's performance we intend to mount the autocollimator on our new inertial rotation sensor (see Sec. 2.1.9). A LIGO-related specification of  $5 \times 10^{-10} \text{ rad}/\sqrt{\text{Hz}}$  at 10 mHz is our ultimate goal. Initial results suggest that the new design surpasses the prototype in both sensitivity and stability.

\*National Institute of Standards and Technology, Gaithersburg, MD.

<sup>†</sup>University of Michigan, Ann Arbor, MI.

### 2.1.11 Wireless environmental sensor network

T. B. Arp, J. H. Gundlach, C. A. Hagedorn, S. Z. D. Plachta, M. D. Turner, and A. Zhdanova

Precision experiments are sensitive to environmental change. The Eöt-Wash experimental hall houses seven operating experiments. Two of these search for signals that vary with daily and annual periods, the others operate in the mHz range. Each experiment runs a set of environmental sensors but none run without downtime. We built an independent array of sensors that operates continuously to provide long-term measurements of the hall environment.

Measurements of temperature and temperature gradients were first. Eight wireless sensors, using XBee radios, were distributed throughout the room, outside the entrance, in the HVAC duct, and on the roof. Each radio was installed on a custom circuit board that provided battery power, a temperature sensor, and a signal amplifier. The sensors were collectively calibrated to better than 100 mK in a temperature-controlled container. Later we added humidity, door, and sunlight sensors.

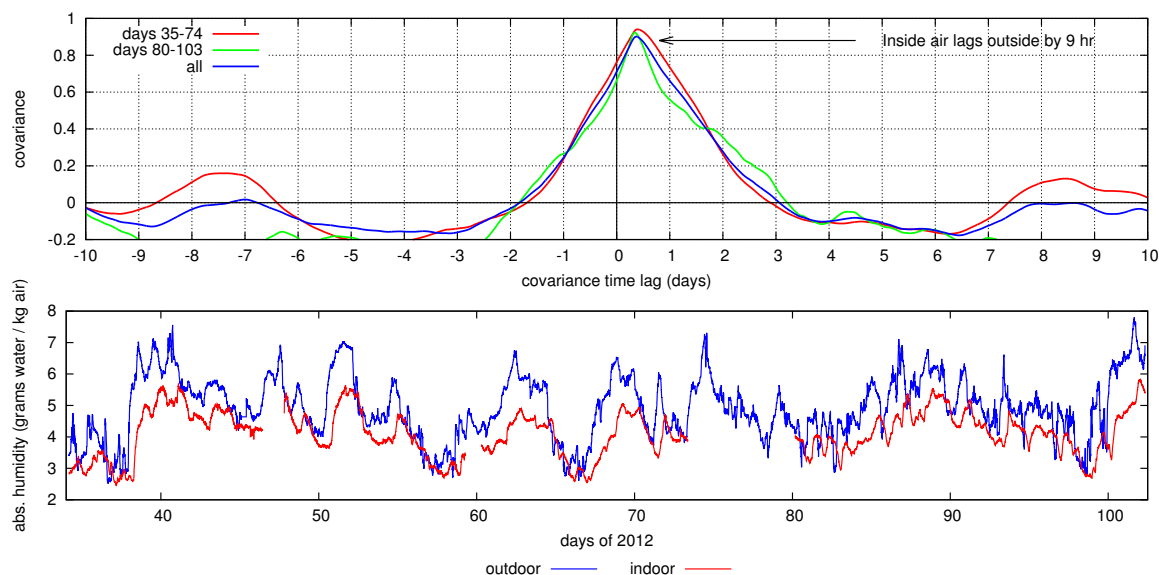


Figure 2.1.11-1. Absolute humidity inside and out, with covariance, to assess room air exchange.

The wireless network is extendable and allows seamless addition and removal of instruments of all types with variable sample rates. Graphs are updated daily and shown on a central display (Fig. 2.1.11-1). Integration of the room sensors into better temperature control is nearly complete.

Torsion balances are sensitive to the external environment. The equivalence-principle experiments are sensitive to the rain-driven water table. Noise, especially in the short-range gravity experiments, correlates with wind and seismic activity. We installed a full weather station on the CENPA roof and are adding integrating seismometers to the sensor network.

## Non-accelerator-based weak interactions

### 2.2 Overview of the CENPA non-accelerator-based weak interactions experiments

A. García

This year the UCNA collaboration continued to take data towards a precise determination of the  $\beta$  asymmetry (see Sec. 2.2.1). At Seattle we developed a system to map the thickness of the foils containing calibration sources (see Sec. 2.2.2).

The mercury-EDM group has made progress on several improvements to their system which will allow for a more sensitive search for Time-Reversal Symmetry violation (see Sec. 2.2.3).

During the last year the emiT collaboration, searching for Time-Reversal Symmetry breaking in the decay of neutrons, worked on finishing a long paper with details on the experiment (see Sec. 2.2.4). The collaboration is now satisfied and the submission of the long paper will likely occur soon.

#### 2.2.1 Status of the UCNA experiment

A. García, R. Hong, A. Knecht, and C. Wrede\* for the UCNA collaboration

The goal of the UCNA collaboration is a precise measurement of the  $\beta$  asymmetry in neutron decay. The experiment utilizes ultra-cold neutrons produced at the Los Alamos Neutron Science Center (LANSCE). Ultra-cold neutrons are polarized by passage through a 7-T superconducting magnet and fed into a decay trap within a 1-T superconducting solenoidal magnet. Two electron detectors at the ends of the solenoidal magnet measure the  $\beta$ -decay asymmetry directly. From the measured decay asymmetry one can extract the ratio of axial to vector coupling constants  $g_A/g_V$ . With the neutron lifetime as an additional input it is then possible to calculate  $V_{ud}$ , the up-down element of the weak quark mixing matrix. All these values are basic elements of the Standard Model. In addition, comparing these results to measurements of nuclear  $\beta$ -decay serves as a stringent test of our current understanding.

Over the last year the experiment was steadily taking data. We have reached a total of about 40 million decays which will allow an extraction of the  $\beta$  asymmetry at the 0.6% level. The collaboration is aiming at moving forward and taking the necessary data to reach a 0.4% measurement. The group at the University of Washington contributed by taking shifts at LANSCE and by preparing a system to measure the precise thicknesses of the different electron calibration foils employed in the experiment (see Sec. 2.2.2). By knowing those thicknesses their effect on the calibration electrons can be calculated.

---

\*Michigan State University, East Lansing, MI.

## 2.2.2 UCNA calibration-source foil-thickness measurement

A. García, R. Hong, A. Knecht, and T. G. MacDonald for the UCNA collaboration

Energy calibration plays an important role in the UCNA experiment. The foil thicknesses of the calibration sources affect the spectrum of the conversion electrons. Therefore, it is important to measure the thickness over the active part of the foil.

At CENPA we developed a device to map the foil thicknesses via the energy loss of  $\alpha$  particles from a  $1\text{-}\mu\text{Ci } ^{241}\text{Am}$  source. The energy of the  $\alpha$ s is stable and does not overlap with the energy of the conversion electrons. We collimated the  $\alpha$ s using a 0.0135-inch-diameter collimator in order to guarantee a good spatial resolution. The  $\alpha$  particles were detected by a silicon detector.

We mounted a 2-D horizontal motion-control system inside the target evaporation chamber allowing us to control the motions of the two perpendicular rails from outside the chamber. The  $x$ -direction rail was connected to a rotation-linear motion converter, which moves 0.030 inches per turn. The wheel of the motion converter outside the chamber is driven by a stepping motor which can be controlled remotely by the data-acquisition system. The  $y$ -direction rail is loaded by a spring and a 10/24 screw pushes against it. This screw is connected to a rotational feedthrough by a flexible joint but it can only be controlled by hand. Therefore the scan of one foil can be done without opening the chamber. The entire system, with the source and collimator, is shown in Fig. 2.2.2-1.

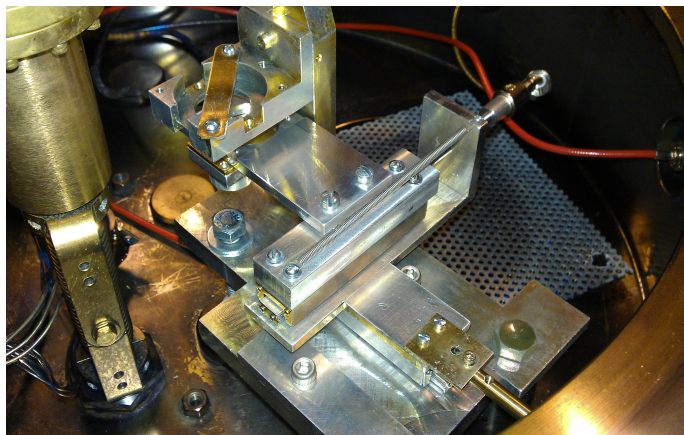


Figure 2.2.2-1. Motion-control system with source and collimator mounted.

We had a test run with an aluminized mylar foil. The counting rate is about 1 Hz. Three measurements were taken: one without the foil, one with one layer of foil, and one with two layers of foil. For each measurement we took data over 10 min. For one layer of 0.25-mil aluminized mylar the thickness resolution can reach 1.6% for 10 minutes of data-taking.

### 2.2.3 Mercury electric-dipole-moment experiment

Y. Chen, E. N. Fortson, B. Graner, B. R. Heckel, and E. Lindahl

Atomic electric-dipole-moment (EDM) experiments offer perhaps the most sensitive probe of  $CP$  violation in theories of physics beyond the Standard Model and our measurements of the  $^{199}\text{Hg}$  EDM over the years have achieved the most precise EDM limit on any system. Searches in diamagnetic atoms such as  $^{199}\text{Hg}$  provide bounds on nuclear EDMs that would most likely originate from  $CP$  violating interactions between nucleons. The leading theoretical extension to the Standard Model, supersymmetry (SUSY), is expected to generate a  $^{199}\text{Hg}$  EDM comparable to our experimental limit. We recently published a new upper limit for the EDM of  $^{199}\text{Hg}$ :  $|d(^{199}\text{Hg})| < 3.1 \times 10^{-29} e \text{ cm}$ , a seven-fold improvement in the upper limit over our previous work<sup>1</sup>. This project is supported primarily by the NSF (P.I. Fortson, co-I. Heckel).

The current version of the  $^{199}\text{Hg}$  EDM apparatus uses ultraviolet (uv) laser light to polarize and measure the spin-precession frequency of  $^{199}\text{Hg}$  atoms in 4 vapor cells, 2 of which (the inner pair) have oppositely directed electric fields. All cells lie in a uniform magnetic field. The frequency difference between the inner pair of cells is sensitive to an EDM while the outer cells are used to monitor the magnetic field and its linear gradient. The experiment is now sensitive to spin-precession frequency shifts on the  $10^{-10}$ -Hz scale. A blind frequency offset is added to the inner-cell frequency difference to mask the EDM signal until the analysis of an entire data set is complete.

In the past year, we have made substantial improvements to the apparatus in preparation for a new round of EDM measurements. Our achievements include a  $4\text{-}\sigma$  measurement of the  $^{199}\text{Hg}$  spin-precession frequency shift, linear in the applied electric field, due to the interference of Stark-induced M1 and E2 transitions with the allowed E1 transition<sup>2</sup>. This Stark effect mimics an EDM and will be eliminated in future EDM data runs by allowing the  $^{199}\text{Hg}$  atoms to precess in the dark. We have developed a method to construct  $^{199}\text{Hg}$  vapor cells without the use of glue. Test cells using this new method have  $^{199}\text{Hg}$  spin-precession lifetimes in excess of 600 s. We have installed a new set of magnetic field coils. The new coils provide better field uniformity and are wound on an insulating frame to eliminate magnetic-field noise from fluctuating currents inherent in room-temperature conductors. We have developed an improved method to measure the high-voltage leakage currents that flow down the vapor-cell walls, a major source of systematic error. We have found that these leakage currents are at least 5 times smaller than the currents measured in our previous work.

We have reduced our system noise by an estimated factor of 4 and have reduced the dominant sources of systematic error by a factor of 5. Before undertaking a new round of  $^{199}\text{Hg}$  EDM measurements, two tasks remain: the construction of a new set of  $^{199}\text{Hg}$  vapor cells and the acquisition of a new uv laser system (on order) as the current laser system no longer produces sufficient uv light. We expect to begin EDM data taking by the end of 2012.

---

<sup>1</sup>W. C. Griffith *et al.*, Phys. Rev. Lett. **102**, 101601 (2009).

<sup>2</sup>T. H. Loftus, *et al.*, Phys. Rev. Lett. **106**, 253002 (2011)

### 2.2.4 Search for time-reversal symmetry violation in neutron decay: detailed analysis report on the emiT experiment

T. E. Chupp\*, R. L. Cooper\*, K. P. Coulter\*, S. J. Freedman†, B. K. Fujikawa†,  
A. García, G. L. Jones‡, H. P. Mumm§, J. S. Nico§, A. K. Thompson§, C. A. Trull¶,  
F. E. Wietfeldt¶, and J. F. Wilkerson||

The emiT collaboration worked on an experiment to search for the breaking of the time-reversal symmetry in neutron  $\beta$  decay. The  $\beta$ -decay rate depends on correlations between the momenta of the electron,  $\vec{p}_e$ , and neutrino,  $\vec{p}_\nu$ , and the average neutron angular momentum  $\langle \vec{J} \rangle$ :

$$d\Gamma \propto \left[ 1 + a \frac{\vec{p}_e}{E_e} \cdot \frac{\vec{p}_\nu}{E_\nu} + \frac{\langle \vec{J} \rangle}{J} \cdot \left( A \frac{\vec{p}_e}{E_e} + B \frac{\vec{p}_\nu}{E_\nu} + D \frac{\vec{p}_e}{E_e} \times \frac{\vec{p}_\nu}{E_\nu} \right) \right]$$

The triple correlation is even under parity ( $P$ ), but odd under motion reversal, the combination of time reversal ( $T$ ) and exchange of initial and final states. A measurement of  $D$  is sensitive to T-odd/P-even interactions among light quarks. For vector-axial-vector interactions only,  $D$  is also a measure of the complex phase of  $g_A/g_V$ .

The last three years have demanded significant attention from García who has been responsible for Monte Carlo calculations which played an important role in analyzing data and understanding systematic uncertainties. Although a brief article was published in 2011<sup>1</sup>, writing a detailed article that justifies uncertainties took a considerable effort. At the time of writing this report, the collaboration has prepared a long paper and seems close to agreement on submitting for publication soon.

---

\*Physics Department, University of Michigan, Ann Arbor, MI.

†Physics Department, University of California at Berkeley and Lawrence Berkeley National Laboratory, Berkeley, CA.

‡Physics Department, Hamilton College, Clinton, NY.

§National Institute of Standards and Technology, Gaithersburg, MD.

¶Physics Department, Tulane University, New Orleans, LA.

||Department of Physics and Astronomy, University of North Carolina, Chapel Hill, NC.

<sup>1</sup>Mumm *et al.*, Phys. Rev. Lett. **107**, 102301 (2011).

## 3 Accelerator-based physics

### Accelerator-based weak interactions

#### 3.1 Overview of the ${}^6\text{He}$ experiments at CENPA

A. García

The  ${}^6\text{He}$  experiments are moving along. We now have the most intense source of  ${}^6\text{He}$  in the world (see Sec. 3.1.1). We have worked on a determination of the  ${}^6\text{He}$  lifetime and resolved a long-standing discrepancy (see Sec. 3.1.2). Using the decay of tritium to fix a parameter to account for nucleon-delta excitations, the decay of  ${}^6\text{He}$  can be used to get the coupling constant in axial decays. Using our experimental determination of the  ${}^6\text{He}$  half-life in combination with *ab-initio* calculations of the matrix element yields an axial coupling constant in agreement with that of neutron decay. This is a further indication that the coupling constant does not get a significant renormalization in the nuclear medium.

We have also moved the laser systems from Argonne National Lab and installed them at UW. We have recently trapped about 30 atoms of  ${}^6\text{He}$  in a magneto-optical trap (MOT) (see Sec. 3.1.3). This will be used for searches for tensor currents in weak decays.

We are presently finalizing the design for the detection and electric field systems and are working on optimizing the laser systems.

##### 3.1.1 Production of ${}^6\text{He}$ at CENPA

Z. T. Alexander, T. M. Cope, A. García, G. C. Harper, R. Hong, A. Knecht,  
P. Müller\*, R. G. H. Robertson, D. W. Storm, H. E. Swanson, D. I. Will,  
W. Williams\*<sup>†</sup>, C. Wrede<sup>‡</sup>, and D. W. Zumwalt

We have recently published an article describing our source for the production of  ${}^6\text{He}$  and its performance<sup>1</sup>. This includes a re-analysis of the data presented in last year's report<sup>2</sup> that includes several factors that had not been accounted for. The achieved rates in our low-background area, Cave 1, is shown in Fig. 3.1.1-1.

We are continuing to improve the performance of our  ${}^6\text{He}$  source. During our last beam time we reliably achieved deuteron beam currents of about 12  $\mu\text{A}$  leading to extracted  ${}^6\text{He}$  well above  $10^9$  atoms/s. Due to the high power of such a beam ( $\sim 220$  W) we had to protect

---

\*Physics Division, Argonne National Laboratory, Lemont, IL.

<sup>†</sup>Department of Physics, Old Dominion University, Norfolk, VA.

<sup>‡</sup>Department of Physics and Astronomy and National Superconducting Cyclotron Laboratory, Michigan State University, East Lansing, MI.

<sup>1</sup>A. Knecht *et al.*, Nucl. Instr. Meth. A **660**, 43 (2011).

<sup>2</sup>CENPA Annual Report, University of Washington (2011) p. 51.

several bellows as they are easily punctured when hit by stray beam. In addition, the high neutron load at the target poses great challenges to our vacuum-control devices which are based on solid-state relays. We have “downgraded” the relevant vacuum control to a system based on mechanical relays.

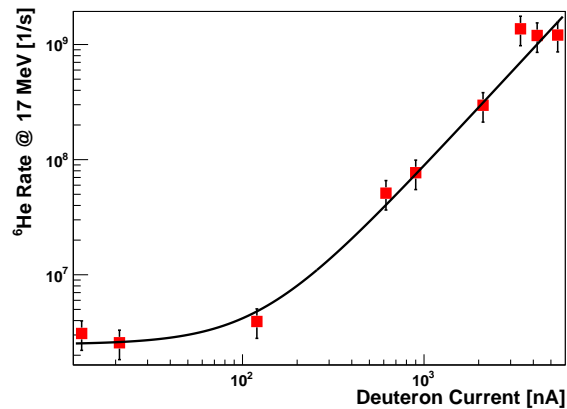


Figure 3.1.1-1. Measured  ${}^6\text{He}$  rates in the low-background area at the point where the  ${}^6\text{He}$  trapping apparatus will be installed.

While all the radioactivity produced in the lithium target is short-lived, the thin stainless-steel window that separates the lithium from the beam-line vacuum is a point of concern in case one has to access or exchange the lithium. Using a germanium detector we have identified  ${}^{56}\text{Co}$  with a half-life of 77 d as the main radioactive isotope produced in the stainless foil in copious amounts. Currently we are investigating aluminum or titanium as possible replacements both by irradiating them with a high-energy deuteron beam and analyzing the produced radioisotopes and also by reviewing their compatibility with lithium and as vacuum separation foils.

### 3.1.2 Precision measurement of the ${}^6\text{He}$ half-life and the weak axial current in nuclei

B. G. Delbridge, A. García, R. Hong, A. Knecht, P. Müller\*, H. E. Swanson, I. S. Towner<sup>†</sup>, S. Utsuno, W. Williams\*,<sup>‡</sup>, C. Wrede<sup>§</sup>, and D. W. Zumwalt

The decays of  ${}^3\text{H}$  and of  ${}^6\text{He}$  are special because these systems are light enough that the corresponding *ab-initio* calculations can be performed with precision. Using the case of  ${}^3\text{H}$  to fix nucleon-delta excitations, the matrix element for  ${}^6\text{He}$  can be calculated to within a few percent<sup>1</sup>. Precision measurement of the  ${}^6\text{He}$  half-life can provide a more solid experimental

\*Physics Division, Argonne National Laboratory, Lemont, IL.

<sup>†</sup>Cyclotron Institute, Texas A&M University, College Station, TX.

<sup>‡</sup>Department of Physics, Old Dominion University, Norfolk, VA.

<sup>§</sup>Department of Physics and Astronomy and National Superconducting Cyclotron Laboratory, Michigan State University, East Lansing, MI.

<sup>1</sup>S. Vaintraub, N. Barnea, and D. Gazit, Phys. Rev. C **79**, 065501 (2009).

value to test theories in order to resolve the issue of the quenching of the weak axial coupling constant,  $g_A$ . However, there is a major discrepancy among previous measurements, which makes the currently reported average and precision of  $806.7 \pm 1.5$  ms unreliable<sup>1</sup>.

We took data for one week in March, 2011, with a good production rate<sup>2</sup> of  ${}^6\text{He}$ . The experiment was conducted in a low-background area and an O-ring-sealed gate valve was used to seal the decay volume. We used two thin scintillators to detect the  $\beta$  particles in coincidence. Then we passed this pulse through four gate generators providing signals of fixed, non-extendable deadtimes. Subsequently, the four signals were fed into a CAMAC-based scaler together with the original coincidence signal and the signals from 1- and 100-kHz clocks. The signals from the 1-kHz clock also triggered the read-out of the scaler module via JAM and provided 1-ms time stamps to our data stream.

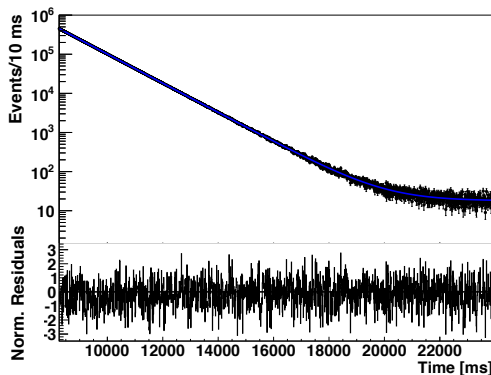


Figure 3.1.2-1.  ${}^6\text{He}$  decay curve for the data with initial rates  $<40$  kHz and the stainless-steel insert removed, with the corresponding residuals. The  $\chi^2/\text{dof}$  of the fit has a typical value of 1578.2/1562.

The data were fit to the function  $R(t) = N(\exp(-(t - t_0)/\tau) + b)$ , where the lifetime  $\tau$  and the background  $b$  are free parameters while  $N$  is set by the total number of counts, as is shown in Fig. 3.1.2-1 with the corresponding residuals. We carefully inspected systematic effects such as deadtime corrections, deadtime drift, background,  ${}^8\text{Li}$  contamination, gain shift,  ${}^6\text{He}$  diffusion, clock accuracy and afterpulsing. We reported our  ${}^6\text{He}$  half-life<sup>3</sup> of  $806.89 \pm 0.11_{\text{stat}} \pm 0.23_{\text{syst}}$  ms, which improved the precision over the currently reported value by a factor of 6. We further determined the  $ft$ -value for this decay to be  $803.04^{+0.26}_{-0.23}$  s. Our extracted Gamow-Teller matrix element of  $|M_{\text{GT}}| = 2.1645(43)$  agrees within a few percent with *ab-initio* calculations using the weak axial coupling constant  $g_A$  measured in free-neutron decay. It is clear that there is no need here for the  $\sim 30\%$  quenching of  $g_A$  needed for shell-model calculations of sd-shell nuclei performed in a restricted base<sup>4</sup>.

In 2012 we plan to take a measurement making use of a digitizing system that should allow us to further reduce systematic uncertainties.

<sup>1</sup>F. Ajzenberg-Selove, Nucl. Phys. A **413**, 1 (1984).

<sup>2</sup>A. Knecht *et al.*, Nucl. Instr. Meth. A **660**, 43 (2011).

<sup>3</sup>A. Knecht *et al.*, Phys. Rev. Lett. **108**, 122502 (2012).

<sup>4</sup>W.-T. Chou, E. K. Warburton, and B. A. Brown, Phys. Rev. C **47**, 163 (1993).

### 3.1.3 $^6\text{He}$ laser-trap setup

A. García, G. C. Harper, R. Hong, A. Knecht, P. Müller\*, H. E. Swanson, W. Williams\*, and D.W. Zumwalt

Presently we are trapping  $^6\text{He}$  atoms using a magneto-optical trap (MOT)<sup>1</sup>. The atoms are excited to the  $2^3\text{S}_1$  metastable state at 19.82 eV above the ground state via a radio frequency plasma discharge (Fig. 3.1.3-1). The 1083-nm trap laser cycles between this metastable state and the  $2^3\text{P}_2$  state.

Since last March we transported the entire trapping apparatus from Argonne National Laboratory to Seattle. We successfully trapped  $^4\text{He}$  soon thereafter and have reached sufficient trapping efficiencies to begin trapping  $^6\text{He}$ . To reach this goal, we made a number of developments in the trapping of  $^6\text{He}$ , including the addition of a locked 706-nm probe laser. When imaging the MOT using only 1083-nm light, our photodetector sees a combination of atomic fluorescence and background scattered light from the trapping lasers. The introduction of additional cycling with the 706-nm probe laser in combination with a photodetector with much higher sensitivity to 706-nm light than to 1083-nm light enhances our ability to image only the MOT by discriminating between these light sources.

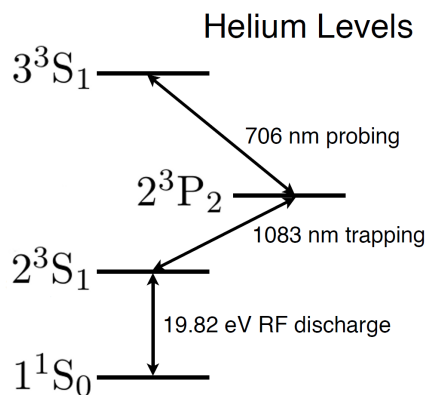


Figure 3.1.3-1. Relevant energy levels for laser trapping of helium.

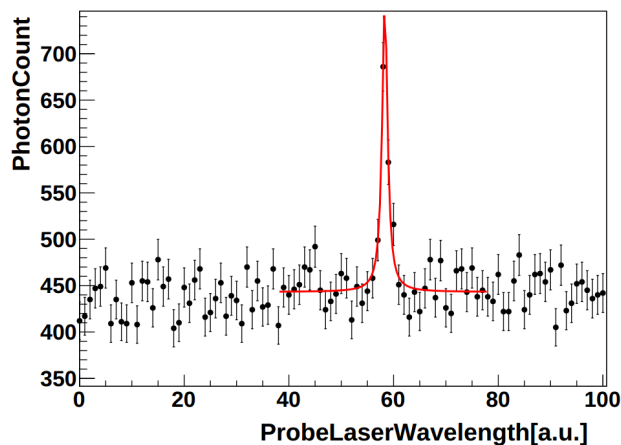


Figure 3.1.3-2. As the frequency of the 706-nm probe laser is swept over the atomic resonance of  $^6\text{He}$  more light is scattered into the photodetector, indicating trapped atoms.

For our first attempt at measuring trapped  $^6\text{He}$ , we followed the usual scheme for achieving a MOT<sup>1</sup>, followed by scanning the frequency of the 706-nm light over the 2P to 3S resonance. We can determine the atom number from the photon flux of the scattered 706-nm light (Fig. 3.1.3-2), and we now report our first successful  $^6\text{He}$  trap.

To date we have managed  $^6\text{He}$  trap rates of  $\sim 30$  atoms/s as calculated from the photon flux. We expect to reach trap rates of  $\sim 1000$  atoms/s at our present level of  $^6\text{He}$  production,

\*Physics Division, Argonne National Laboratory, Lemont, IL.

<sup>1</sup> Metcalf, "Laser Cooling and Trapping" (1999).

so our trapping efficiency is lower than is achievable. We have identified metastable plasma quenching due to  $\text{H}_2$  contamination as the likely source of this inefficiency, and a number of techniques to reduce the partial pressure of  $\text{H}_2$  have been attempted. We have made promising headway to reduce the contamination, and this work is ongoing. We will begin trapping  $^6\text{He}$  again at the end of April.

### 3.1.4 Investigation of vacuum separation foils with minimal energy loss for $\beta$ particles

Y.S. Bagdasarova, A. García, and A. Knecht

The high outgassing of the materials used in the construction of the  $\beta$  detector prevents ultra-high vacuum from being sustained within the chamber of the MOT. Consequently, a thin, impermeable foil needs to be placed between the chamber and the detector. The foil should be able to withstand a 1-atm differential pressure while being as thin as possible in order not to affect the  $\beta$ s. Although the default option is to employ a 125- $\mu\text{m}$  beryllium foil, vacuum and simulation results on Kapton polyimide films indicate that it may be a better option.

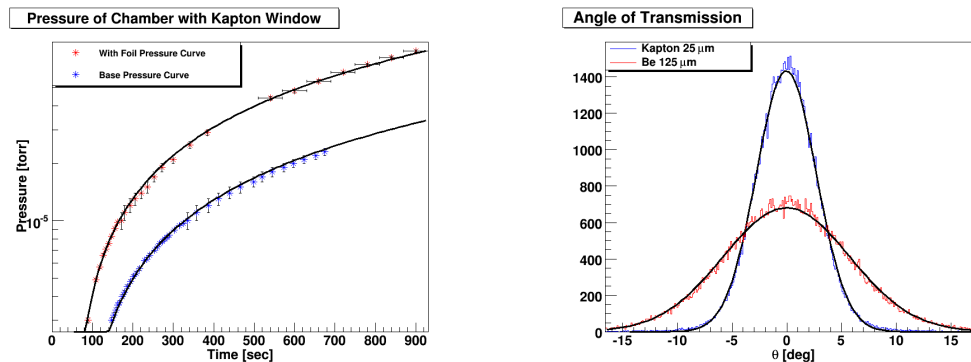


Figure 3.1.4-1. Left: Rise in chamber pressure over time with (red) and without (blue) 25- $\mu\text{m}$  Al-coated Kapton window in place. Right: Simulated angular distribution of transmitted  $\beta$ s through 25- $\mu\text{m}$  Kapton (blue) and 125- $\mu\text{m}$  beryllium (red) foil at normal incidence and 1500 keV.

Basic pressure tests were performed on regular Kapton and aluminum-coated Kapton to assess their durability and performance under vacuum. The thinnest foil to withstand 1 atm was 25  $\mu\text{m}$  thick. In order to measure its leakage rate we attached the foils to a vacuum chamber and measured the rise in pressure over time upon isolating the chamber from the turbo pump. Fig. 3.1.4-1 shows the obtained pressure curves and their fits for Al-coated Kapton. The foil leak rate is obtained by taking the difference between the leak rate of the chamber with and without the foil in place. The measured rates for 25- $\mu\text{m}$  uncoated Kapton and Al-coated Kapton were  $4 \times 10^{-6}$  and  $2 \times 10^{-4}$  L-Torr/sec, respectively. It is unclear why the coated Kapton foil had such an elevated leak rate. However, the leakage rate of the uncoated foil is at an acceptable level. The minimum pressures reached after pumping with the Kapton and Al-Kapton foils were  $7.1 \times 10^{-7}$  and  $1.1 \times 10^{-6}$  Torr respectively, while the minimum pressures with thick plates in place of the foils were  $2.9 \times 10^{-7}$  and  $3.6 \times 10^{-7}$  Torr.

PENELOPE, a Monte Carlo simulation package, was used to simulate the transmission of monoenergetic electrons through 25  $\mu\text{m}$  of Kapton and 125  $\mu\text{m}$  of beryllium at various angles of incidence (Fig. 3.1.4-1.) At 1500 keV the average energy loss is 3 keV (2 keV FWHM) for Kapton and 24 keV (10 keV FWHM) for beryllium while at the same time the angular spread of the  $\beta$ s after their passage is much reduced for Kapton.

### 3.2 Experimental validation of the largest calculated isospin-symmetry-breaking effect in a superallowed Fermi decay

C. Bordeanu\*, A. Garca, J. C. Hardy†, V. E. Iacob†, D. Melconian†, N. Nica†, H. I. Park†, G. Tabacaru†, I. S. Towner†, L. Trache†, S. Triambak‡, R. E. Tribble†, and Y. Zhai†

Models to calculate small isospin-symmetry-breaking effects in superallowed Fermi decays have been placed under scrutiny in recent years. A stringent test of these models is to measure transitions for which the correction is predicted to be large. In 2001 we made a proposal to run an experiment at Texas A&M to determine the  $\beta$ -decay branches of  $^{32}\text{Cl}$ . The idea was to collect  $^{32}\text{Cl}$  in a tape and transport it to a counting location where  $\beta - \gamma$  coincidences could be measured with a precisely calibrated high-purity germanium detector and deduce from it the  $\beta$  branches.

We were then motivated by trying to minimize systematic uncertainties in a determination of isospin-symmetry breaking in the decay of  $^{32}\text{Ar}^1$ . The  $^{32}\text{Cl}$  experiment ran smoothly in 2001 led by then-postdoctoral fellow Dan Melconian with much help from the Texas A&M team and others from Seattle. The data analysis involved many details that required much attention and this took time.

The precision on the  $\gamma$  yields for most of the known  $\beta$  branches was improved by about an order of magnitude from previous experiments, and many new transitions were observed. We determined  $^{32}\text{Cl}$ -decay transition strengths extending up to  $E_x \sim 11$  MeV. The  $ft$  value for the decay to the isobaric-analog state in  $^{32}\text{S}$  was measured and we discovered that there was a large isospin-symmetry breaking in  $^{32}\text{S}$  and that this could be used to test the calculations that are used for extracting  $V_{ud}$ .

Our measurement found the isospin-symmetry-breaking correction to the superallowed transition of this decay to be  $(\delta_C - \delta_{NS})_{\text{exp}} = 5.4(9)\%$ , significantly larger than for any other known superallowed Fermi transition. The shell-model calculation yielded  $(\delta_C - \delta_{NS})_{\text{theo}} = 4.8(5)\%$  in reasonable agreement with the measurement. These results have now been published<sup>2</sup>.

---

\*Horia Hulubei National Institute for Physics and Nuclear Engineering, Bucharest-Magurele, Romania.

†Department of Physics, Texas A&M University, College Station, TX.

‡Present address: Department of Physics & Astrophysics, University of Delhi, Delhi 110 007, India.

<sup>1</sup>M. Bhattacharya *et al.*, Phys. Rev. C **77**, 065503 (2008).

<sup>2</sup>D. Melconian *et al.*, Phys. Rev. Lett. **107**, 182301 (2011) and Phys. Rev. C **85**, 025501 (2012).

## 4 Precision muon physics

### 4.1 Overview of the muon physics program

J. Crnkovic, A. García, N. Froemming, D. W. Hertzog, P. Kammel, J. Kaspar, B. Kiburg, S. A. Knaack, M. H. Murray, D. J. Prindle, F. Wauters, P. Winter, and T. Zhao

The Precision Muon Group is involved in a series of fundamental experiments that determine Standard-Model parameters, low-energy effective-field-theory constants, or provide sensitive tests for new physics. This is the second year for our program at CENPA. The efforts are in full swing and the group has expanded considerably. The transition from bridge NSF funding to support from the DOE Office of Nuclear Physics is complete. Physics highlights are given below with details supplied in the accompanying sections. Briefly, we finished the analysis of the MuCap determination of  $g_P$  and are nearly complete with the analysis of two hadronic cross section measurements related to  $g - 2$  hadronic vacuum polarization. Our long paper summarizing MuLan's 1-ppm measurement of  $\tau_{\mu^+}$  and 0.6-ppm determination of  $G_F$  is in a mature draft. A 12-week run of MuSun acquired our first physics data set. Considerable progress has been made on  $g - 2$  detector development and in advancing the design of the experiment as a whole. The active muon projects are:

- The MuCap experiment at the Paul Scherrer Institute (PSI) in Switzerland measures the negative-muon lifetime in high-purity protium gas. The difference between  $\tau_{\mu^-}$  and  $\tau_{\mu^+}$  (from MuLan<sup>1</sup>) determines the  $\mu p$  capture rate  $\Lambda_s$ . The capture rate can be used to obtain the weak-nucleon pseudo-scalar coupling  $g_P$ , which is the experimentally least known of the weak-nucleon couplings, despite being precisely predicted by fundamental low-energy QCD-based theory. The final data sample, obtained in 2006 and 2007 has 10 times the statistics compared to that used in a preliminary publication. These data presented considerable challenges, requiring years to analyze owing to a myriad of potential subtle systematic effects. This work is complete and the results were announced for the first time in an invited session at the April, 2012 APS meeting by Peter Winter. We find the preliminary result that  $g_P = 8.1 \pm 0.5$ , which is in excellent agreement with the QCD-based prediction of  $8.26 \pm 0.23$ . It is the first unambiguous determination of  $g_P$  and a clear confirmation of a firm and important theoretical prediction. We note that lead Ph.D. student Kiburg completed his degree in May, 2011 and stayed on in our group for a 1-year postdoc position to work on the last phase of the analysis and on the  $g - 2$  detector development (see below). He has recently accepted a prestigious Lederman Fellowship at Fermilab. Graduate student Knaack is completing her Ph.D. thesis on a precision measurement of molecular formation, which is essential for the interpretation of the MuCap experiment.
- MuSun is built on the MuLan and MuCap techniques developed at PSI. Like MuCap, it is a measurement of the negative-muon lifetime in a gaseous tracking chamber. Here

---

<sup>1</sup>D. M. Webber, *et al.*, Phys. Rev. Lett.**106**, 041803 (2011).

we use ultra-pure deuterium and hold the temperature at approximately 30 K to reduce unwanted molecular processes, including muon-catalyzed fusion. The capture process on the deuteron is one of the simplest two-nucleon weak interactions and the physics involved has aspects in common with both  $pp$  fusion in the sun and neutrino breakup of deuterium, as used in the SNO experiment. For all three processes, effective field theory is quite precise, up to an unknown low-energy constant. By establishing a precise measurement for the  $\mu d$  capture rate, we will fix this LEC, which is common for the other two processes. In the summer of 2011 we completed the first physics data taking with the full cryogenic TPC and all appropriate ancillary measuring equipment. These data are being analyzed by senior Ph.D. student Murray and postdoc Wauters, along with a broader team from our international collaboration. In parallel to the analysis, we have begun lab work here at UW to develop new cryo-amplifiers and have made a test setup with a duplicate TPC module to study electronics and pad optimization; both are important improvements we intend to implement prior to the final data taking runs in 2013 and 2014.

- One of the strongest hints at new physics is the persistent difference between the measurement and Standard-Model prediction for the muon anomalous magnetic moment. Both are known to  $\sim 0.5$ -ppm precision. The current discrepancy  $a_\mu(Expt - Thy) = (281 \pm 80) \times 10^{-11}$  is suggestive, but not yet definitive, about new physics at the TeV scale. We proposed a next-generation muon  $g - 2$  experiment with a factor of 4 or more improved overall precision. Now approved, it represents one of the flagship experiments in the new Intensity Frontier effort at Fermilab. Besides a strong role in the overall project leadership, our group is making key technical contributions through the development of new electromagnetic calorimeters and their readout systems, which are required for a high-rate environment. Our focus over the past year has been on  $PbF_2$  crystals and silicon photomultiplier readout, using custom pulse-optimizing electronics boards designed at CENPA. We are also involved in the simulation effort in general, in the muon delivery (beam) design, and the precision magnetic-field measuring effort. A related project is our analysis of Belle initial-state-radiation data to determine multi-hadron cross sections, which are needed to reduce the uncertainty on the hadronic vacuum polarization contribution to the muon anomaly. Graduate student Crnkovic, now assisted by postdoc Jarek Kaspar, is nearly finished with the analysis of two channels, which are described separately.

## MuCap

### 4.2 Overview of the MuCap experiment and technique

D. W. Hertzog, P. Kammel, B. Kiburg, S. A. Knaack, and P. Winter

The elementary electroweak process  $\mu^- p \rightarrow n \nu_\mu$  of ordinary muon capture (OMC) is an excellent probe of the helicity structure of the weak interaction. The OMC process involves  $g_V(q_0^2)$ ,  $g_M(q_0^2)$ ,  $g_A(q_0^2)$ , and  $g_P(q_0^2)$ ; i.e., the nucleon's vector, magnetic, axial, and pseudo-scalar form factors, respectively. The relevant momentum transfer is given by  $q_0^2 = -0.88m_\mu^2$ .

Since  $g_V$ ,  $g_M$ , and  $g_A$  are well-known from other processes, the measurement of the singlet capture rate  $\Lambda_S$  of the OMC process allows for a determination of  $g_P$ . This quantity mainly arises from the coupling of the axial current to an intermediate pion. By now, the dominant pion-pole term as well as higher-order corrections are systematically calculated within heavy-baryon chiral perturbation theory and its underlying concept of chiral symmetry breaking. Thus, an experimental confirmation of the predicted ChPT result<sup>1</sup>  $g_P = 8.26 \pm 0.23$  is an important test of QCD symmetries at low energies.

The experimental determination of  $g_P$  spans a long history including both OMC efforts and one experiment<sup>2</sup> using radiative muon capture (RMC). As can be seen from Fig. 4.2-1, the interpretation of the earlier experimental results is unclear because the OMC<sup>3</sup> and RMC results depend significantly on the molecular ortho-para transition rate  $\lambda_{op}$ . While details about the formation of  $pp\mu$  molecules can be found in reviews<sup>4</sup>, it is important to note that the use of a low-density gas target at 1% liquid hydrogen density in MuCap is essential to allow the extraction of  $g_P$  nearly independently of the poorly known rate  $\lambda_{op}$ .

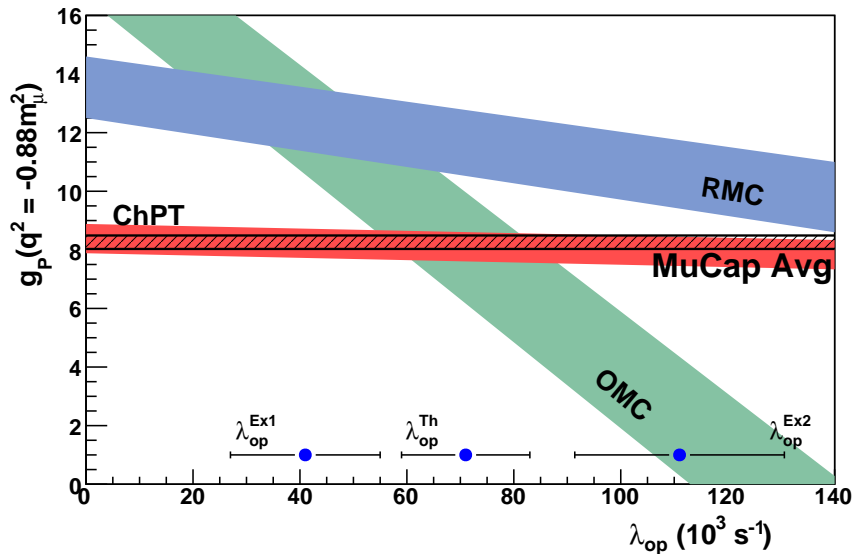


Figure 4.2-1. Previous most precise result from OMC<sup>3</sup> and RMC<sup>2</sup> compared to the ChPT prediction<sup>1</sup> for  $g_P$ . Both experiments significantly depend on the poorly known molecular rate  $\lambda_{op}$ . The MuCap result<sup>3</sup> is almost independent of  $\lambda_{op}$  due to the chosen experimental conditions.

The MuCap experiment was performed at the high-intensity muon beamline  $\pi E3$  at the Paul Scherrer Institute, Switzerland. Muons enter the central TPC where they stop in the hydrogen gas. The muon's arrival is initially registered in the muon-entrance scintillator and a two-plane wire chamber. Upon registering a muon arrival, an electrostatic kicker deflects

<sup>1</sup> V. Bernard, N. Kaiser, U.-G. Meissner, Phys. Rev. D **50**, 6899 (1994); N. Kaiser, Phys. Rev. C **67**, 027002 (2003).

<sup>2</sup> D. H. Wright, *et al.*, Phys. Rev. C **57**, 373 (1998).

<sup>3</sup> G. Bardin, *et al.*, Nucl. Phys. A **352**, 365 (1981).

<sup>4</sup> P. Kammel, K. Kubodera, Annu. Rev. Nucl. Part. Sci. **60**, 327 (2010); T. Gorringer, H. W. Fearing, Rev. Mod. Phys. **76**, 31 (2004).

the incoming beam to prevent additional muons from entering the target during a 25- $\mu$ s measurement period in the TPC. Pileup of a second muon due to the finite beam extinction is detected in the entrance counters with high efficiency and only leads to a small systematic effect on the lifetime. Ultra-high purity of the 10-bar hydrogen gas in the TPC was provided by constant circulation through an external cleaning unit<sup>1</sup> reducing chemical contaminants to concentrations of less than 10 ppb. Isotopic purity of better than 6 ppb was achieved by an initial purification using a cryogenic distillation column that separates isotopes based on the difference in vapor pressure for hydrogen and deuterium. Such high elemental and isotopic purity levels are crucial to reduce any effects from capture on non-hydrogen atoms which can distort the result for the singlet rate  $\Lambda_S$ . At our concentration levels, these effects are small and well under control. In addition, the experimental setup enables us to monitor and measure the effects stemming from muon capture on chemical impurities.

The full reconstruction of the muon track by means of the TPC data allows for the selection of muons stopping far away from any wall material. The decay electrons' trajectories are reconstructed in the cylindrical wire chambers surrounding the TPC. A segmented scintillator hodoscope on the outside provides fast timing information for the decay electrons. The high statistics of  $\sim 1.5 \cdot 10^{10}$  decays allows for a precise measurement of the negative muons' lifetime in hydrogen. The singlet capture rate  $\Lambda_S$  can then be inferred from the difference of the negative muon's lifetime in hydrogen measured in MuCap and the positive muon's lifetime measured in MuLan<sup>2</sup>. After the data for our initial result<sup>3</sup> were taken, the MuCap system underwent some important upgrades including the isotopic purification by means of the deuterium separation column, an improved electronics readout system and the integration of the electrostatic kicker. Since then, we have finished collecting the final statistics during 2006 and 2007. The analysis of the full statistics, exceeding the published data by an order of magnitude, is described in the following section (see Sec. 4.2.1). A dedicated measurement to reduce one of our main systematic errors in the published result stemming from the uncertainty in the molecular formation rate  $\lambda_{pp\mu}$  is described thereafter (see Sec. 4.2.2). The current, still preliminary, result of the MuCap experiment is presented in Fig. 4.2-1. It is the first precise and unambiguous measurement of  $g_P$ . Its dependence on  $\lambda_{op}$  is almost negligible. The MuCap result is in excellent agreement with theory. It excludes any dramatic breakdown of the chiral predictions, as initially suggested by the RMC result, and resolves a long-standing puzzle concerning the nucleon's least known electro-weak form factor.

#### 4.2.1 Finalized analysis for the singlet capture rate

D. W. Hertzog, P. Kammel, B. Kiburg, S. A. Knaack, and P. Winter

The main analysis of the MuCap experiment extracts the lifetime of negative muons stopped in the hydrogen gas in order to infer the singlet capture rate  $\Lambda_S$  for the OMC process. The decay time for each event is given by the time difference of the electron scintillator hodoscope and the muon entrance scintillator and histogrammed to extract the muon's lifetime. The

<sup>1</sup>V. Ganzha, *et al.*, Nucl. Instrum. Methods A **578**, 485 (2007).

<sup>2</sup>D. M. Webber, Phys. Rev. Lett. **106**, 041803 (2011).

<sup>3</sup>V. Andreev, *et al.*, Phys. Rev. Lett. **99**, 032002 (2007).

TPC signals allow for a reconstruction of the stopping muon's track. The outgoing decay electron track is reconstructed from the signals of the electron wire chambers. While these muon and electron tracks are not necessarily needed for the timing measurement, they offer crucial handles on suppressing background events that could distort the measured lifetime. One of the most important classes of such events include muons that do not stop in the pure hydrogen gas but in some frame material introducing an additional fast capture time component. Hence, careful studies of the stability of the extracted lifetime for variation of these cut parameters was performed to exclude any significant time distortions.

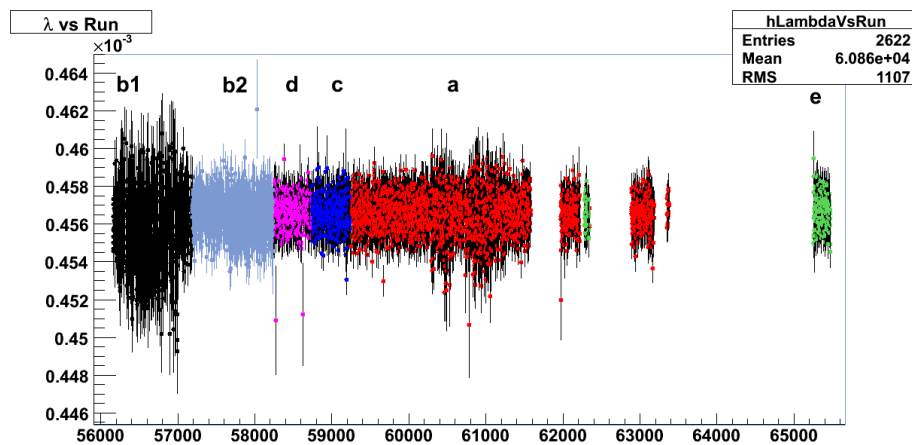


Figure 4.2.1-1. Lifetime versus individual run files for  $\mu^-$  data taken in 2007. The gaps starting above run number 61000 are due to a change in the beam polarity to deliver  $\mu^+$ .

The final statistics resulted in  $\sim 1.5 \times 10^{10}$  negative muon decays amounting to a total of 54 TB of stored data. As a first step, the raw information is translated into physical objects like muon and electron tracks. Due to its processor intensiveness, this stage was only performed twice. The subsequent analysis involved the fine-tuning of the selection criteria of muon-electron coincidences. Scanning this highly-dimensional parameter space required several iterations of this subsequent analysis. The most crucial part was a careful fine-tuning of the requirements imposed on the muon track. While more stringent cuts would usually improve the suppression of time distortions caused by physics effects (such as capture on frame material), they can also couple to subtle detector effects. Hence, a very careful optimization of the quest for stringent cuts due to physics and the necessity of relaxing these to avoid detector related systematics has been the major work. At this moment, the entire data analysis has been successfully finished. Fig. 4.2.1-1 shows the stability of the fitted lifetime for all of our  $\mu^-$  data taken in 2007 as an example of the overall consistency observed. To avoid any bias in the analysis, our clock frequency was blinded with an offset secret to the analyzers. In the meantime, the collaboration settled on all necessary corrections that need to be applied and all systematic errors were evaluated. The overall unblinding offsets were revealed at the last collaboration meeting. The current result for the pseudoscalar form factor measured by MuCap is  $g_P = 8.1 \pm 0.5$ , in agreement with the prediction from chiral perturbation theory ( $8.26 \pm 0.23$ ).

### 4.2.2 Finalized analysis of the molecular rates

D. W. Hertzog, P. Kammel, B. Kiburg, S. A. Knaack, and P. Winter

The MuCap experiment (see Sec. 4.2) measures the  $\mu^-$  lifetime in a gaseous hydrogen TPC to obtain the  $\mu p$  singlet capture rate  $\Lambda_S$ . Due to the chosen experimental conditions, corrections to the extracted capture rate originating from the formation of muonic molecules are suppressed compared to measurements in liquid hydrogen, but are not negligible. After a muon stops in the TPC and forms a  $\mu^- p$  atom, collisions with other hydrogen atoms can lead to the formation of molecular hydrogen  $pp\mu^-$  at the rate  $\lambda_{pp\mu}$ . Muon capture from the molecular state is slower than from the singlet state and  $\lambda_{pp\mu}$  must be known to correctly extract  $\Lambda_S$  from the pure hydrogen data. The current knowledge of the molecular formation rate is based on a series of measurements with varying results and methods. The world average,  $\lambda_{pp\mu} = 2.3(5) \times 10^6 \text{ s}^{-1}$ , is consequently determined to only  $\approx 22\%$  relative precision. That uncertainty in  $\lambda_{pp\mu}$  potentially contributes a systematic error that is of the same magnitude as the statistical precision for the final MuCap result. An improved measurement of  $\lambda_{pp\mu}$  to reduce this systematic uncertainty is now complete.

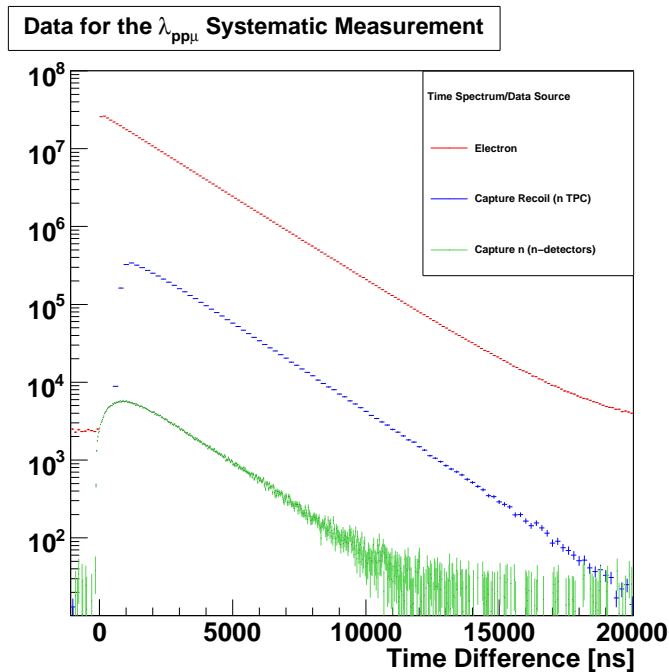


Figure 4.2.2-1. Time spectra of the argon-doped hydrogen data. The electron decay spectrum with  $\sim 5 \times 10^8$  events is shown in red. The histograms in blue and green are the time spectra of recoiling nuclei ( $4 \times 10^6$ ) and neutrons ( $5 \times 10^5$ ) from muon capture onto the argon nucleus.

A new determination of  $\lambda_{pp\mu}$  is based on data obtained using an argon-doped hydrogen gas (18.5 ppm atomic concentration) in the TPC, which is otherwise operated identically to the undoped data. Argon introduces additional atomic processes involving the muon. These are: a transfer rate  $\Lambda_{pAr}$  from the singlet  $\mu^- p$  state that leaves the  $\mu^-$  in a bound state with the argon nucleus in an energetically favorable transition; and a capture rate on

the argon nucleus  $\Lambda_{Ar}$ , which is  $\sim Z^4$  larger than the  $\Lambda_S$  capture rate. These kinetics are observed in the muon-decay electron and the direct capture time spectra, which are then fit to extract the rate  $\lambda_{pp\mu}$ . Fig. 4.2.2-1 shows the three relevant time spectra of this analysis. The highest-statistics spectrum is the muon-decay-electron time distribution, which is the most precise constraint in the fits. The other two spectra are obtained from capture events onto argon, based on the detection of either neutrons (green) or recoiling nuclei (blue). The new molecular formation rate result is  $\lambda_{pp\mu} = 1.883(65) \times 10^6 \text{ s}^{-1}$ , which is determined from the decay electron time spectrum analysis. We measure the effective molecular formation rate to 3.5% relative precision, which is a five-fold improvement on the previous world average. The present result improves the experimental interpretation and extraction of the  $\Lambda_S$  singlet capture rate result. The systematic error due to the uncertainty in the molecular formation rate is reduced from  $4.3 \text{ s}^{-1}$  to better than  $1 \text{ s}^{-1}$ .

## MuSun

### 4.3 Muon capture on deuterium, the MuSun experiment

D. W. Hertzog, P. Kammel, M. H. Murray, D. J. Prindle, P. Winter, and F. Wauters

The goal of the MuSun experiment<sup>1</sup> is a measurement of the rate  $\Lambda_d$  for the semileptonic weak process  $\mu^- + d \rightarrow \nu_\mu + n + n$  to a precision of better than 1.5%.  $\Lambda_d$  denotes the capture rate from the doublet hyperfine state of the muonic deuterium atom in its  $1s$  ground state.

Muon capture on the deuteron is the simplest weak-interaction process on a nucleus that can both be calculated and measured to a high degree of precision (see the discussion in a recent review of this field<sup>2</sup>). Effective field theories (EFTs) have been developed to calculate electro-weak observables in few-body systems, following Weinberg's pioneering work. The standard nuclear-physics approach (SNPA), based on the impulse approximation with explicit modeling of two-body current contributions, is being replaced by less model-dependent hybrid EFT<sup>3</sup> and pionless EFT<sup>4</sup> calculations. Very recently fully self-consistent calculations in a rigorous QCD-based EFT scheme have been published (Table 4.3-1). These calculations can establish quantitative relations between muon capture and electro-weak astrophysical processes of fundamental importance, which have never been measured directly. These include  $pp$  fusion, which is the primary energy source in the Sun and other main-sequence stars, and the  $\nu d$  reaction, which provided convincing evidence for solar neutrino oscillations at the Sudbury Neutrino Observatory.

While  $\mu d$  capture could serve as the benchmark for the axial-current interaction in the two-nucleon system, the present experimental situation is inadequate to provide much guidance.

<sup>1</sup><http://muon.npl.washington.edu/exp/MuSun>.

<sup>2</sup>P. Kammel, K. Kubodera, *Annu. Rev. Nucl. Part. Sci.* **60**, 327 (2010).

<sup>3</sup>S. Ando, T.-S. Park, K. Kubodera, and F. Myhrer, *Phys. Lett.* **B533**, 25 (2002); P. Ricci, and E. Truhlik, *arXiv:1012.2216* (2010); L. E. Marcucci *et al.*, *Phys. Rev. C* **83**, 014002, (2011).

<sup>4</sup>J.-W. Chen, X.-d. Ji, and Y.-c. Li, *Phys. Lett.* **B620**, 33 (2005).

The best existing experiments<sup>1</sup> are not precise enough and the most precise result differs from modern theory by almost three standard deviations. If true, such a discrepancy would have major ramifications for the above-mentioned astrophysics processes. The prospect of a precise MuSun result has stimulated recent calculations and first steps were taken towards a fully self-consistent EFT treatment. Results since 1980 are compiled in Table 4.3-1.

$\Lambda_d$	year	Method	Reference
386	2001	EFT*	Ando, Phys. Lett. B <b>533</b> , 25-36
$416 \pm 6$	2009	SNPA, EFT*	Ricci, Nucl. Phys. A <b>837</b> , 110
$392.0 \pm 2.3$	2011	EFT*	Marcucci, Phys. Rev. C <b>83</b> 014002
$399 \pm 3$	2012	EFT	Marcucci, Phys.Rev.Lett. <b>108</b> , 052502
$383.8-392.4$	2012	EFT	Adam, Phys. Lett. B <b>709</b> , 93-100
$470 \pm 29$	1986	Electron	Bardin, Nucl. Phys A <b>453</b> , 591-604
$409 \pm 40$	1989	Neutron	Cargnelli <sup>2</sup>

Table 4.3-1. Recent theoretical and experimental results on muon capture rate  $\Lambda_d$  from the doublet state of the  $\mu d$  atom. EFT\* denotes a hybrid EFT calculation. “Electron” denotes that the capture rate was measured with the lifetime technique, in contrast to deriving this rate from the capture neutrons.

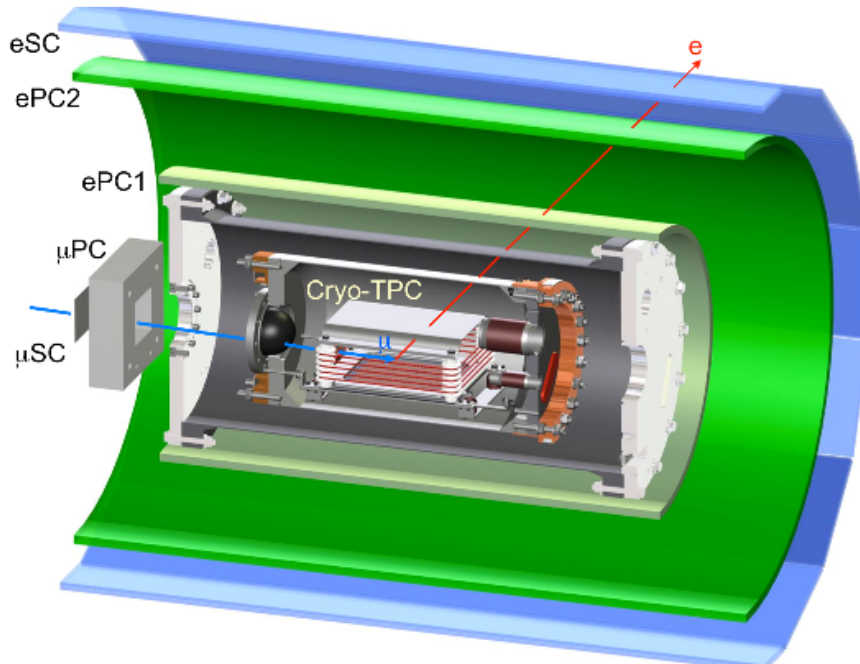


Figure 4.3-1. Drawing of the MuSun muon and electron detectors.

The MuSun experiment, shown in Fig. 4.3-1, measures  $\Lambda_d$  with the so-called lifetime technique:  $\lambda_{\mu d} = \lambda_{\mu^+} + \Lambda_d$ . Most parts of the detector are inherited from MuCap, including the muon entrance detectors (two thin scintillator slabs and a wire chamber) and the electron detector (two cylindrical wire chambers surrounded by a hodoscope consisting of a double

<sup>1</sup>G. Bardin *et al.*, Nucl. Phys. **A453**, 591 (1986); M. Cargnelli *et al.*, in Proceedings of the XXIII Yamada Conf. on Nuclear Weak Processes and Nuclear Structure, Osaka, Japan, (1989).

layer of scintillator paddles). However, the condition of the active target must lead to an unambiguous extraction of  $\Lambda_d$ , independent of muonic atomic physics complications occurring after the muon stops in deuterium (Fig. 4.3-2). The transition between the upper  $\mu d$  quartet to the lower  $\mu d$  hyperfine state,  $\lambda_{qd}$ , is slow and, once a  $dd\mu$  molecule is formed, muon-catalyzed  $dd$  fusion occurs on a time scale of nanoseconds, recycling the muon. Our studies demonstrated that atomic physics uncertainties are reduced to a negligible level at optimized target conditions of  $T = 30$  K and 6% liquid hydrogen density (Fig. 4.3-2).

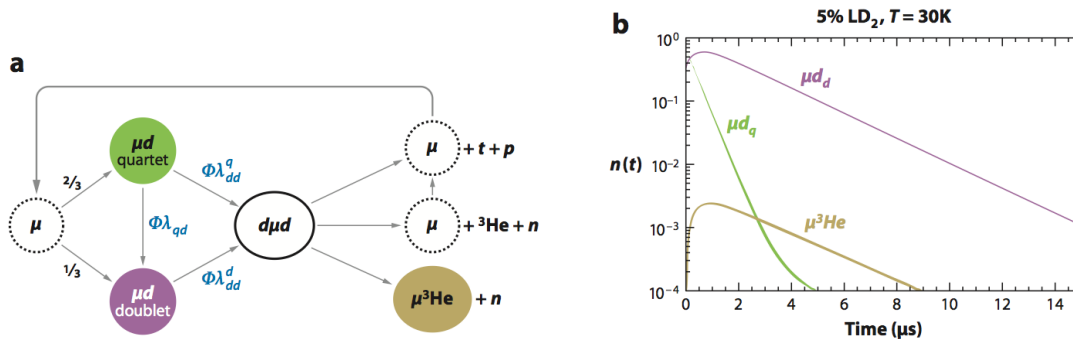


Figure 4.3-2. Left: The complex molecular dynamics of negative muons in  $D_2$ . Right: At the optimized target condition, the majority of the muons populate the  $\mu d$  doublet state after  $2 \mu s$ .

A new high-density cryogenic ionization chamber (CryoTPC) filled with ultra-pure deuterium was developed as an active target to monitor the muon stopping location and muon-catalyzed fusion reactions. The full waveforms of the TPC signals are digitized and stored using flash ADCs. Optimization of the energy resolution and the anode pad geometry is crucial for clean identification of muon stops and detection of fusion and capture products. The higher target density of the MuSun TPC (5 times that of MuCap) prevents the use of gas amplification and necessitates drift voltages up to 100 kV.

After two commissioning runs in 2010, a 12-week production data run was collected during summer 2011 in the  $\pi E3$  area of the Paul Scherrer Institute. This year, the  $\pi E1$  beam area will be extended, providing the MuSun experiment with a dedicated location for its detectors. In the fall, a 6-week commissioning and systematic study run is planned at the new beamline. A second full physics run is envisaged in 2013.

### 4.3.1 The 2011 run

D. W. Hertzog, P. Kammel, M. H. Murray, P. Winter, and F. Wauters

A data set of  $5 \times 10^9$  fully-reconstructed negative muon decays was collected in summer, 2011, which is one third of the statistics needed to reach the final precision. The data are being analyzed at several institutions, with a major UW contribution. We are confident that the ongoing analysis will lead to a first physics result from the MuSun experiment.

Upgrades of various detector and data-acquisition systems were crucial to the success of this run. A quantity of 1500 L of isotopically pure deuterium ( $> 99.996\%$ ) was generated and

the active-target TPC was refurbished, including an improved anode-pad plane and Frisch grid as shown in Fig. 4.3.2-1 (see Sec. 4.3.2). Baseline restorers were added to the TPC's amplifier chain and new amplifier-discriminator cards were installed on the electron wire chambers. In addition, a muon spin-rotator magnet was installed around the TPC to control the  $\mu$ SR signal of positive muons, and eliminate it for the possible remnant polarization of the  $\mu^-d$  atoms. A high-purity germanium detector and a NaI detector were installed to explore the option of a muonic X-ray detection system for future runs.

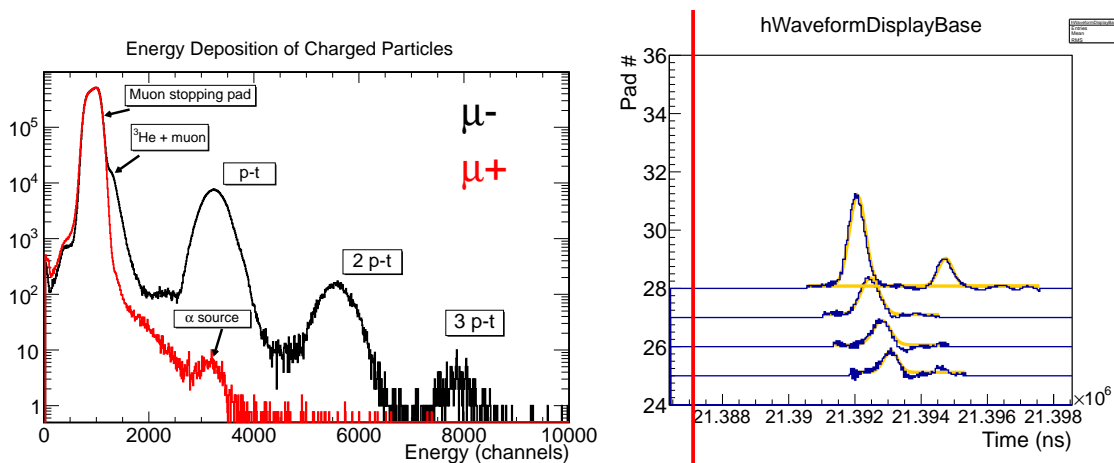


Figure 4.3.1-1. Left: The energy spectra of charged particles in the TPC. The energy deposited on the stopping pad and all neighboring pads is summed, showing the fusion products piled up with the muon stop energy. Right: A typical readout of the TPC's  $6 \times 8$  anode-pad plane, including a Bragg peak on the stopping pads from the stopped muon followed by a  $^3\text{He}$  ion - a product of muon-catalyzed fusion. The orange lines are the fit functions overlaid on the raw signal. The red line is the muon entrance time.

After optimizing the operation of the experiment, all systems functioned reliably during the entire data-taking period. Fig. 4.3.1-1 shows the energy spectra of all charged particles observed in the TPC and the digitized TPC signals of a muon stopping in the middle of the TPC, followed by a  $^3\text{He}$  fusion event, a mono-energetic signal of  $\sim 800$  keV. To improve our understanding of the TPC, a number of detailed systematic studies were performed, such as scanning a wide range of temperatures and densities. In addition, a  $\mu^+$  data set was collected for various systematic checks. The data set of 31.6 TB was written to 2-TB hard drives and copied over the internet to mass tape storage at the TACC Ranch facility in Texas. After the run, the hard drives were shipped to UW and installed in a file storage array, making the data rapidly accessible for the analyzers on local machines and the CENPA Rocks cluster.

### 4.3.2 Hardware development at UW

D. W. Hertzog, P. Kammel, M. H. Murray, P. Winter, and F. Wauters

The MuSun experiment requires stopping muons in a deuterium-gas TPC and detecting the outgoing decay-electron track. Muons entering the stopping target can stop in surrounding materials, which have a capture rate larger than that of deuterium. In order to prevent the

resulting distortion of the lifetime, it is necessary to coat surfaces in very high-Z materials. With this technique, the muons capture before the fit start time, and thus don't affect the measurement. A particularly dangerous surface is the anode plane of the TPC, which is segmented into 48 copper pads (Fig. 4.3.2-1). The plane must be stiff and exhibit little out-gassing in the extremely pure gaseous  $D_2$  environment, so it is constructed of the machinable ceramic MACOR. At the Washington Technology Center on campus, Peterson of the CENPA electronics shop is developing techniques to electroplate Au on the pad plane. For the final version, a thickness of  $20\ \mu\text{m}$  is safer so that the muons do not penetrate to the MACOR or Cu substrate. This is a considerable engineering challenge, requiring that a full board be Au-plated and then machined to a grid of 48 pads. We are consulting with Hank Simons of the CENPA Instrument Shop to find a way to machine this delicate piece.

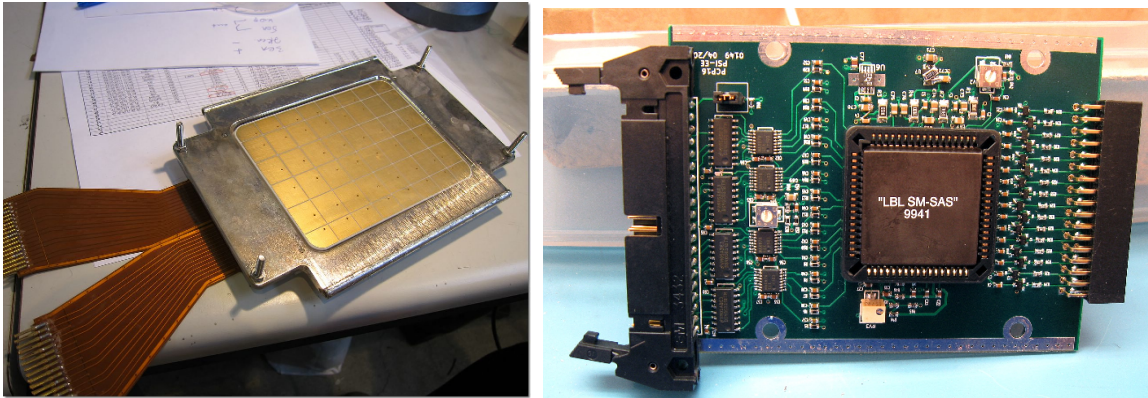


Figure 4.3.2-1. Left: The TPC's pad plane, with 48 Au-plated readout anodes, covered by a stainless-steel Frisch grid. Right: Redesigned amplifier discriminator card to read out 16 of the 2560 channels of the wire chambers.

Decay-electron tracks are detected by two cylindrical 3-plane wire chambers and a barrel hodoscope of scintillator paddles. The 2560 channels of the wire chambers are read out by custom PCB cards each of which contains an amplifier chain and threshold discriminator that digitize the signals from through-going charged particles. These sensitive amplifiers easily pick up RF noise from the electronics near the experiment and from the hall. With the help and effort of Peterson and Van Wechel of the CENPA electronics shop, the cards were redesigned for the summer 2011 run (Fig. 4.3.2-1). The new design introduces a more robust Cu shield (not shown in figure) for the preamplifier inputs, decoupled from the mechanism for mounting to the chamber. During the run, the RF pickup and mounting difficulties of past runs were nearly eliminated, allowing for uninterrupted data acquisition.

In preparation for the coming data runs in 2012 and 2013, we are assembling a test TPC in the Muon Physics Lab in the Physics building. At this test station, we will experiment with different electronic configurations in order to optimize the resolution and stability of the TPC. One goal in particular is to shorten the distance between the charge-integrating preamplifiers and the anode pads. In the current design, the signals from the TPC in the cryo vessel are fed out through the insulation vacuum to an external preamplifier cage. While this is mechanically simpler, the long signal cables contribute a large input capacitance and allow for spurious pickup signals. In order to move the preamplifiers closer to the cryo vessel,

they will have to be redesigned to function at LN<sub>2</sub> temperature. This undertaking has been spearheaded by our colleagues at Regis University and will require the collaboration of the CENPA electronics engineers.

### 4.3.3 Data-analysis progress

D. W. Hertzog, P. Kammel, M. H. Murray, D. J. Prindle, P. Winter, and F. Wauters

The MuSun data-analysis software is a multi-stage, modular C++ program. The first stage performs the most CPU-intensive tasks such as pulse fitting on the TPC digitized waveforms. The raw data are collected into physics objects such as muon and electron tracks, which are stored in the ROOT tree format. Significant gains in performance were achieved by replacing the standard ROOT Minuit fitter by a much faster custom fitter using template waveforms. The second stage of the analysis is a flexible platform for quick passes over the muon entrance centered tree output. In this stage, lifetime histograms are constructed and special systematic studies are performed.

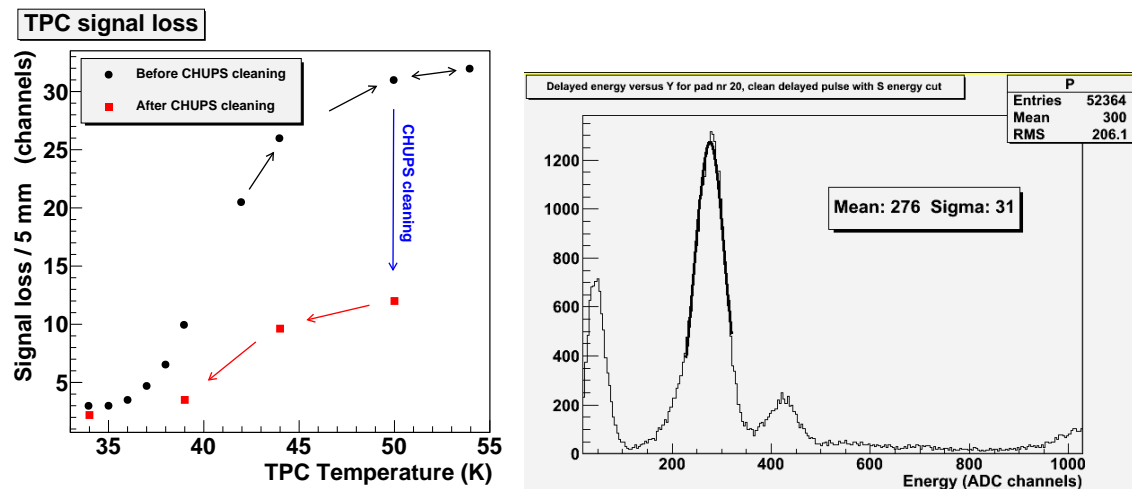


Figure 4.3.3-1. Left: A scan of the the signal loss in the TPC at constant density. The effect decreases when opening the detector to the gas purification system for a few hours. Right: The low energy tail of the <sup>3</sup>He fusion peak is a major background for capture-recoil signal on gas impurities which is a motivation to improve the energy resolution of the TPC.

In order to perform a 1.5% measurement of  $\Lambda_d$ , requiring 10 ppm precision on the negative muon lifetime in deuterium, all systematic effects must be tightly controlled and understood. It is crucial that muon track-finding algorithms be robust against time-dependent effects. For example, any interference between the muon-stop definition in the TPC's fiducial volume and a muon-catalyzed fusion event must be avoided, since coupling to the time-dependent fusion rate skews the exponential time distribution. This means we cannot just rely on the Bragg peak of the muon to define a muon stop. A related effect is the time-dependent interference of the decay electron with the muon track. Different strategies are being explored not only

with real data but also with the MuSun GEANT4-based Monte-Carlo code. In addition, the  $\mu^+$  data set provides a test bed for our algorithms, as it is free of fusion and muonic atomic or molecular effects.

The relatively low  $\Lambda_d$  capture rate and high target density require a D<sub>2</sub> purity level of a few parts-per-billion (ppb), which must be achieved by our continuous gas purification system CHUPS<sup>1</sup>. For the MuCap experiment, the correction on the muon lifetime from remaining gas impurities could be derived from the capture recoil signals, which were well separated from all other signals in the TPC. In the MuSun TPC, this is complicated by the similar magnitude <sup>3</sup>He fusion signals (Fig. 4.3.3-1). During the 2011 run, a small temperature-dependent signal loss as a function of drift time was observed (Fig. 4.3.3-1). We postulate that this effect is due to traces of O<sub>2</sub>, a well-known electronegative contaminant. A careful analysis of the TPC signals in the energy range of the <sup>3</sup>He fusions will test this hypothesis. In addition, the analysis of X-rays in the NaI detector will determine the feasibility of an X-ray detection system to tag impurity events<sup>2</sup>, thus reducing the <sup>3</sup>He background.

Future runs with <sup>1</sup>H<sub>2</sub> and N<sub>2</sub>-doped D<sub>2</sub> will increase our understanding of impurity levels in the cryogenic TPC.

## g-2

### 4.4 Overview of the $g - 2$ experiment: physics, technique and project status

A. García, N. Froemming, D. W. Hertzog, P. Kammel, B. Kiburg, P. Winter, and T. Zhao

The anomalous magnetic moment of the muon,  $a_\mu$ , can be calculated and measured precisely. The “g-2 test” is a comparison between theory and experiment and it represents one of the most sensitive challenges to the completeness of the Standard Model (SM). The SM theory and the Brookhaven E821 measurement<sup>3</sup> have uncertainties of 0.42 ppm and 0.54 ppm, respectively. The difference between experiment and theory (Exp-SM) is  $(287 \pm 80) \times 10^{-11}$ , or a  $3.6 - \sigma$  significance. A  $5 - \sigma$  or greater level of significance is the generally accepted threshold to establish a discovery. To this end, a next-generation  $g - 2$  experiment (E989) has been approved at Fermilab. We are co-leading this effort, which has a precision goal on  $a_\mu$  of 0.14 ppm. It will be achieved by a data sample more than 20 times larger than used at BNL, which can be collected in just over 1 year of running in the new experiment.

The SM error is dominated by quantum loops involving hadrons, specifically the hadronic vacuum polarization (HVP) and the hadronic light-by-light (HLbL) scattering. The relative uncertainties are 0.35 ppm and 0.22 ppm, respectively. The HVP contribution is obtained

<sup>1</sup> V.A. Ganzha *et al.*, NIM A **578**, 485 (2007).

<sup>2</sup>When the muon transfers from a  $\mu d$  atom to a gas impurity such as O<sub>2</sub> or N<sub>2</sub>, a characteristic muonic cascade X-ray is emitted.

<sup>3</sup>Muon G-2 Collaboration: G.W. Bennett *et al.*, Phys. Rev. D **73** 072003, (2006).

from  $e^+e^- \rightarrow \text{hadrons}$  cross sections. The optical theorem, cross-sections, and appropriate dispersion relation are used to accurately determine  $a_\mu(\text{HVP})$ . Low-energy cross-sections are obtained from experiment, and they drive the uncertainty on the HVP contribution. A reduction to  $\sim 0.25$  ppm on the time scale of a new  $g - 2$  experiment is expected based on upcoming experiments. Our group is contributing to these measurements (see Sec. 4.4.2). The HLbL scattering contribution must be determined from low-energy QCD models or from Lattice QCD. We recently co-hosted an INT Workshop<sup>1</sup> on the HLbL scattering contribution. Following the workshop, the theory community is making progress toward their goal of a 0.05-ppm determination of  $a_\mu(\text{HLbL})$ , especially in the lattice-QCD-based efforts.

The E989 experiment will relocate the BNL Storage Ring to Fermilab, and use the accelerator complex to fill the ring 4 times more frequently compared to BNL. Further improvements will lead to a five- to ten-fold increase in the number of stored muons per proton on target and a considerable reduction in beam-related background. An upgraded suite of detectors and associated electronics will be required, as well as improvements in the magnetic-field mapping system. The experimental plans evolved rapidly. An encompassing “Muon Campus” concept has also been established at Fermilab. The campus plan uses a beam-delivery concept different from our previous descriptions. It has the the  $g - 2$  and Mu2e experiments sharing many common accelerator upgrades and physical installations. Since our last report, working teams—*Beam, Ring, Field, Detectors*—have been meeting regularly to advance plans. Except for the Ring-team activities, the UW group is involved directly in all tasks. We have taken a leading role in the detector efforts, which are aimed at the measurement of the muon precession frequency.

The  $g - 2$  work is divided as follows. The beam team is responsible for the entire particle chain that produces muons entering the ring. This sequence includes the booster, the recycler, the target station, the decay FODO lattice, a muon circulation ring (the former antiproton debuncher) and a transport beamline into the experimental hall. The team is now led by Fermilab accelerator physicists with Kammel still playing an active role, especially in the decay lattice design and in aspects of understanding the optimization of beam into the storage ring. The field team will shim the storage-ring field to a high degree of uniformity, and they will measure the field during data-taking using a series of NMR probes. The NMR probes will be read out using a custom data-acquisition system. García is involved in the field team activities. The ring team will disassemble the storage ring at BNL, arrange for its transport to Fermilab, and rebuild it in a new building. Ground-breaking is tentatively scheduled for late 2012. The Detector team encompasses the tasks related to the measurement of the precession frequency: detectors, electronics, DAQ, analysis and simulations.

Our group has focused on two technical efforts: simulations and detector development. The simulation effort is based on the collaboration protocol g2MIGTrace. Kiburg and graduate student Froemming have both contributed significantly to this project. It is a complete GEANT-based dynamic muon storage simulator with proper spin tracking and decays. Simulation is being used to understand two-pulse pileup, one of the lead systematic error categories. Pileup is expected to be exacerbated at the higher data rates at Fermilab. All

---

<sup>1</sup><http://www.int.washington.edu/PROGRAMS/11-47w/>

detector responses will be digitized and waveforms will be stored for offline interpretation. We are developing fast calorimeters with custom electronics to minimize pulse-occupancy time. The readout devices—ultra-fast PMTs or “silicon photomultipliers”—are measured in our lab, where we can precisely produce two-pulse sequences using a uv laser. The output is then compared to our two-pulse-pileup simulation engine. The simulation engine takes measured pulse shapes as input, and uses them to produce controlled data-like digitization sequences. A pulse-finder program is then used to fit the sequences. The fits are used to determine the pulse numbers, times and energies. We describe a small fraction of the work in detail in a separate section (see Sec. 4.4.1). We also describe the recent efforts we led at the Fermilab Test Beam Facility (see Sec. 4.4.2).

#### 4.4.1 Detector-development laboratory and test-beam run for $g - 2$

D. W. Hertzog, P. Kammel, B. Kiburg, R. LeFree, K. Wall, P. Winter, and T. Zhao

Our detector-development laboratory has evolved significantly in the past year. Tools to test and calibrate electromagnetic calorimeters, the MuSun gondola hodoscope, and various photo-sensitive readout devices are working. Our fast multi-wire proportional chambers (used in the recent  $g - 2$  test-beam run, see below) were prepared and tested. A new area has just been set up for MuSun TPC work aimed at pad-plane electronics and pad-plane optimization. The lab provides an excellent opportunity for students to obtain hands-on hardware experience. Physics major LeFree carried out many of the basic lab installation requirements and detector measurements. She has been assisted recently by undergraduate student Wall. Supervision and execution of the detailed program is carried out by postdocs Kiburg and Winter.

The  $g - 2$ -specific tests involve evaluating the performance of fast photomultipliers (PMTs) and large-array silicon photomultipliers (SiPMs). Each device is a candidate to be coupled with either our homemade W/SciFi calorimeter or PbF2 or PbWO4 crystals, which were purchased from the Shanghai Siccas High Technology Corporation. The in-house tests are designed to prepare detectors, measure and calibrate light yield, and perform two-pulse “pileup” tests under controlled conditions.

The  $g - 2$  calorimeter must be dense, non-magnetic and segmented, with good resolution and a very short pulse shape. These characteristics are satisfied in different degrees by all three tested options. Twenty-four arrays of  $5 \times 7$  segments (height by width) will eventually be built. The segmentation and orientation imply a readout in a region having limited space. Lightguides that couple the detectors to remote PMTs are difficult to realize. We are thus driven to consider the new SiPM technology. These devices are non-magnetic and immune to high fields and can be placed directly on the rear ends of the chosen calorimeter option. The focus of our work has been on the direct comparison between a known technology (PMTs) that is difficult to implement versus a new technology (SiPMs), which appear to be straightforward to install.

Some of the tools now built or acquired include:

- A nitrogen laser system, which produces 600-ps, 337-nm light bursts. Several splitter boxes are used with a reference PMT that monitors the light level, shot by shot.
- An optics setup that allows for two pulses, separated by various fixed-length quartz cables to be directed at different detectors. An attenuator wheel is used to provide quantized reductions in the light level. This system is also used to calibrate the photo-electrons per channel or per pulse height as a function of gain.
- ORCA data-acquisition software coupled to CAMAC. This flexible system has been configured to support many of our measurement efforts.
- Several fast digital oscilloscopes, various power and bias supplies, custom LED drivers, and a variety of standard electronics modules, light-tight boxes, and a light-pen scanner.

At this time, our leading candidate detector system for  $g - 2$  is a PbF<sub>2</sub> crystal array read out by 16-channel SiPMs from Hamamatsu. PbF<sub>2</sub> is a pure Cherenkov medium, which guarantees the shortest light pulse compared to the SciFi or PbWO<sub>4</sub>. It has excellent resolution and it is very dense. SiPM technology has been evolving rapidly since we first began to test these devices and the cost has gone down significantly. The device we are now using has an active area of  $12 \times 12 \text{ mm}^2$ , in 16 individual  $3 \times 3\text{-mm}^2$  “channels.” It has more than 56,000 individual  $50 - \mu\text{m}^2$  pixels, each of which responds in Geiger mode to an incoming photon. The summed hits (activated pixels) on each channel provide analog signals that must be amplified, summed and inverted and then transported along standard  $50\text{-}\Omega$  coax signal cable. Our CENPA engineers have produced numerous custom boards for various devices of different sizes to provide the bias voltage and to sum and invert the channels. It is a non-trivial development as the boards must be compact, low in power consumption, and non-magnetic. Their main efforts are aimed at designing circuits having the shortest possible recovery time for the hit pixels, ultimately reaching the intrinsic device-limited RC time constant. They have achieved this for smaller SiPMs and they are in the process of optimizing the components, power consumption and onboard circuitry to preserve pulse shape for the full array of 16 channels. To our knowledge, this unique aspect of SiPM development has not yet received significant attention by others.

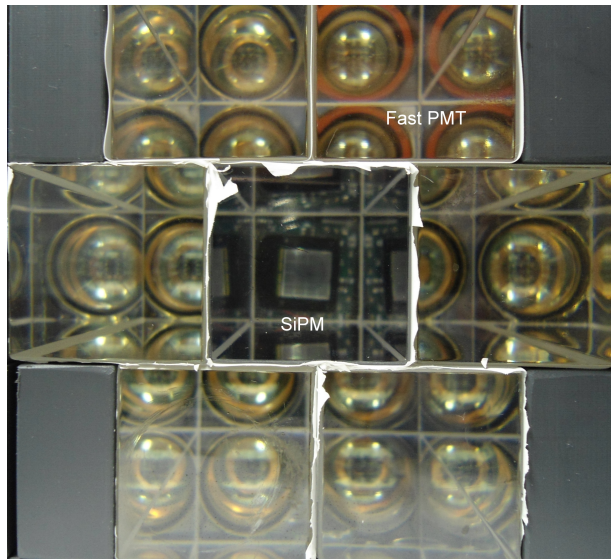


Figure 4.4.1-1. Photo of the front face of our  $2 \times 3 \times 2$  array of PbF<sub>2</sub> crystals. Each has a cross section area of  $3 \times 3 \text{ cm}^2$  and a length of 14 cm. The view through the crystals shows the centered SiPM readout and multiple reflections of the PMTs used on the outer crystals.

A main focus of this year's work has been to prepare an array of crystals (see Fig. 4.4.1-1) for testing at the Fermilab Test Beam Facility (FTBF). We recently completed a week-long run where we measured the response to electrons from 1 to 8 GeV for a  $2 \times 3 \times 2$  array of PbF2 crystals, a PbWO4 crystal, a large W/SciFi array, and a standard Fermilab large Pb-glass detector (for reference). We used a variety of wrapping techniques and couplings from "crystal" to readout device. The fast PMT and the SiPM were compared directly on the same crystal. The waveforms for all events were recorded using both 12-bit 500-MHz and 8-bit 1-GHz digitizers. Incoming electrons were triggered by several scintillators and a gas Cherenkov counter and their impact positions were recorded by our MWPC. Fig. 4.4.1-1 shows the open front face of our 7-crystal PbF2 array. Visible in the center is the 16-channel SiPM with one of the CENPA-designed electronic summing circuits. The outer crystals are read out using conventional photomultipliers (PMTs). The top right crystal has a very fast, 8-stage Hamamatsu R9800 PMT used to measure the absolute pulse shape, which varied by wrapping technique. The analysis of these data has just begun.

#### 4.4.2 Current status of cross section measurements via ISR at Belle

J.D. Crnkovic, D.W. Hertzog, and J. Kaspar

The most recent measurement of the muon anomalous magnetic moment ( $a_\mu$ ) suggests the possibility of new physics beyond the Standard Model. The largest source of uncertainty in the Standard-Model prediction comes from the leading-order hadronic vacuum polarization (HVP) component. The HVP uncertainty is primarily due to the inability to calculate the contributions below 3 GeV in perturbative QCD. The low-energy contributions are instead derived from experimentally measured exclusive cross sections of electron-positron annihilation to hadrons and some contributions can be calculated from  $\tau$ -spectral functions<sup>1</sup>. Historically there have been significant differences between the predicted  $a_\mu$  from the  $e^+e^-$  cross sections vs. the  $\tau$  data<sup>2</sup>. Theoretical work on this discrepancy continues<sup>3</sup>.

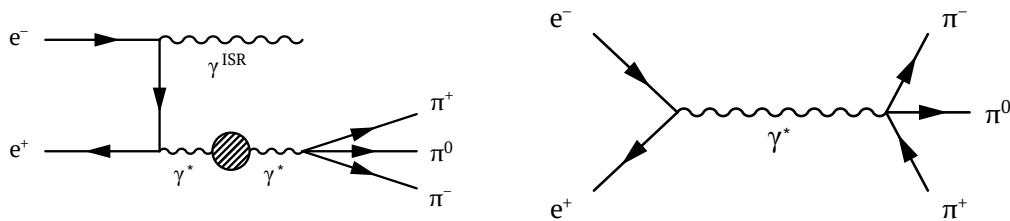


Figure 4.4.2-1. Leading-order Feynman diagram for  $e^+e^- \rightarrow \pi^+\pi^-\pi^0$  process as measured by the initial-state radiation method. The tree-level diagram of the same process, given on the right, is used in the dispersion relation to derive hadronic vacuum polarization.

The direct method of obtaining these cross sections is to vary the center-of-mass energy of the initial electron-positron system. Fixed-energy colliders, such as  $B$ -factories, can alternatively use an initial-state radiation (ISR) photon to lower the effective invariant mass of the hadron system. Fig. 4.4.2-1 shows the leading-order ISR Feynman diagram.

<sup>1</sup> R. Alemany, M. Davier and A. Hocker, Eur. Phys. J. C **2**, 123 (1998) [arXiv:hep-ph/9703220].

<sup>2</sup> F. Jegerlehner, Acta Phys. Polon. B **38**, 3021 (2007) [arXiv:hep-ph/0703125].

<sup>3</sup> F. Jegerlehner and R. Szafron, arXiv:1101.2872 [hep-ph].

The  $\sigma(e^+e^- \rightarrow \pi^+\pi^-\pi^0)$  and  $\sigma(e^+e^- \rightarrow \pi^+\pi^-\eta)$  are two such HVP contributions to the calculation of  $a_\mu$ . The  $\pi^+\pi^-\pi^0$  channel provides the second largest contribution to  $a_\mu$ <sup>1</sup>, and the  $\pi^+\pi^-\eta$  channel has a corresponding  $\tau$ -spectral function for comparison. Both channels are relevant to the precision goals of the new Fermilab E989 experiment<sup>2</sup>. The aim of our current research is to precisely measure both of these cross sections using the ISR method on Belle data obtained at the KEK-B factory in Tsukuba, Japan.

We ported the Belle analysis framework to the CENPA computing cluster. This allows for the local processing of Belle data, as well as the production and processing of Belle Monte Carlo. This work forms the thesis for Crnkovic (University of Illinois Ph.D. student).

The Belle analysis has recently completed and:

- All the Belle data were processed.
- Standard Belle kinematic cuts were carefully fine-tuned, and new cuts were added to significantly improve the signal-to-noise ratio.
- Multiple fitters were developed and tested to separate signal from background including Feldman-Cousins formalism, a phenomenological double-Gaussian fitter, and MC-derived signal resonance shapes.
- Particle-identification corrections to cross sections and relevant systematic uncertainties were calculated.
- In addition to accurate geometry and detailed physics, the Belle MC now includes a proper trigger simulation.
- Several mass-unfolding methods ranging from a simple matrix inversion up to Bayesian techniques were tested and their performances are being evaluated.
- The PHOKHARA<sup>3</sup> event generator, simulating ISR processes to next-to-leading order accuracy, was added to the Belle MC and used to calculate detector efficiency.
- The EvtGen decay generator is being ported to Belle MC to better understand final-state radiation in these processes and convert the ISR cross section to a tree-level one; see Fig. 4.4.2-1.
- A Belle collaboration note was written.

Cross-sections for  $e^+e^- \rightarrow \pi^+\pi^-\pi^0$  and  $e^+e^- \rightarrow \pi^+\pi^-\eta$  processes have been calculated. Studies of systematic uncertainties are in progress. The goal of this analysis is to gain a better local understanding of initial-state radiation physics and its effect on cross-section measurements and hadron vacuum polarization.

---

<sup>1</sup> M. Davier, A. Hoecker, B. Malaescu, Z. Zhang, Eur. Phys. J. C **71** 1515 (2011).

<sup>2</sup> [http://gm2.fnal.gov/public\\_docs/proposals/Proposal-APR5-Final.pdf](http://gm2.fnal.gov/public_docs/proposals/Proposal-APR5-Final.pdf).

<sup>3</sup> <http://ific.uv.es/~rodrigo/phokhara/>.

## 5 Axion searches

### ADMX (Axion Dark Matter eXperiment)<sup>1</sup>

#### 5.1 ADMX axion search

C. Boutan, M. Hotz, D. Lyapustin, L. J Rosenberg, G. Rybka, A. Wagner, and D.I. Will

The Axion Dark Matter eXperiment (ADMX) is a large-scale RF-cavity search for galactic dark-matter axions. This experiment has been in operation since the mid-1990s, and was moved to CENPA in 2010. It is presently being upgraded to have sufficient sensitivity to either detect or rule out the QCD-axion hypothesis at high confidence. We plan to begin commissioning the newly upgraded ADMX in late 2012 and begin data taking shortly thereafter.

The axion was postulated three decades ago to explain why QCD conserves the discrete symmetries  $P$  (parity) and  $CP$  (charge conjugation times parity). QCD's predictions depend upon a parameter  $\theta$ . When  $\theta$  differs from zero, QCD violates  $P$  and  $CP$ . Since the strong interactions appear to be  $P$ - and  $CP$ -symmetric in the laboratory,  $\theta$  must be very small. The upper limit on the neutron electric-dipole moment requires  $|\theta| < 10^{-10}$ . However, in the Standard Model,  $P$ - and  $CP$ -violation by the weak interactions feeds into the strong interactions so that the expected value of  $\theta$  is of order unity. The inability of the Standard Model to account for  $P$ - and  $CP$ -conservation by the strong interactions is called the "strong  $CP$  problem". Peccei and Quinn proposed a solution to this problem in which the Standard Model is modified so that  $\theta$  becomes a dynamical field and relaxes to zero. The theory's underlying broken continuous symmetry results in the existence of a new particle called the axion. The axion is the quantum of oscillation of the  $\theta$  field and has zero spin, zero electric charge, and negative intrinsic parity. So, like the neutral pion, the axion can decay into two photons.

Despite, however, the prodigious predicted local density of dark-matter axions (in the neighborhood of  $10^{14}/\text{cc}$ ), the expected electromagnetic signal would be extraordinarily weak, around  $10^{-23}$  W in the ADMX apparatus. Our present ADMX Collaboration (with original core institutions Washington, LLNL, Florida, NRAO and Berkeley) constructed and operated a large-scale dark-matter axion experiment that, for the first time, reached sensitivity to plausible dark-matter axions. This experiment consists of a large microwave cavity immersed in a static magnetic field. Nearby galactic-halo axions scatter from the static field and convert into microwave photons within the cavity.

The ADMX detection apparatus is essentially an extraordinarily low-noise radio receiver with a RF cavity forming a tuned tank circuit. A short electric-field probe couples power

---

<sup>1</sup>ADMX is supported by the DOE Office of High-Energy Physics and makes use of CENPA resources by recharge to the cost center.

from the cavity into a cryogenic amplifier which is cooled to near the cavity temperature, around 2 K.

The last operation of the ADMX experiment, fitted with superconducting quantum interference device (SQUID) amplifiers, completed a scan of the  $1.9 - 3.5 \mu\text{eV}$  axion mass range and published the results for conservative estimates of dark matter density. With further analysis we have since published a search for axions under more interesting models of how dark matter may be distributed in our galaxy<sup>1</sup>.

The motivation for lowering the system noise temperature is clear: (i) for a given axion-photon coupling the scan rate grows inversely as the square of the system temperature and (ii) for a given scan rate the power sensitivity increases as the system temperature drops. In ADMX the system noise temperature is essentially the noise temperature of the amplifier plus the cavity physical temperature. We developed SQUID amplifiers in the 100-1000 MHz range specifically for ADMX and this development allowed more than an order-of-magnitude reduction in system noise temperature.



Figure 5.1-1. Left: Installing the bucking coil, which cancels the magnetic field at the location of the SQUID, in the new experimental insert. Right: The new design for the ADMX experimental insert shown in position within the superconducting main magnet.

ADMX is currently being retrofit for lower-temperature operation. We intend to use a pumped  $^3\text{He}$  system to reach a temperature of 300 mK, and later install a dilution refrigerator capable of reaching 100 mK. The cryogenics of these temperatures are considerably more technically challenging than those of the last operating point and require a complete redesign of the experimental insert. Construction of this new insert began in winter, 2011, and we expect to enter a commissioning phase later this year. To support the cryogenics of the ADMX experiment, a helium liquefaction system will be installed at the far end of the accelerator tunnel this fall.

<sup>1</sup>J. Hoskins *et al.*, Phys. Rev. D **84**, 121302(R) (2011).

## Axion torsion balance experiment

### 5.2 Investigation of upgrades to the axion-search torsion balance

E. G. Adelberger, F. Fleischer, B. R. Heckel, S. A. Hoedl\*, C. D. Hoyle†, D. Shook†, and H. E. Swanson

In the previous annual report<sup>1</sup> we described an upgrade to the torsion-balance experiment searching for axion-like particles. As discussed in the same report, the error of our first published result<sup>2</sup> from this project was completely dominated by the problem of degaussing the magnet to a well-defined and reproducible initial state.

We have continued our investigation of a laminated magnet core design made from sheets of perfection-annealed CO-NETIC AA<sup>3</sup>. This was done via experimental studies of the prototype made previously and by means of finite element simulations. The software package COMSOL Multiphysics<sup>4</sup> was used for the simulations to explore the effects of geometrical imperfections in assembling the magnet core and in aligning the two halves of the magnet and the pole pieces with respect to each other. As a check of the results of the simulations we also compared magnetic-field calculations for the new core with corresponding measurements achieving good agreement within the uncertainties of the exact geometry.

In addition we have decided to explore a new pendulum geometry to reduce the dependence of the equilibrium position of the pendulum on small alignment errors of the magnet halves. Also in this case, we have used COMSOL Multiphysics to study changes to the current design. We have decided to forgo a geometrical cancellation effect which reduces the magnetic force due to the diamagnetism of the silicon. Instead we will aim for a pendulum shape which is less sensitive to imperfections in the magnet geometry.

Together these changes seem to represent a viable upgrade path towards an experiment with greater sensitivity and therefore more stringent limits on a macroscopic, parity- and time-reversal-violating force mediated by axion-like particles.

---

\*Civatech Oncology, Inc., Research Triangle Park, NC.

†Humboldt State University, Arcata, CA.

<sup>1</sup>CENPA Annual Report, University of Washington (2011) p. 75.

<sup>2</sup>S.A. Hoedl, F. Fleischer, E.G. Adelberger, and B.R. Heckel, Phys. Rev. Lett. **106**, 041801 (2011).

<sup>3</sup><http://www.magnetic-shield.com/products/conetic.html>

<sup>4</sup><http://www.comsol.com>

## 6 Relativistic Heavy Ions

### 6.1 UW URHI program overview

T. A. Trainor

The UW URHI (ultra-relativistic heavy ion) program, also referred to as the Event Structure or Estruct program (in close cooperation with the URHI group at UT Austin) has established a detailed phenomenological description of RHIC collisions using data from the solenoidal tracker at RHIC (STAR) detector. This description strongly contradicts popular claims for creation of a strongly-coupled, flowing, dense partonic medium or “perfect liquid” with novel properties, including opacity to most jets and very small viscosity. The principal contradictions include identification of *increased* jet structure in more-central Au-Au collisions and isolation of a *nonjet azimuth quadrupole* that might be interpreted as “elliptic flow” but whose phenomenology strongly contradicts hydro-theory expectations in several respects. It is possible that jet and quadrupole phenomena represent the extremes of QCD as a field theory: Compton scattering of partons at one limit and continuum multipole radiation (azimuth quadrupole) at the other. We have established that the quadrupole is remarkably insensitive to the collision context except for the geometry evolution of intersecting spheres, independent of their size.

Because of the major community investment in “perfect liquid” claims there has been a strong negative response to Estruct results. The same-side 2D peak identified as jet structure (jet cone) in 2D angular correlations has been reinterpreted in terms of “higher harmonic flows” (e.g., “triangular flow”) or “glasma flux tubes” coupled to radial flow, or as the result of fluctuations of the initial-state A-A collision geometry coupled to the flowing medium. The common strategy has been to minimize apparent jet structure in favor of flow interpretations.

In response we have adopted a multifaceted program to address several issues: (a) the uniqueness of the Estruct model of 2D angular correlations, (b) the direct relation between pQCD theory and jet manifestations in spectra and correlations, (c) the uniqueness of the nonjet quadrupole component of angular correlations isolated from jet structure, (d) the lack of correspondence between jet and nonjet-quadrupole evolution with A-A centrality, (e) the inconsistencies between nonjet quadrupole phenomenology and hydro theory predictions, (f) falsification of glasma flux tube conjectures by direct comparisons with correlation data, (g) identification of claimed “higher harmonic flows” as manifestations of 1D Fourier components of the same-side 2D jet peak.

Given recent challenges to Estruct model fits to data we have formulated a detailed description of the statistical basis for the standard 2D fit model, including the concept of a *necessary and sufficient* data model and the *principle of parsimony* (Ockham’s razor) in which the model with fewest parameters must be preferred. We have provided detailed mathematical correspondence between the Estruct standard model and proposed alternatives, especially elaboration of the Estruct model by addition of a sextupole  $\cos(3\phi_\Delta)$  term. We have demonstrated that the added sextupole component (interpreted as “triangular flow”) is not a *necessary* model element, and its fit values are actually *systematically insignificant*.

A quantitative equivalence has been established between recently-claimed higher harmonic flows and the Fourier series components of the same-side (SS) 2D jet peak projected onto the 1D azimuth<sup>1</sup>. It has been shown that the SS 2D peak volume is predicted by pQCD, so the peak is not a hydro manifestation. It is also shown that the SS 2D peak centrality trend is unrelated to that of the nonjet quadrupole, which might be interpreted to represent elliptic flow if that mechanism were relevant. Nonjet quadrupole systematics are in turn incompatible with hydro interpretations. Quadrupole source-boost systematics are at odds with hydro predictions, and the energy dependence is remarkably similar to that for jet structure. To validate such interpretations we have made a careful study of quadrupole-data systematic uncertainties. We find that flow interpretations are generally falsified by spectrum and correlation data.

We have submitted a long paper on minijet correlations in Au-Au collisions<sup>2</sup> that describes the discovery of a *sharp transition* in jet characteristics occurring at a fixed centrality point (as measured by mean participant path length  $\nu$ ) independent of energy or system size (e.g., the same  $\nu \approx 3$  for Au-Au and Cu-Cu). The sharp transition and strong increase in jet structure for more-central Au-Au collision are interpreted as anomalous centrality evolution inconsistent with the formation of a dense, thermalized partonic medium opaque to jets.

We have established a quantitative relation between pQCD parton-fragment yield predictions and measured spectrum and correlation structure nominally identified with jets<sup>3</sup> to buttress the (mini)jet interpretation and confirm a quantitative (Borghini-Wiedemann) description of modified parton fragmentation to jets in more-central Au-Au collisions.

We have employed the measured properties of minijet correlations, both centrality trends and transverse-momentum ( $p_t$ ) structure to falsify theoretical claims that the nominal same-side jet structure actually results from glasma flux tubes combined with radial flow<sup>4,5,6</sup>.

We have explained the “same-side ridge” observed in correlations from p-p collisions at 7 TeV (with certain multiplicity and  $p_t$  constraints) in terms of the nonjet azimuth quadrupole appearing in p-p collisions, discounting claims of new physics in p-p collisions at LHC energies related to claimed QGP in heavy-ion collisions at the RHIC.

As a follow-up we have measured the charge-multiplicity dependence of the nonjet quadrupole in 200-GeV p-p collisions and find a simple trend that may provide a sought-after centrality measure for p-p collisions.

More-recent progress on those several topics is presented below.

---

<sup>1</sup>T. A. Trainor, arXiv:1109.2540.

<sup>2</sup>G. Agakishiev *et al.* (STAR Collaboration). arXiv:1109.4380.

<sup>3</sup>T. A. Trainor and D. T. Kettler, Phys. Rev. C **83**, 034903 (2011).

<sup>4</sup>T. A. Trainor and R. L. Ray, Phys. Rev. C **84**, 034906 (2011).

<sup>5</sup>T. A. Trainor and D. T. Kettler, Phys. Rev. C **84**, 024910 (2011).

<sup>6</sup>T. A. Trainor, arXiv:1012.2373.

## 6.2 Au-Au azimuth quadrupole source-boost systematics on $(b, \sqrt{s_{NN}})$

D. T. Kettler and T. A. Trainor

The nonjet azimuth quadrupole conventionally denoted by  $v_2$  and interpreted in terms of “elliptic flow,” a conjectured hydrodynamic phenomenon, can be associated with a particle source boost inferred from  $v_2(p_t)$  data. The basis for the inference is assigning by hypothesis a quadrupole source boost including monopole (radial flow) and quadrupole components  $\Delta y_{t0} + \Delta y_{t2} \cos[2(\phi - \Psi_r)]$ , where  $\Psi_r$  denotes the collision reaction-plane angle. The associated particle spectrum  $\rho_2(y_t, \phi, b)$  is described according to the Cooper-Frye prescription for thermal radiation from a moving source. A Taylor expansion applied to the definition of  $v_2(y_t, b)$  gives  $\rho_0(y_t, b)v_2(y_t, b) \approx (\Delta y_{t2}/2T_2)p_t(\text{boost})\rho_2(y_t, b)$ , where  $\rho_2(y_t, b)$  is the quadrupole spectrum. By plotting measured quantities in the form  $v_2(p_t, b)/p_t(\text{lab}) \propto [p_t(\text{boost})/p_t(\text{lab})] \rho_2(y_t, b)/\rho_0(y_t, b)$  vs transverse rapidity  $y_t$  we can infer the source boost  $\Delta y_{t0}$  from the common zero intercept. The ratio in square brackets is purely kinematics.

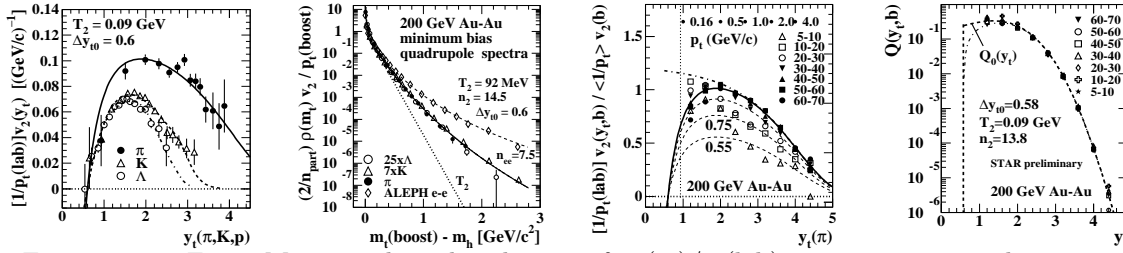


Figure 6.2-1. First: Minimum-bias distribution of  $v_2(p_t)/p_t(\text{lab})$  vs transverse rapidity  $y_t$  for 3 hadron species. Second: Those data plotted as quadrupole spectra on  $m_t$  in the boost frame. Third: Centrality dependence of  $p_t$ -differential nonjet  $v_2\{2D\}(p_t)$ . Fourth: Universal quadrupole spectrum  $Q_0(p_t)$  that describes all centralities from 200-GeV Au-Au collisions.

Fig. 6.2-1 (first) shows published  $v_2(p_t, b)$  data (points) divided by  $p_t$  in the lab frame. The data are *minimum-bias* – averaged over all Au-Au centralities. The curves represent a universal parametrization. All data trends intercept zero at the inferred source boost  $\Delta y_{t0} = 0.6$ . Fig. 6.2-1 (second) shows the same data transformed from the lab frame to the boost frame and plotted as quadrupole spectra vs transverse mass  $m_t$ . In that format the data for three hadron species coincide when normalized by their thermal-model abundances (relative to pions, factors noted in the panel), as expected for a common boosted source.

The question then arises: what is the centrality dependence of the quadrupole source boost? Does it increase with Au-Au centrality due to higher densities and increased pressure gradients as expected for flows? Fig. 6.2-1 (third) shows quadrupole data vs Au-Au centrality inferred with the Estruct standard 2D-fit model. The data are unit-normalized and show that over a broad centrality range the source boost is constant. For the most-central collisions the overall magnitude drops below the trend for more-peripheral collisions indicating “quenching” of the nonjet quadrupole. Fig. 6.2-1 (fourth) shows the same data multiplied by the corresponding single-particle spectra  $\rho_0(y_t, b)$  to reveal the unit-normal quadrupole spectra  $Q(y_t, b)$ . All spectra are described by a single universal form  $Q_0(y_t)$  (bold dashed curve). The source boost is constant in all cases, and the combination  $\rho_0(y_t, b)v_2(y_t, b, \sqrt{s_{NN}})$  is fully factorized.

### 6.3 Universal parametrization of $v_2\{2D\}(p_t, b, \sqrt{s_{NN}})$

D. T. Kettler and T. A. Trainor

Systematic variation of the  $p_t$ -differential azimuth quadrupole conventionally measured by  $v_2(p_t, b)$  plays a key role in tests of hydro theory and in separate analyses related to jet studies. In the latter case systematic parametrizations of  $v_2(p_t, b)$  are used to define a combinatoric background subtracted from sibling-pair distributions to infer jet angular correlations. If the  $v_2$  data are in error substantial systematic biases in apparent jet structure may result.

Using Estruct 2D-model fits to angular correlations we have established a simple universal trend inferred from  $v_2\{2D\}(p_t, b)$  data that provides an accurate data parametrization free of jet-related biases (“nonflow”). Fig. 6.3-1 (left) shows for six centralities (dotted curves)

$$v_2\{2D\}(p_t, b) = \langle 1/p_t \rangle p_t v_2\{2D\}(b) \rho_2(p_t, b) / \rho_0(p_t, b) \quad (1)$$

in the form  $v_2\{2D\}(p_t, b) = 2(\text{GeV}/c)^{-1} p_t v_2\{2D\}(b) \exp[-p_t/(4 \text{ GeV}/c)]$ , where  $v_2\{2D\}(b)$  represents a simple parametrization of previously-measured  $p_t$ -integral quadrupole data that describes  $\{2D\}$  data down to p-p collisions. The solid curves are obtained from the expression above by suppressing the quadrupole amplitudes for the most-central cases.

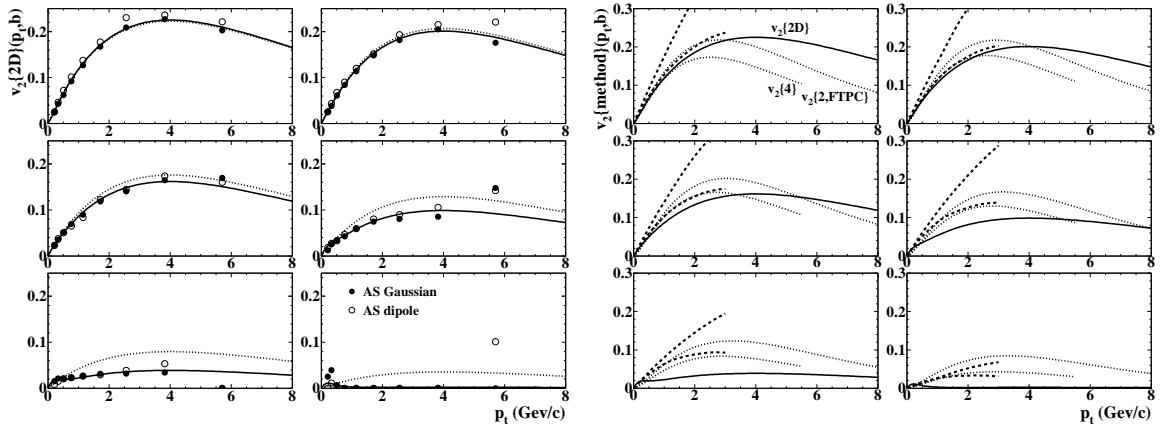


Figure 6.3-1. Left: Measured nonjet quadrupole data  $v_2\{2D\}$  (points) from this analysis vs transverse momentum  $p_t$  for six increasing 200-GeV Au-Au centralities including 0-5% central (lower right) – curves describe a universal  $v_2$  parametrization (see text). Right: Comparisons between the universal parametrization from this analysis (solid curves), conventional  $v_2$  parametrizations (dotted curves) and viscous hydro predictions (dashed curves).

Fig. 6.3-1 (right) shows comparisons between the solid curves in the left panels and an alternative parametrization based on published conventional  $v_2(p_t)$  data (dotted curves). The upper dotted curves represent published  $v_2\{2, \text{FTPC}\}$ , the lower curves  $v_2\{4\}$  (two- and four-particle cumulant methods). It is apparent that large discrepancies exist between the two systems. The differences have been identified as contributions from the quadrupole component of the same-side 2D jet peak. When that conventional parametrization is used to isolate apparent jet azimuth correlations large errors may result, especially underestimation of jet amplitudes and away-side distortions interpreted by some to indicate formation of “Mach cones.” Comparisons with hydro theory (dashed curves, two viscosities) are also misleading.

## 6.4 Systematic uncertainties for $v_2\{2D\}(p_t, b, \sqrt{s_{NN}})$ measurements in Au-Au

D. T. Kettler and T. A. Trainor

Estruct model fits to 2D angular correlations have provided major insights regarding evolution of jet-related structure and the nonjet azimuth quadrupole, including a factorized universal description of the latter. It is essential to establish the accuracy of those results by estimating systematic uncertainties, emphasizing in this case the nonjet azimuth quadrupole. Assessment of systematic uncertainties is a complex subject. Here we consider specifically 2D model-fit uncertainties and uncertainties in inferences of quadrupole source boosts.

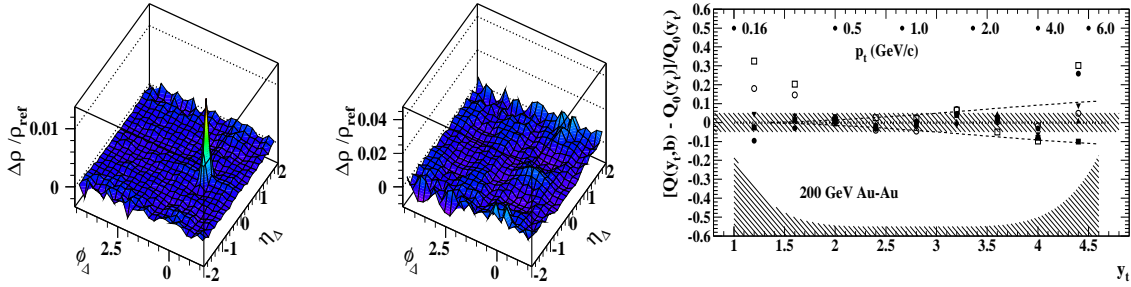


Figure 6.4-1. Left: Fit residuals for 40-50% central Au-Au collisions with  $p_t \approx 0.5$  GeV/c (first) and 3 GeV/c (second). Right: Relative deviations of measured quadrupole spectra  $Q(y_t, b)$  from a universal function  $Q_0(y_t)$  independent of Au-Au centrality (impact parameter  $b$ ). The dashed curves indicate relative changes in quadrupole source boost  $\Delta y_{t0}$  by  $\pm 2\%$ .

Fig. 6.4-1 (left panels) shows representative fit residuals from 40-50% central 200-GeV Au-Au collisions for  $p_t = 0.5$  GeV/c (first) and 3 GeV/c (second). The  $p_t$ -differential fit model does not include a term for Bose-Einstein correlations and conversion electrons. That structure then survives as a narrow peak at the origin in the first panel. At larger  $p_t$  the BEC component is negligible, but the same-side 2D peak acquires a non-Gaussian shape on  $\eta_\Delta$  just visible in the second panel. Systematic studies reveal that the nonjet azimuth quadrupole represented by  $v_2\{2D\}$  or  $A_Q\{2D\}$  is insensitive to the details of the SS 2D peak model *as long as such a model is employed*. The fit residuals are otherwise consistent with statistical uncertainties.

Fig. 6.4-1 (right panel) considers uncertainties in the surprising conclusion that the nonjet azimuth quadrupole mean source boost  $\Delta y_{t0}$  is independent of Au-Au centrality, dramatically contradicting expectations from hydrodynamic scenarios. The plotted points represent the relative difference  $[Q(y_t, b) - Q_0(y_t)]/Q_0(y_t)$  for seven Au-Au centrality bins, where the  $Q(y_t, b)$  are unit-normal quadrupole spectra inferred from  $v_2\{2D\}(p_t, b)$  data and  $Q_0(y_t)$  is a universal Lévy distribution boosted by  $\Delta y_{t0} = 0.6$ . The upper hatched band represents  $\pm 5\%$  point-to-point relative deviations. The dotted curves represent shifts in the source boost by  $\pm 2\%$  of  $\Delta y_{t0}$ . The lower hatched band represents 2D fit uncertainties. This plot establishes small upper limits on overall systematic uncertainties in both the inferred source boost and the *shape* of  $y_t$  of the universal parametrization of  $v_2\{2D\}(y_t, b, \sqrt{s_{NN}})$ .

## 6.5 Distinguishing nonjet- and jet-related azimuth quadrupole contributions

D. T. Kettler and T. A. Trainor

Published  $v_2$  data conventionally interpreted to represent “elliptic flow” as a hydrodynamic phenomenon may include substantial biases extending to 100% of the published data values. Such bias is conventionally referred to as “nonflow.” It can be demonstrated from 2D angular correlations that the dominant source of “nonflow” bias is the SS 2D peak corresponding to jets. Estruct model fits to 2D angular correlations accurately distinguish between the SS 2D peak contribution  $v_2\{SS\}$  and the *nonjet* contribution  $v_2\{2D\}$  that might be associated with elliptic flow if such flow played a significant role in nuclear collisions.

Fig. 6.5-1 (first) shows published  $v_2\{EP\}$  (event plane) data for two energies (points) compared to a parametrization of  $v_2\{2D\}$  data (solid curves) in the form of per-particle measure  $A_Q = \rho_0(b)v_2^2$ , with  $\rho_0(b)$  the single-particle angular density. The difference between EP and 2D data is just the quadrupole component of the SS 2D jet peak denoted by  $A_Q\{SS\}$ .

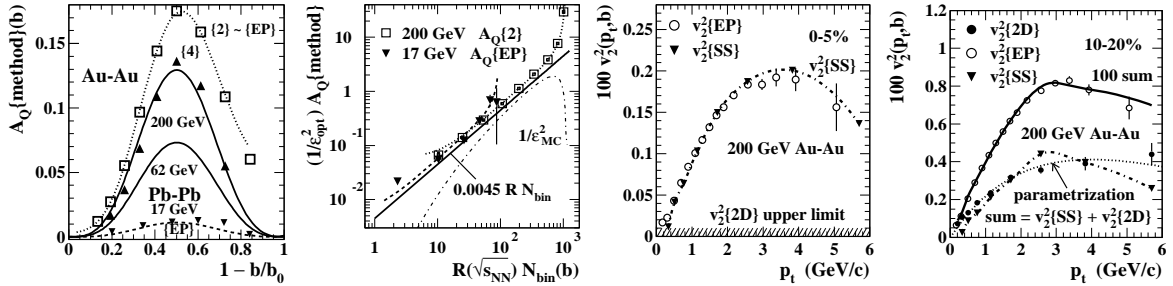


Figure 6.5-1. First: Published  $v_2(b)\{\text{method}\}$  data (points) vs Estruct  $\{2D\}$  results (curves). Second: Published  $v_2(b)\{\text{method}\}$  data (points) vs a universal relation describing  $\{2D\}$  results (solid line). Third: Published  $v_2\{EP\}(p_t, b)$  data (open points) vs the quadrupole component of the SS *jet* peak (solid triangles). Fourth: Same, but with nonzero  $\{2D\}$  nonjet quadrupole component (solid dots) and Estruct universal parametrization (dotted curve).

Fig. 6.5-1 (second) shows the same comparison in a format where the relation  $A_Q\{2D\}(b) \propto N_{binary}\epsilon_{opt}^2$  (bold straight line) is especially simple.  $N_{binary}$  is the number of binary nucleon-nucleon (N-N) collisions, and  $\epsilon_{opt}$  is the so-called *optical* Glauber A-A eccentricity assuming a smooth matter distribution. From the comparison it is clear that such a simple trend would not be apparent from published  $v_2$  data, given the large biases from jet correlations.

Fig. 6.5-1 (third) shows published  $v_2\{EP\}(p_t, b)$  data (open circles) for 0-5% central Au-Au collisions compared to the quadrupole component of the SS 2D jet peak (solid triangles). A small upper limit is placed on the nonjet quadrupole for this centrality (hatched band). We find that what is claimed to represent “elliptic flow” is in this case entirely jet structure.

Fig. 6.5-1 (fourth) shows the same comparison for 10-20% central Au-Au collisions where a nonzero nonjet quadrupole contribution is obtained (solid dots). The sum of nonjet quadrupole and that from the SS 2D jet peak (bold solid curve) accurately reproduces the  $\{EP\}$  data (open circles). The published  $v_2$  data are therefore very misleading. The dotted curve is the universal parameterization  $v_2\{2D\}(p_t, b, \sqrt{s_{NN}})$  for the nonjet quadrupole.

## 6.6 The sharp transition in minijet characteristics on centrality

D. J. Prindle, R. L. Ray\*, and T. A. Trainor

A central motivation for the study of high-energy nucleus-nucleus (A-A) collisions at the RHIC and LHC has been the possibility to form a unique new state of matter – a thermalized and flowing quark-gluon plasma or QGP – differing substantially from expectations for elementary hadronic (e.g., p-p or N-N) collisions. In order to assess properly the nature or even the existence of such novel material one must formulate a *null hypothesis* representing no novelty in A-A collisions. Such a hypothesis is based on a Glauber (eikonal) model of A-A collisions in which a succession of N-N collisions determined by A-A geometry is linearly superposed. Each N-N collision is assumed to produce hadrons with structure observed in isolated p-p collisions. We describe this as the *Glauber linear superposition* (GLS) reference.

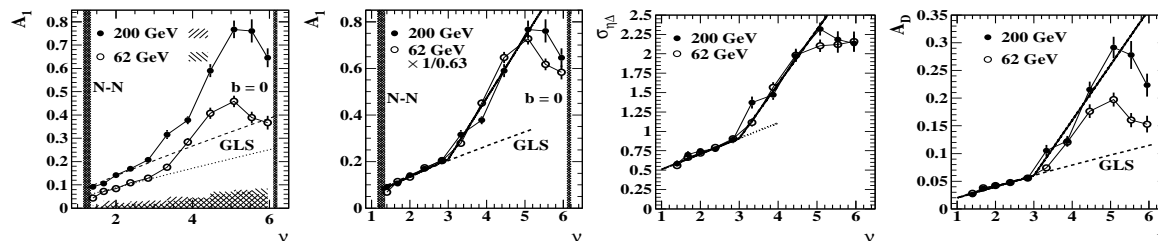


Figure 6.6-1. First: Fitted amplitudes for the SS 2D jet peak from two Au-Au collision energies. Second: The same data normalized by a QCD  $\log(\sqrt{s_{NN}})$  factor (0.63) showing a sharp transition in the slope at a common centrality  $\nu = 3$ . Third: The same for the SS peak pseudorapidity  $\eta$  width. Fourth: The same for the AS dipole (back-to-back jets) amplitude.

Fig. 6.6-1 (first) shows Estruct measurements of the SS 2D peak amplitude  $A_1$  (points) for eleven centrality bins (measured by mean nucleon path length  $\nu$ ) of 62- and 200-GeV Au-Au collisions. The dotted curves represent GLS references for the two energies. Fig. 6.6-1 (second) shows the same data with the 62-GeV data rescaled by the factor  $1/0.63$  expected from a  $\log(\sqrt{s_{NN}})$  trend also observed for the nonjet azimuth quadrupole. Data from the two energies are not then significantly different. It is apparent that data for the first five centrality bins do not deviate significantly from the GLS reference and don't falsify the null hypothesis at the few-percent level. Fig. 6.6-1 (third and fourth) show respectively the  $\eta$  width of the SS 2D peak and the amplitude of the away-side (AS) 1D peak (AS dipole) representing back-to-back jets in elementary p-p collisions. In the three cases the parameters accurately follow the GLS trend up to a centrality denoted by  $\nu = 3$  consistent with the null or linear-superposition hypothesis. Above that point substantial deviations are observed and the null hypothesis is falsified – something new happens. The amplitudes of the SS 2D and AS 1D peaks increase dramatically relative to the GLS, and the SS 2D peak  $\eta$  width also increases substantially. The azimuth width (not shown) *actually decreases*. Those parameters are interpreted as jet structure in elementary p-p collisions. Agreement with the GLS reference up to  $\nu = 3$  implies that the jet interpretation remains valid there. The jet interpretation remains a strong candidate above that point.

\*University of Texas, Austin, TX.

## 6.7 Uniqueness of the Estruct standard 2D fit model

D. J. Prindle, R. L. Ray\*, and T. A. Trainor

The Estruct standard 2D-fit model is established as a *necessary and sufficient* model of  $p_t$ -integral angular correlations. Each element of the model is *necessary* because its omission results in the same structure appearing in the fit residuals. The model is *sufficient* because the combination of necessary elements describes the data to their statistical limits. Recently, an initiative has emerged to add one or more “higher harmonics” (sextupole, octupole, etc.) to the Estruct standard model, motivated by a search for evidence of corresponding “flows” in the hadronic final state. When an additional sextupole term is added, for instance, the term is found to have a nonzero amplitude and other parameter values change substantially. The changes are interpreted to imply that the standard model is not unique, that the fitted parameter values have large uncertainties, and that other correlation components are present in the data. As recent Estruct studies have demonstrated, that argument is very misleading.

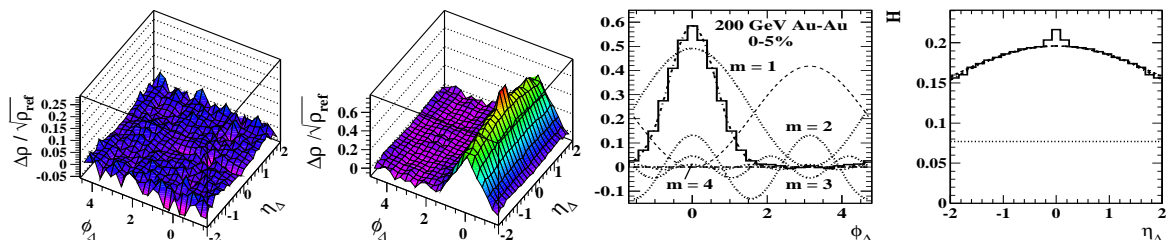


Figure 6.7-1. First: Residuals from Estruct standard fit to 0-5% central Au-Au collisions. Second: 2D data histogram with fitted AS dipole and nonjet quadrupole component subtracted revealing the SS 2D peak. Third: Projection of SS 2D peak onto azimuth (bold histogram) with several Fourier components ( $m$ ). Fourth: Projection of SS 2D peak onto pseudorapidity (histogram) with Gaussian from standard Estruct fit and Gaussian resulting from addition of a sextupole component to the standard model (curves indistinguishable).

Fig. 6.7-1 (first) shows the 2D fit residuals from 0-5% central Au-Au collisions for the standard 2D model with negligible residual structure. When the fitted AS dipole ( $m = 1$ ) and nonjet quadrupole ( $m = 2$ ) elements are subtracted from the data histogram, Fig. 6.7-1 (second) results. The peak is accurately described by a single 2D Gaussian (the narrow peak at the origin is irrelevant quantum correlations). The SS peak is then the only possible source of “higher harmonics” ( $m > 2$ ) in the data, as illustrated in Fig. 6.7-1 (third). When a sextupole ( $m = 3$ ) element is added to the standard model it can combine with the dipole and quadrupole elements to form a truncated Fourier series. *Observed* changes in those parameters reveal that the combined Fourier series is exactly equivalent to a 1D Gaussian on azimuth with the same width as the SS 2D peak. In effect, the added sextupole is equivalent to a change in the SS 2D peak model. A constant offset is added to the model factor describing the  $\eta$  dependence. Fig. 6.7-1 (fourth) shows a projection of the SS 2D data peak (histogram) compared to the model function from the standard model and the modification equivalent to the added sextupole (dashed and dash-dotted curves). The two curves are indistinguishable. Neither the substantial sextupole amplitude nor the equivalent offset is *systematically significant*.

\*University of Texas, Austin, TX.

## 6.8 The nonjet quadrupole in 200-GeV p-p collisions: theory vs data

D. J. Prindle and T. A. Trainor

So-called “elliptic flow” conventionally measured by  $v_2$ {method} is believed to arise in more-central Au-Au collisions from large energy densities and pressure gradients conjectured to develop there. Given that mechanism flows would be unexpected in elementary p-p collisions. However, Estruct measurements of  $v_2\{2D\}(b)$  vs Au-Au centrality provide evidence for a significant nonjet azimuth quadrupole  $v_2\{2D\}$  in N-N (p-p) collisions. A same-side (SS) “ridge” in recent LHC measurements of 7-TeV p-p collisions may be a manifestation of the nonjet quadrupole. And a pQCD theory calculation of  $v_2$  in 200 GeV p-p collisions<sup>1</sup> matches the Estruct Au-Au trend extrapolated to N-N. To confront the apparent contradiction we have measured 2D angular correlations vs charge multiplicity  $n_{ch}$  from 200-GeV p-p collisions.

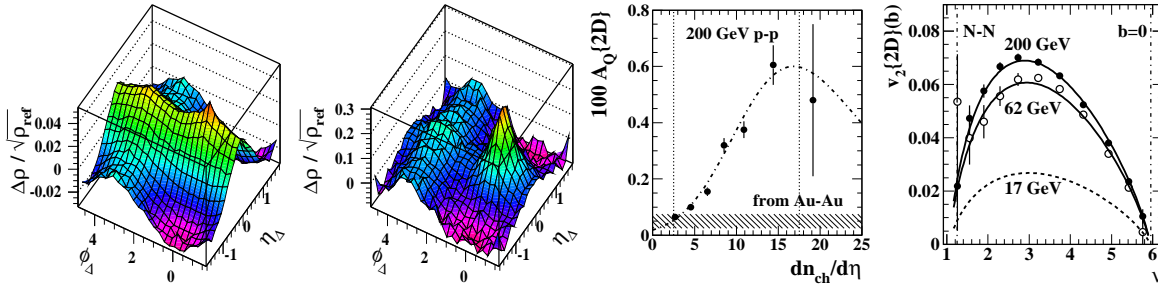


Figure 6.8-1. First:  $p$ - $p$  2D angular correlations for  $dn_{ch}/d\eta \approx 2$ . Second: angular correlations for  $dn_{ch}/d\eta \approx 14$ . Third: nonjet quadrupole per-particle amplitude  $A_Q\{2D\}$  vs  $p$ - $p$  particle density. Fourth: nonjet quadrupole  $v_2\{2D\}$  data vs Au-Au centrality.

Fig. 6.8-1 (first and second) show representative p-p 2D angular correlations for  $n_{ch} \approx 2$  and 14 in one unit of  $\eta$  (first and sixth event classes). The main trends are same-side (SS) 2D peak and away-side (AS) dipole (representing jets) rapidly increasing with  $n_{ch}$  and a 1D Gaussian on  $\eta_\Delta$  (representing projectile proton dissociation) increasing slowly with  $n_{ch}$ .

Fig. 6.8-1 (third) shows fitted values of nonjet quadrupole  $A_Q\{2D\}(b) = \rho_0(b)v_2^2\{2D\}(b)$  for seven multiplicity classes. The p-p quadrupole is observed to increase rapidly for smaller  $n_{ch}$  and then may saturate at larger  $n_{ch}$ . The hatched band is the value inferred for N-N collisions from Au-Au data, with systematic uncertainty. The dash-dotted curve is obtained by combining a hypothesis for the relation between  $n_{ch}$  and p-p centrality as measured by relative impact parameter  $b/b_0$  with the trend for  $A_Q\{2D\}(b)$  observed in Au-Au collisions. The overall amplitude has been scaled to fit the data.

Fig. 6.8-1 (fourth) shows  $v_2\{2D\}(b)$  for Au-Au collisions. The left-most 200-GeV data point (solid dot) compares well with the pQCD prediction  $v_2 = 0.02$  derived from a color dipole model. With further development of this analysis it may be possible to establish a direct link between QCD field theory and the measured nonjet azimuth quadrupole. More generally, such differential analysis is essential to define the “underlying event” for LHC p-p collisions required in searches for physics beyond the Standard Model.

<sup>1</sup>B. Z. Kopeliovich, A. H. Rezaeian, and Ivan Schmidt, Phys. Rev. D **78**, 114009 (2008).

## 6.9 Centrality vs $n_{ch}$ in 200-GeV p-p collisions

D. J. Prindle, and T. A. Trainor

Defining the collision centrality for elementary hadronic collisions is a longstanding problem that has taken on increased importance in the search for physics beyond the Standard Model at the LHC. A two-component (soft + hard) model with soft processes originating over a large hadron cross section and hard processes emerging from a smaller-radius core are consistent with electron deep-inelastic scattering (DIS) data. A correspondence between p-p geometry and physical observables is sought. The most accessible observable is the charge multiplicity. In our analysis we add (mini)jet and nonjet-quadrupole 2D correlation structure.

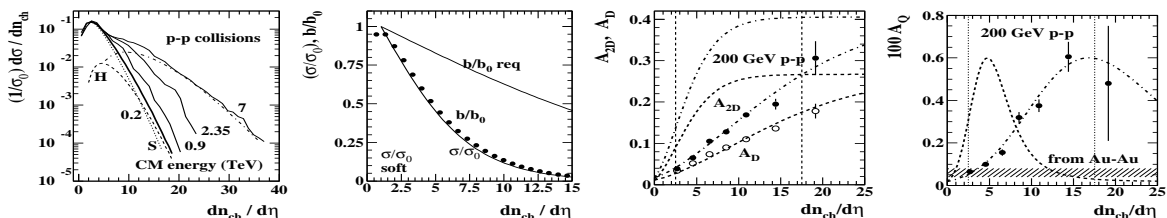


Figure 6.9-1. First: Minimum-bias distributions from p-p collisions at several energies – the 200-GeV distribution is decomposed into soft (S) and hard (H) components. Second: p-p fractional impact parameter vs  $n_{ch}$  inferred from MB data (points) and required to describe jet and nonjet quadrupole data (solid curve). Third: Fitted amplitudes for SS 2D and AS 1D jet peaks (points). Fourth: Fitted nonjet azimuth quadrupole amplitudes (points).

Fig. 6.9-1 (first) shows minimum-bias (MB) distributions for four p-p collision energies. We decompose the 200 GeV data into soft (S) and hard (H) components based on  $p_t$  spectrum analysis. Comparing the data trends it can be inferred that the soft component S varies little with collision energy, whereas the hard component H broadens and increases in amplitude logarithmically with energy. Fig. 6.9-1 (second) shows the relative impact parameter  $b/b_0$  (points) inferred from the 200-GeV MB distribution. Also shown is a similar curve rescaled by  $n_{ch}$  relevant to further argument below. Fig. 6.9-1 (third) shows SS 2D and AS 1D peak amplitudes from fits to measured 2D angular correlations representing jets and back-to-back jet pairs respectively. Fig. 6.9-1 (fourth) shows corresponding fitted nonjet quadrupole amplitudes.

To develop a centrality model we make the hypothesis that both (mini)jet and nonjet quadrupole production arise from low- $x$  gluon interactions concentrated in a reduced-diameter core within proton projectiles, as suggested by DIS data. The  $b/b_0$  vs  $n_{ch}$  relation for hard processes may be rescaled from the MB (soft process) data trend, as shown in Fig. 6.9-1 (second). We adopt the further hypothesis that p-p collisions can otherwise be described by the Glauber model applied to the geometry of intersecting spheres independent of absolute system size, leading to predictions for both jet production and nonjet quadrupole amplitude.

Fig. 6.9-1 (third and forth) show predicted trends for hard processes (right curves) vs soft or MB processes (left curves) compared to data inferred from 2D histograms. In each case the amplitudes have been scaled to match the data, but the shapes are derived from the Glauber model (minijets) and from the rescaled impact parameter (quadrupole and minijets).

## 6.10 Systematic distinctions between 2D jet structure and the nonjet quadrupole

T. A. Trainor

There is substantial supporting evidence that the same-side (SS) 2D peak in angular correlations from high-energy p-p and peripheral Au-Au collisions represents jets. However, in more-central Au-Au collisions SS 2D peak properties change substantially, especially strong elongation of the SS peak on pseudorapidity  $\eta$ . A trend has emerged in the past two years to reinterpret the SS peak in terms of hydrodynamic flows by reducing some or all angular correlations to a Fourier series on azimuth and interpreting each term as a “flow.”

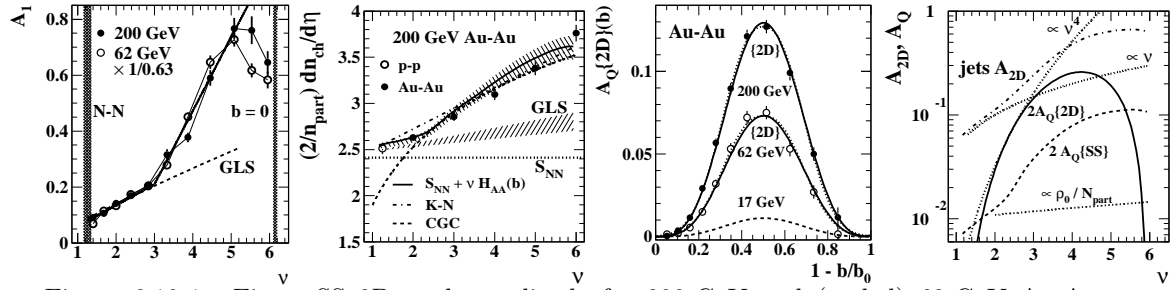


Figure 6.10-1. First: SS 2D peak amplitude for 200-GeV and (scaled) 62-GeV Au-Au collisions. Second: Per-participant yield vs centrality from spectra (points) and inference from jet correlations plus pQCD (solid curve). Third: Nonjet azimuth quadrupole data (points) and universal factorized parametrization (curves). Fourth: Centrality trends for jet structure (dash-dotted curve) and nonjet azimuth quadrupole (solid curve)

We observe that the SS 2D peak retains jet characteristics for all Au-Au centralities. In Fig. 6.10-1 (first) the SS peak amplitude exhibits a sharp transition in its centrality trend at  $\nu = 3$ , but in Fig. 6.10-1 (second) the SS peak volume combined with a pQCD calculation (solid curve) corresponds accurately to jet fragment spectrum yields,  $H_{AA}(b)$  (points), for all centralities. Azimuth multipoles (Fourier components) inferred from the SS 2D peak and attributed to “higher harmonic flows” must follow the same pQCD centrality trend.

In Fig. 6.10-1 (third) the nonjet azimuth quadrupole inferred from Estruct 2D fits exhibits a smooth universal centrality trend (points and curves) that includes no sharp transition. In Fig. 6.10-1 (fourth) the SS peak amplitude  $A_{2D}$  (dash-dotted curve) is compared directly with the nonjet quadrupole  $A_Q\{2D\}$  (solid curve) on a semilog plot to illustrate the great difference between the two centrality trends. Any attempt to interpret the SS 2D peak in terms of flows must reconcile two distinct quadrupole contributions  $A_Q\{2D\}$  and  $A_Q\{SS\}$  (both nominally “elliptic flow”) having such different centrality trends. We conclude that claims of “higher harmonic flows” inferred from SS 2D peak structure are inconsistent with the actual data trends. The physical origin of the SS peak in more-central Au-Au collisions remains parton fragmentation to jets, albeit modified by the Au-Au collision context.

### 6.11 Two-particle correlations in Au-Au collisions at $\sqrt{s_{NN}} = 200, 62, 39, 19, 11$ and 7 GeV

D. J. Prindle and T. A. Trainor

RHIC has performed a beam-energy scan (BES) looking for a critical point. For systems close to critical points correlation lengths become large. There is a common expectation that one of the beam energies will be close enough to a critical point that we can observe a change in correlation structure or, if the scan is too coarse, that below a transition energy a QGP signal disappears. In two-particle correlations we have observed unexpected behavior of the same-side peak dependence on centrality<sup>1</sup> for beam energies  $\sqrt{s_{NN}} = 62$  and 200 GeV. In peripheral collisions this peak is clearly associated with jets and is narrower in  $\eta_{\Delta}$  than it is in  $\phi_{\Delta}$ . As centrality is increased, so that the path length of the colliding nuclei is increased, the amplitude and  $\eta_{\Delta}$  width increase substantially while the  $\phi_{\Delta}$  width decreases. We are analyzing BES data to see if there is a beam-energy dependence to this behavior. We expect that, for beam energies below about  $\sqrt{s_{NN}} = 13$  GeV, jet production should be kinematically suppressed.

We characterize our two-particle correlations on  $(\eta_{\Delta}, \phi_{\Delta})$  with model components including a same-side 2D Gaussian (mentioned above), an away-side  $\cos(\phi_{\Delta})$  function (momentum conservation), a same-side narrow 2D exponential (HBT and  $e^+e^-$ ), a  $\cos(2\phi_{\Delta})$  function ( $v_2$ ), a 1D Gaussian on  $\eta_{\Delta}$  (fragmentation of partons continuing down the beam pipe), and a constant offset. The 1D Gaussian on  $\eta_{\Delta}$  changes as the beam rapidity is reduced bringing more of these projectile fragments into the STAR acceptance. When the 1D Gaussian is very broad there is a fitting ambiguity with the offset. Replacing it with  $A|\eta_{\Delta}|^{\alpha}$  stabilizes the fit and we use this functional form at and below  $\sqrt{s_{NN}} = 27$  GeV.

In our preliminary analysis we do not have tracking efficiency corrections, so fitted amplitudes may change. The amplitudes of the same-side 2D Gaussian and the away-side  $\cos(\phi_{\Delta})$  decrease as the beam energy is reduced, as expected. The amplitude of  $\cos(2\phi_{\Delta})$  also decreases roughly as expected. What is unexpected is that the  $\eta_{\Delta}$  broadening of the same-side 2D Gaussian seems to be independent of beam energy.

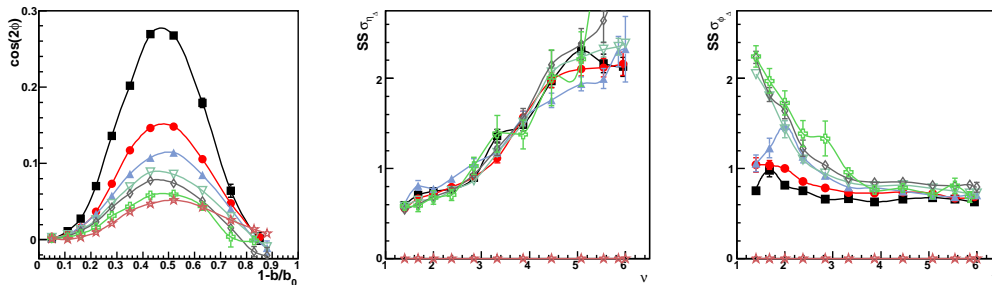


Figure 6.11-1. First:  $\cos(2\phi_{\Delta})$  amplitude. Second and Third:  $\eta_{\Delta}$  and  $\phi_{\Delta}$  widths of same-side 2D Gaussian. Beam energies are  $\sqrt{s_{NN}} = 200, 62, 39, 27, 19, 11$  and 7 GeV.

<sup>1</sup>CENPA Annual Report, University of Washington (2011) p. 77.

## 6.12 Analysis of new tracking code for STAR

D. J. Prindle

STAR has been taking and analyzing data for ten years. While the main TPC has always maintained the same geometry (although the electronics and DAQ have been upgraded), the interior, surrounding, and forward detectors have changed substantially. The proliferation of geometries makes it difficult to keep consistency between the Monte Carlo simulation and the reconstructed data. Further, the current tracking model is not compatible with the new forward tracking detectors which are disks perpendicular to the beam line. The STAR software-infrastructure team has launched an initiative to upgrade the tracking code with a more suitable track model and to use a geometry description that is common to both the Monte Carlo and the event reconstruction. We have been tasked with checking event samples to determine if the new reconstruction code is usable for physics production.

We compared data that had been reconstructed using the current production tracking code, referred to as *Sti*, and also reconstructed using the new code in development, *Stv*. *Stv* uses the GEANT Virtual Monte Carlo which can track through a non-uniform magnetic field (in contrast to *Sti*) and use the GEANT geometry information, hopefully leading to a better accounting of energy loss and multiple Coulomb scattering as well as better consistency with Monte Carlo simulations of the data. In addition to the two tracking algorithms we evaluated a new track-finding implementation using a cellular automaton (CA) which uses only local hit information and is about ten times faster than the track finder currently in use. Thus we had four production samples to compare: *Sti*, *StiCA*, *Stv* and *StvCA*.

CA variants find more tracks than the currently used track finder (for both *Sti* and *Stv*) and these extra tracks appear to be good. This is an improvement. There were, however, some problems with the current implementation of *Stv*. One small problem was that only primary tracks were saved. An important cut to reduce pileup contamination is the ratio of primary to global tracks. The data used for the comparison had significant pileup so this reduced the accuracy of our comparisons. For some analyses *Stv* seems to be a step forward, in particular for femtoscopic analysis. For the two-particle correlations used in *EStruct*, the number correlations are reasonable (albeit contaminated by pileup until a re-production is done saving the globals), but the  $p_t$  correlations are very odd. We tracked this down to *Stv* having a significant number of tracks with higher  $p_t$  than *Sti* has. This is clearly a problem with *Stv*.

The STAR software-infrastructure team is now reviewing *Stv* so they can fix the high  $p_t$  tail. After that is done (and global tracks are saved) we will presumably do another production comparison.

## 7 Other research

### Status of nonlocal quantum communication test

J. G. Cramer, B. Parris, and D. B. Pengra

The question we have been investigating in this experiment is whether the intrinsic nonlocality of standard quantum mechanics is the private domain of Nature, as is generally assumed by the physics community, or whether in special circumstances the nonlocal connection between subsystems can be used to send signals from one observer to another. With the aid of generous private contributions and some use of CENPA resources, we have continued the work on this test of nonlocal quantum communication, which has been reported in the past five years<sup>1,2,3,4,5</sup>. The initial configuration of the experiment, as described in the first two references, employed a high-power argon-ion laser operating at about 1 W at 351 nm that pumped nonlinear crystals (BBO or LiIO<sub>3</sub>) to produce pairs of momentum-entangled 702-nm photons, on which measurements were subsequently performed. Signal-to-noise limitations arising from a background of fluorescence photons competing with the entangled-photon-pair signal prevented the planned measurements with the initial configuration.

The work is continuing in the Optics Laboratory on the 2nd floor of the Physics-Astronomy Building, which offered the advantage that the experimental area can be darkened without interference with other experiments. A new experimental configuration, described in last year's CENPA Annual Report<sup>5</sup> uses a periodically-poled potassium titanyl phosphate (pp-KTP) crystal with a 10- $\mu$ m poling length and dimensions 1 mm $\times$ 2 mm $\times$ 30 mm from Raicol, Inc. The ppKTP crystal is maintained at 50° C in a precision crystal oven and pumped with a 405 nm Sacher Littow-type grating-stabilized diode laser.

In the past year we have been attempting to increase the signal-to-noise ratio of the experiment, which represents the primary roadblock in testing nonlocal communication. We mounted six avalanche photodiodes (APDs), a thermistor temperature monitor, and a light-pulsar LED on the cold-finger of a surplus liquid-nitrogen cryostat formerly used with a silicon x-ray detector. Light fibers were cemented to the APDs and brought out of the cryostat through small holes in a port made vacuum-tight with TorrSeal. Then the cryostat was filled with liquid nitrogen, and the diodes were operated in Geiger mode and tested with a pulsed-LED light source mounted inside the cryostat near the APDs and with photons sent to them through the light fibers.

The results of these tests were somewhat disappointing. The voltage-fluctuation noise level in the APDs did indeed drop with temperature, but so did the voltage threshold at which the avalanche breakdown occurred. In principle, a liquid-nitrogen cryostat should be capable of going down to a temperature of 77 K, but our system, presumably because of heat

---

<sup>1</sup>CENPA Annual Report, University of Washington (2007) p. 52.

<sup>2</sup>CENPA Annual Report, University of Washington (2008) p. 42.

<sup>3</sup>CENPA Annual Report, University of Washington (2009) p. 41.

<sup>4</sup>CENPA Annual Report, University of Washington (2010) p. 93.

<sup>5</sup>CENPA Annual Report, University of Washington (2011) p. 94.

leaks through the electrical connections, produced a minimum equilibrium temperature of about 99 K. We observed APD avalanche thresholds of around 282 V at room temperature and of around 44 V at 99 K. Because the size of the voltage fluctuations fairly closely tracks the avalanche threshold, we found that there was no significant improvement in the noise level arising from spontaneous avalanche breakdown at the lower temperatures. In fact, the best signal-to-noise situation seemed to occur at around 270 K. This suggests that Peltier cooling of the APDs should be adequate, and that cooling to liquid nitrogen temperatures is counter-productive.

The other way in which we attempted to increase the signal-to-noise ratio of the experiment was to investigate pulsing of the 100-mW 405-nm Sacher grating-stabilized laser that produces entangled photon pairs in the nonlinear ppKTP crystal of the system. The idea was that if the same number of laser-derived pump photons could be delivered in a tight bunch rather than in a continuous wave, the signal photons would be similarly bunched and time-correlated while noise due to spontaneous avalanches in the APDs and random 810-nm noise photons from fluorescence in the nonlinear crystal would not. Therefore, we developed pulsing of the Sacher laser.

The Sacher diode module has a modulation input connection, but we found that putting voltage pulses into this port produced no effect. However, inside the box we discovered a switch not documented in the manual which, when moved to the other position, permitted modulation of the unit. The next problem was that a rather small coupling capacitor in the unit coupled the modulation signal to the laser diode, and that laser operation could be turned off for only a limited time interval. We solved this problem by using a programmable HP pulser that delivered a complicated stair-step waveform.

However, at about the time the laser pulsing was ready to use, the Sacher laser began to have operational problems. These took the form of low output and “crashes” when normal drive currents were applied. The Sacher unit as delivered in 2009 produced a maximum output power of about 100 mW. This had fallen to about 25 mW by 2011, lower but still probably adequate for the experiment. However, recent measurements indicate that the present maximum power output of the unit is only about 40  $\mu$ W. In the coming year, our first priority will be to obtain a new 405-nm laser and/or get the Sacher unit repaired. We will also implement Peltier cooling for APD units of the system, as indicated by our experience this year.

## 8 Education

### 8.1 Use of CENPA facilities in education and course work at UW

G. C. Harper

CENPA has always maintained a prominent role in broad-scoped, practical, hands-on training for both undergraduate and graduate students at the University of Washington. One of the most significant and unique advantages that our students enjoy is direct participation in the ongoing local research at CENPA and the engineering contributions to our off-site collaborations.

We have been increasing our presence in undergraduate education and in the spring, 2011, quarter we provided an accelerator-based laboratory course in nuclear physics (see Sec. 8.2). This was an undergraduate special-topics course in physics, course number 499, which we intend to continue to provide on a regular basis. Another undergraduate classroom application of CENPA facilities included the use of one of our radioactive sources in a radiochemistry course this year (see Sec. 8.3) for activating materials to be used in laboratory experiments.

We continue to provide extensive hands-on training for both undergraduate and graduate students. Our electronics shop is available for use by the students (see Sec. 9.4) where they can learn electronic design and assembly. In the student shop (see Sec. 9.5) all users are trained in machine tool operation and safety. Finally, CENPA has a long history of teaching students accelerator and ion-source operation (see Sec. 8.4).

### 8.2 Accelerator-based lab class in nuclear physics

N. M. Boyd, A. García, G. C. Harper, A. Knecht, and D. I. Will

We have developed a class dedicated to teaching undergraduates simple aspects of techniques for nuclear-physics experiments including tuning beams through the accelerator<sup>1</sup>.

The class met once a week during the spring quarter of 2011 with lectures of about one hour and practice by the students which lasted up to 6 hours per week. The list of subjects we covered were:

1. Basics of  $\gamma$  ray detection. Ge detectors. Detecting radioactivity from the reactor accidents in Japan.
2. Basic workings of accelerators. Tuning beam through our tandem.
3. Basic electronics for data acquisition.
4. Rutherford scattering and the sizes of nuclei.
5. Resonances in nuclear reactions. Nucleosynthesis of elements in stars.

---

<sup>1</sup>Phys499: Basic Tools for Experimental Nuclear Physics: <http://faculty.washington.edu/agarcia3/phys499>.

The emphasis was on allowing all students to acquire hands-on experience in all practical aspects. Quizzes and homework assignments gave us indications that the class was effective. Seven out of eight students in the class expressed interest in continuing with research at CENPA.



Figure 8.2-1. Students near the Rutherford scattering beam line, getting ready for the experiment.

### 8.3 Radiochemistry and nuclear-chemistry education program in the UW Department of Chemistry

K. A. Krohn<sup>\*</sup>, D. I. Will, and W. H. Zoller<sup>†</sup>

The tracer principle using radionuclides is critically important in disciplines ranging from basic chemical and biochemical mechanisms to human medicine, from atmospheric chemistry to geochemistry, and from materials science to cosmology. Several years ago the Howard Hughes Foundation funded nuclear-detection instrumentation for Chemistry 410, a lecture/laboratory course in Radiochemistry and Nuclear Chemistry taught each winter quarter and limited by equipment workstations to 16 students. In order to maintain a fresh course the curriculum is updated each year to reflect the application interests of students. The basic science of radiation detection and the safe handling of isotopes are covered in the first four sessions. The students are then taken to various working laboratories to gain hands-on experience in using radionuclides to answer important science questions.

<sup>\*</sup>Professor of Radiology & Radiation Oncology, Adjunct Professor of Chemistry, University of Washington, Seattle, WA.

<sup>†</sup>Emeritus Professor, Department of Chemistry, University of Washington, Seattle, WA.

One trip is to the Washington State Department of Health Laboratory for a practical experiment in counting long-lived  $\alpha$  and  $\beta$  emitters. The exercise is done in the context of a realistic terrorism scenario where the students are presented with an unknown sample wipe test and asked to gauge the magnitude of the threat. A second trip is to the Applied Physics Laboratory to use X-ray fluorescence to analyze an unknown substance.

Protein labeling by radio-iodination is a common method for attaching an exogenous label to important biological molecules. This exercise provides practical experience in handling open sources of radionuclides and teaches the role surveys play in detecting radioactive contamination following the laboratory exercise. Chelation labeling is another approach for attaching a detectable signal to an interesting molecule. We do an experiment using  $^{99m}\text{Tc}$ , which is commonly used for medical imaging.

While many radionuclides are commercially available, an even larger number need to be made on demand. The nuclear reactions for this purpose use neutrons or charged particles to induce nuclear reactions. The students gain experience with both methods. We use the UW Medical Center cyclotron to make  $^{13}\text{NH}_3$  for imaging the heart muscle using positron emission tomography. The students learn basic aspects of cyclotron engineering and medical imaging instrumentation as well as radiochemical synthesis in a clean room so that the radiopharmaceutical product is safe for human injection. We also make radionuclides using neutrons. Because a reactor is not available at UW, we use the  $\alpha$ -Be neutron source from CENPA for this purpose. The neutrons are thermalized by scattering through polyethylene and are used to irradiate different pure elements for neutron activation analysis and then to identify the composition of an unknown alloy.

#### 8.4 Student training

N. M. Boyd, G. C. Harper, D. R. Hyde, D. A. Peterson, and D. I. Will

At CENPA students are trained in a variety of technical laboratory skills that include accelerator operation, machining, and electronics. During the 10 days of accelerator crew training this year, 11 students were taught to operate the ion sources and the tandem Van de Graaff accelerator. These students practiced generating an ion beam, charging the tandem, and tuning the beam through the accelerator.

At least 14 people (including RAs, REU students, and undergraduate hourlies) have received training in the CENPA student shop this year and many of them have completed our training course. These students have learned to safely operate a variety of machines including our lathes, milling machines, drill presses, saws, grinders, the metal shear and break, and hand and power tools. Three students were trained to use an oxygen/acetylene cutting torch. Two students have been trained on the student shop NC 2-Axis Trak milling machine in order to make complicated parts for their research projects.

In the electronics shop, at least four students have been instructed this year in soldering and wiring. Students also frequently gain experience with vacuum systems and cryogenics as dictated by the needs of their experiment.

## 9 Facilities

### 9.1 Facilities overview

G. C. Harper

CENPA constantly adjusts and improves its facilities in order to provide the best possible resources and research environment for its users as new experiments emerge and as the demands of research change with time. In addition we maintain high-quality shop services that are available to the faculty, staff, and students.

The computational facilities at CENPA remain at the front edge of technology. As always, personal desktop and portable computers are maintained and the technology kept current. The NPL Data Center (NPLDC) which previously contained a single high performance cluster, ATHENA, now provides the infrastructure to multiple clusters and department appliances (see Sec. 9.2).

The FN tandem Van de Graaff accelerator lab undergoes changes regularly to accommodate new experiments and provide support for accelerator-related projects. The accelerator lab is also a hands-on training facility for students. The students are trained to operate the accelerator and ion sources. An undergraduate course using the accelerator to perform nuclear-physics experiments has also been developed. The accelerator can be quickly switched between two different operational modes to provide a wide energy range with high beam intensity over the entire range. The ion sources are modified as needed to accommodate a wide variety of experimental requirements (see Sec. 9.3).

The CENPA electronics shop provides modern surface-mount technology and miniature cable manufacturing equipment on site and in appropriately clean areas. The shop continues to do custom design work for specialty pre-amps as well as dedicated multichannel DAQ systems. The shop also interacts with the on-campus Washington Technology Center, taking advantage of much of the capital-intensive, high-tech equipment there that is more effectively used as a cost-shared facility. The electronics shop staff also provides training for students and other staff members (see Sec. 9.4).

The CENPA instrument shop and student shop provide a unique climate for a research facility. The student shop is headed by an instrument maker who provides safety training and instruction to students, staff, and faculty. Our main instrument shop is manned by two highly skilled instrument makers with decades of experience working in the university and research environments. The instrument makers interact with students, staff, and faculty on a daily basis, providing instruction on how to design physically realizable devices and how to correctly document design changes (see Sec. 9.5).

Laboratory space is reallocated as needed, as new large experiments are initiated at or move to CENPA. The entire east end of the accelerator tunnel, both inside and outside the building, continues to be modified to house the ADMX experiment. New lab space is being opened up to provide testing facilities for the development of experiments and detectors for the muon and neutrino programs (see Sec. 9.6).

## 9.2 Laboratory computer systems

G. T. Holman

CENPA is a mixed shop of Windows 7, XP, Mac OS X and various Linux distributions. Windows 7 is installed on new systems but we are still running Windows XP for data-acquisition systems. In previous years the IT focus was directed toward server consolidation, network security, process documentation and removal of redundant processes. We continue to utilize Xen virtualization to drive most web pages, Elogs, wiki, calendar, tracking, and document servers. The CENPA website and research group web pages are run on a virtual Debian server and utilize the Drupal web framework. The NPL mail server still provides NPL presence but all email is relayed to UW email hardware as this allows users direct management.

Two Dell 510 20-TB servers (Lisa and Marie) were purchased to replace Crunch4 and offer increased user storage, print server capability, and improved backup policy. Linux, Windows and Mac workstations are now backed up to the Lisa 20-TB raid farm from which they are written to LTO tape by the Physics Computer Center on a three-month backup retention plan. Lisa runs the Crash Plan Pro backup application which supports Linux, Mac, Windows, and Solaris operating systems and provides differential and encrypted backups. Whereas workstations rely on Crash Plan Pro for backups, all servers use rsync and rsnapshot. Marie provides 20 TB for research, user, and shared group data. All Crunch servers were transitioned into virtual appliances for CENPA user and research-group domains.

The NPL Data Center (NPLDC) provides the critical infrastructure supporting high-performance scientific-computing applications that cannot be efficiently executed on typical commodity server infrastructures (e.g., the Amazon EC2 Cloud). NPLDC space is shared by Physics, the Institute for Nuclear Theory (INT), CENPA, and the Astronomy departments. In previous years the space housed a single cluster that was treated as one computational resource, also known as Athena.

Today, to meet the wide and highly specialized array of research requirements, the cluster has been separated into specific instances. The computational hardware infrastructure supports six different instances of the cluster: three cluster instances that leverage Infiniband interconnects (classified as HPC clusters) and three clusters that primarily run single-threaded applications (non-HPC clusters.) The HPC clusters primarily use Torque/Maui via the three clusters' dedicated front ends.

The data requirements in the NPLDC have also rapidly grown. Approximately one third of the rack space is dedicated to non-cluster hardware: NFS scratch storage, SQL, MySQL, and backup servers. These servers constitute over 200 TB of raw disk space. The computational clusters instances continue to use 23.7 TB of SAN storage on a HP/Polyserve NFS Cluster. This is an order of magnitude increase in specialized, low-cost storage for both cluster and desktop scientific computing. Planning is underway to migrate serial/VAX based controllers to TCP/Labview this year.

### 9.3 Van de Graaff accelerator and ion source operations and development

Z. T. Alexander, N. M. Boyd, T. M. Cope, G. C. Harper, T. G. MacDonald,  
D. A. Peterson, S. P. R. Steininger\*, T. D. Van Wechel, and D. I. Will

The tandem was entered only once this year. After observing tandem stripper foils failing very rapidly (in under 30 seconds) when running a 1-10  $\mu\text{A}$ , 17-MeV  $^2\text{H}$  beam, the tank opening of 7 March, 2011, revealed melted foil frames. Realigning the frame-holding assembly resolved this problem, resulting in measured foil longevity of over 10 hours for a 10- $\mu\text{A}$  17-MeV  $^2\text{H}$  beam on mechanically slackened foils. The realignment was achieved in 3 steps. First, the bracket on the front-back foil aperture box was machined down by 0.025" shifting it beam-left with respect to a foil frame. Second, the aperture box was realigned such that it was square with respect to the beam direction (one of the retaining-screw holes had been drilled out and the box was therefore tilted). Third, the steering-assembly plate (attached to the aperture box) was realigned with respect to a blank foil frame. This phenomenon and our solution were reported at the SNEAP 2011 conference<sup>1</sup>.

Further damages to the accelerator were incurred during experiments conducted in March, 2012, as a result of tuning a high energy beam at high currents. A 17.8-MeV, 14- $\mu\text{A}$   $^2\text{H}$  beam (constituting 249 W at the high energy end) burned holes in two bellows, one in the object region and one in the crossover region. These vacuum regions were repaired with the addition of internal stainless-steel tube shielding to protect the bellows. Repairs were also made to the Tesla meter for injector deck analyzing magnet.

<b>ACTIVITY SCHEDULED</b>	<b>DAYS SCHEDULED</b>	<b>PERCENT of TIME</b>
Ion implantation, deck ion sources	0	0
Nuclear-physics research, accelerator	34	9
Subtotal, ion implant or nuclear-physics research	34	9
Development, maintenance, or crew training	23	6
Grand total	57	15

Table 9.3-1. Tandem Accelerator Operations 1 April, 2011, to 31 March, 2012 .

During the 12 months from 1 April, 2011 to 31 March, 2012 the tandem pellet chains operated 233 hours, the SpIS operated 0 hours, and the DEIS operated 284 hours. Additional statistics of accelerator operations are given in Table 9.3-1.

Ion beams produced using the DEIS this year included 5.5–17.8-MeV  $^2\text{H}$  for the  $^6\text{He}$  experiment, 1-MeV  $^1\text{H}$  for the Muon group, and 3.0-MeV  $^1\text{H}$  for the Physics 499 class, and 53-MeV  $^{16}\text{O}$  for crew training.

\*Currently at Radiation Oncology, University of Washington

<sup>1</sup>Symposium for Northeastern Accelerator Personnel, SNEAP 2011, ORNL, Oak Ridge, TN.

## 9.4 Electronics shop

D. A. Peterson and T. D. Van Wechel

The electronics shop is responsible for the design and construction of new laboratory electronic equipment and for the maintenance and repair of existing CENPA electronics. Projects undertaken by the electronics shop this past year included the following:

1. Continued to develop MAJORANA preamp. A new lower-noise board has been designed and tested, and several low-noise FETs have been evaluated this year.
2. Built 20 new cathode preamps for the MuSun experiment.
3. Designed and built VME summing boards for the KATRIN veto.
4. Designed and built an optical pulser for KATRIN focal-plane-detector calibration.
5. Modified 75 SNO NCD preamps for use in the HALO project.
6. Designed preamplifier for the KATRIN Tritium Recoil Ion Mass Spectrometer.
7. Produced fused silica connector paddles for the MAJORANA connectors.
8. Designed and built several readout boards for the evaluation of silicon photomultipliers for the g-2 experiment.
9. Designed a VCO driver for  ${}^6\text{He}$ .
10. Designed copper to fiber optic boards for the focal plane detector of the KATRIN experiment.
11. Designed and build two beam line controllers for  ${}^6\text{He}$ .
12. Designed and built manual magnet steerer for Van de Graaff accelerator.

## 9.5 CENPA instrument shops

J. H. Elms, G. C. Harper, D. R. Hyde, and H. Simons

The CENPA main instrument shop completed several large projects this year.

1. Two cryostats for testing single crystal strings for the MAJORANA experiment. These consisted of several OFHC copper parts and required the CNC lathe (see Sec. 1.2.3).
2. Two large-diameter, ultra-high-vacuum in-line isolation valves for the KATRIN main spectrometer (see Sec. 1.1.4).
3. A heat pipe and LN<sub>2</sub> manifold for KATRIN (see Sec. 1.1.4).

4. A very large vacuum flange for the ADMX main magnet cryostat, which was composed of many individual vacuum flanges. This required a substantial number of precise vacuum welds (see Sec. 5.1).
5. Modification of some large existing flanges and retrieval of the bucking coil from the ADMX vacuum chamber (see Sec. 5.1).
6. A very delicate “parking brake” for the gravity group’s torsion balance.
7. A large mu-metal shield for inside the vacuum vessel of the cryogenic torsion balance (see Sec. 2.1.7).

The student shop produced several small projects in addition to providing machine-tool training and safety training for the faculty, staff, and students.

1. A small-scale, crystal detector and photomultiplier tube box was produced for testing a variety of detector arrays for the muon group’s  $g - 2$  experiment (see Sec. 4.4.1).
2. Small parts for the NCDs used in the HALO project (see Sec. 1.4).
3. Cryostat pit installation components for ADMX (see Sec. 5.1).
4. Various parts for torsion balance experiments (see Sec. 2.1).
5. An aluminum vacuum mounting plate for the UCNA experiment.

## 9.6 Building upgrades for ADMX

N. M. Boyd, A. Wagner, and D. I. Will

The installation of the Axion Dark Matter eXperiment (ADMX) at the east end of the CENPA accelerator tunnel requires both alteration of the building to accommodate the large (11 ft) main magnet, and substantial additional infrastructure to supply the experiment with power. In order to situate the magnet for useful operation a 3-ft-deep pit was excavated at the east end of the tunnel. This pit brings the top of the magnet level with a 1.5-ft inset in the concrete floor permitting convenient access for power, pump lines, and cryogenics via a false floor. Power is supplied to the experiment from a 1200-A breaker panel located 30 ft down the tunnel.

Aside from the magnet, the largest piece of infrastructure required by the experiment is a He liquefier. The Linde-model L1410 liquefier with RS compressor was selected for this purpose. The liquefier and compressor will be located 15 ft from the main magnet. The compressor requires approximately 4 kW of power with commensurate cooling supplied by a water chiller. Recovery of the He gas will be accomplished by a gas bag to be hung on the east wall and several compressors feeding an intermediate storage buffer and ultimately the large pre-existing He gas tank. The back fence was substantially enlarged to make room for a concrete pad to accommodate this infrastructure. Installation of the water chiller, recovery lines and recovery compressors should commence in the early fall of 2012 and installation of the liquefier should be completed in early 2013.

## 10 CENPA Personnel

### 10.1 Faculty

Eric G. Adelberger <sup>1</sup>	Professor Emeritus
Hans Bichsel <sup>1</sup>	Affiliate Professor
John G. Cramer <sup>1</sup>	Professor Emeritus
Peter J. Doe	Research Professor
Sanshiro Enomoto	Research Assistant Professor; CENPA Fellow
Frank Fleischer <sup>1,2</sup>	Research Assistant Professor
Alejandro García	Professor
Jens H. Gundlach <sup>1</sup>	Professor
Blayne R. Heckel <sup>1</sup>	Professor; Chair
David W. Hertzog	Professor
C. D. Hoyle <sup>1,3</sup>	Affiliate Assistant Professor
Peter Kammel	Research Professor
Michael L. Miller <sup>4</sup>	Research Assistant Professor; CENPA Fellow
R. G. Hamish Robertson	Professor; Director
Leslie J Rosenberg <sup>1</sup>	Professor
Stephan Schlamming <sup>1,5</sup>	Research Assistant Professor
Kurt A. Snover <sup>1</sup>	Research Professor Emeritus
Derek W. Storm <sup>1</sup>	Research Professor Emeritus
Nikolai R. Tolich	Assistant Professor
Thomas A. Trainor	Research Professor
Robert Vandenbosch <sup>1</sup>	Professor Emeritus
William G. Weitkamp <sup>1</sup>	Research Professor Emeritus
John F. Wilkerson <sup>1,6</sup>	Affiliate Professor
Tianchi Zhao	Research Associate Professor

### 10.2 CENPA External Advisory Committee

Baha Balantekin	University of Wisconsin
Stuart Freedman	UC Berkeley and Lawrence Berkeley National Laboratory
Wick Haxton	UC Berkeley and Lawrence Berkeley National Laboratory
William Zajc	Columbia University

<sup>1</sup>Not supported by DOE CENPA grant.

<sup>2</sup>Faculty appointment, November, 2011.

<sup>3</sup>Affiliated faculty, Humboldt State University, Arcata, CA.

<sup>4</sup>Departed February, 2012, currently at Cloudant, Inc.

<sup>5</sup>On leave to N.I.S.T., November, 2010.

<sup>6</sup>Affiliated faculty, University of North Carolina, Chapel Hill, NC.

### 10.3 Postdoctoral Research Associates

Jarek Kaspar  
 Brendan Kiburg<sup>3</sup>  
 Andreas Knecht  
 Diana Parno  
 Gray Rybka<sup>1</sup>  
 Hok Wan Chan Tseung

Krishna Venkateswara<sup>1</sup>  
 Andrew Wagner<sup>1</sup>  
 Frederik Wauters<sup>4</sup>  
 Peter Winter  
 Chris Wrede<sup>5</sup>

### 10.4 Predoctoral Research Associates

Yelena Bagdasarova<sup>6</sup>  
 Laura Bodine  
 Ted Cook<sup>1</sup>  
 Jason Crnkovic<sup>1</sup>  
 Ian Derrington<sup>1,7</sup>  
 Nathan Froemming<sup>8</sup>  
 Brent Graner  
 Charles Hagedorn<sup>1</sup>  
 Ran Hong  
 Michael Hotz<sup>1</sup>  
 David Kettler  
 Sara Knaack<sup>1</sup>  
 Jared Kofron

Jonathan Leon  
 Dmitry Lyapustin<sup>1</sup>  
 Timothy Major  
 Eric Martin  
 Michael Murray  
 Alexis Schubert  
 Daniel Scislawski<sup>9</sup>  
 William Terrano<sup>1</sup>  
 Matthew Turner<sup>1</sup>  
 Todd Wagner<sup>1</sup>  
 Brandon Wall  
 Brett Wolfe<sup>10</sup>  
 David Zumwalt

### 10.5 NSF Research Experience for Undergraduates participants

Megan Geen  
 Arman Ballado  
 Micah Koller

Wheaton College  
 University of Florida  
 Carleton College

---

<sup>1</sup>Not supported by DOE CENPA grant.

<sup>2</sup>Feodor Lynen Fellow.

<sup>3</sup>Arrived June, 2011.

<sup>4</sup>Arrived October, 2011.

<sup>5</sup>Departed August, 2011, Michigan State University, East Lansing, MI.

<sup>6</sup>Arrived August, 2011.

<sup>7</sup>Graduated November, 2011.

<sup>8</sup>Arrived September, 2011.

<sup>9</sup>On leave August, 2011.

<sup>10</sup>Departed May, 2011.

**10.6 University of Washington graduates taking research credit**

Niklas Mueller	Nikolai Tolich, Advisor
Rachel Rosten	Hamish Robertson, Advisor
Rachel Ryan	Peter Kammel, Advisor
Matthias Smith	David Hertzog, Advisor

**10.7 University of Washington undergraduates taking research credit**

Shawn Apodaca	Nikolai Tolich, Advisor
Trevor Arp	Jens Gundlach, Advisor
Jennie Chen	Blayne Heckel, Advisor
Tyler Cope	Alejandro García, Advisor
Brent Delbridge <sup>1</sup>	Andreas Knecht, Chris Wrede, Advisors
Blake Freeman <sup>2</sup>	Chris Wrede, Advisor
Holly Hess	Eric Adelberger, Advisor
Eric Lee-Wong	Blayne Heckel, Advisor
Troy MacDonald	Alejandro García, Advisor
James Mulligan	Nikolai Tolich, Advisor
Stephen Plachta	Jens Gundlach, Advisor
Devin Short	Alejandro García, Advisor
Satoshi Utsuno <sup>3</sup>	Chris Wrede, Advisor
Thomas Wolowiec	Leslie Rosenberg, Advisor
Alexandria "Sasha" Zhdanova	Charlie Hagedorn, Advisor

**10.8 Professional staff**

John F. Amsbaugh	Research Engineer	KATRIN vacuum systems
Nora M. Boyd	Research Engineer	ADMX installation, accelerator
Tom H. Burritt	Research Engineer	Design of KATRIN detector system
Gregory C. Harper	Associate Director	Accelerator, ion sources
Gary T. Holman	Systems Manager	Computer Systems
Duncan J. Prindle, Ph.D.	Research Scientist	Heavy ion research
Hendrik Simons	Instrument Maker	Shop Supervisor
H. Erik Swanson, Ph.D.	Research Physicist	Precision experimental equipment
Timothy D. Van Wechel	Electronics Engineer	Analog and digital electronics design
Douglas I. Will	Senior Engineer	Cryogenics, ion sources, buildings

<sup>1</sup>Graduated December, 2011.<sup>2</sup>Graduated June, 2011.<sup>3</sup>Returned to Keio University, Japan, June, 2011.

## 10.9 Technical staff

James H. Elms	Instrument Maker
David R. Hyde	Instrument Maker
David A. Peterson	Electronics Technician

## 10.10 Administrative staff

Victoria A. Clarkson	Administrator
Kate J. Higgins <sup>1</sup>	Fiscal Specialist
Robert S. Shupe	Fiscal Specialist

## 10.11 Part-time staff and student helpers

Zachery Alexander<sup>2</sup>  
 Trevor Arp<sup>3</sup>  
 Tyler Cope  
 Robert Fiszer<sup>4</sup>  
 Rachel LeFree<sup>5</sup>  
 Brynn MacCoy<sup>6</sup>  
 Troy MacDonald<sup>2</sup>  
 Elizabeth McBride<sup>3</sup>  
 Stephen Plachta<sup>3</sup>  
 Clifford Plesha<sup>2</sup>  
 Devin Short  
 Arielle Steger<sup>6</sup>  
 Steven Steininger<sup>7</sup>  
 Aaron Stoll<sup>3</sup>  
 Kevin Wierman<sup>8</sup>

---

<sup>1</sup>Departed October, 2011

<sup>2</sup>Arrived October, 2011.

<sup>3</sup>Arrived June, 2011.

<sup>4</sup>Graduated and departed December, 2011.

<sup>5</sup>Arrived August, 2011.

<sup>6</sup>Arrived November, 2011.

<sup>7</sup>Departed September, 2011, Department of Radiation Oncology, University of Washington Hospital.

<sup>8</sup>Graduated, departed for University of North Carolina, Chapel Hill, NC, June, 2011.

## 11 Publications

Publications and presentations with a date of 2011 or 2012 are included below. Some entries from early 2011 may therefore also appear in the 2011 Annual Report.

### 11.1 Published papers

“Solar fusion cross sections II: the pp chain and CNO cycles,” E. G. Adelberger, A. García, R. G. H. Robertson, K. A. Snover, A. B. Balantekin, K. M. Heeger, M. J. Ramsey-Musolf, D. Bemmerer, A. Junghans, C. A. Bertulani, J.-W. Chen, H. Costantini, P. Prati, M. Couder, E. Uberseder, M. Wiescher, R. Cyburt, B. Davids, S. J. Freedman, M. Gai, D. Gazit, L. Gialanella, G. Imbriani, U. Greife, M. Hass, W. C. Haxton, T. Itahashi, K. Kubodera, K. Langanke, D. Leitner, M. Leitner, P. Vetter, L. Winslow, L. E. Marcucci, T. Motobayashi, A. Mukhamedzhanov, R. E. Tribble, K. M. Nollett, F. M. Nuñez, T.-S. Park, P. D. Parker, R. Schiavilla, E. C. Simpson, C. Spitaleri, F. Strieder, H.-P. Trautvetter, K. Suemmerer, and S. Typel; *Rev. Mod. Phys.* **83**, 195 (2011).

“Low Multiplicity Burst Search at the Sudbury Neutrino Observatory,” B. Aharmim *et al.* (SNO Collaboration); *Ap. J.* **728**, 83 (2011); arXiv:1011.5436 [hep-ex].

“Four methods for determining the composition of trace radioactive surface contamination of low-radioactivity metal,” H. M. O’Keeffe, T. H. Burritt, B. T. Cleveland, G. Doucas, N. Gagnon, N. A. Jelley, C. Kraus, I. T. Lawson, S. Majerus, S. R. McGee, A. W. Myers, A. W. P. Poon, K. Rielage, R. G. H. Robertson, R. C. Rosten, L. C. Stonehill, B. A. VanDevender, T. D. Van Wechel; *Nuclear Inst. and Methods in Physics Research, A* **659** (2011), 182; arXiv: 1103.5788 (2011).

“Arrival time and magnitude of airborne fission products from the Fukushima, Japan, reactor incident as measured in Seattle, WA, USA,” J. Diaz Leon *et al.*, *J. Env. Rad.* **95**, 1032 (2011).

“A High-Intensity Source of  $^6\text{He}$  Atoms for Fundamental Research,” A. Knecht *et al.*, *Nucl. Instrum. Methods Phys. Res., Sect. A* **660**, 43 (2011).

“Full simulation of the Sudbury Neutrino Observatory proportional counters,” B. Beltran *et al.*, *New J. Phys.* **13**, 073006 (2011).

“Performance of a TiN-coated monolithic silicon pin-diode array under mechanical stress,” B. A. VanDevender, L. I. Bodine, A. W. Myers, J. F. Amsbaugh, M. A. Howe, M. L. Leber, R. G. H. Robertson, K. Tolich, T. D. Van Wechel, B. L. Wall, *Nucl. Instrum. Methods in Phys. Research A* **673** 46 (2012).

“Picoradian deflection measurement with an interferometric quasi-autocollimator using weak value amplification,” M. D. Turner, C. A. Hagedorn, S. Schlamminger, and J. H. Gundlach, *Opt. Lett.* **36**, 1479-1481 (2011); arXiv:1103.4426.

“Upgraded photon calorimeter with integrating readout for Hall A Compton Polarimeter at Jefferson Lab,” M. Friend, D. Parno, F. Benmokhtar, A. Camsonne, M. Dalton, G. B. Franklin, V. Mamyan, R. Michaels, S. Nanda, V. Nelyubin, K. Paschke, B. Quinn, A. Rakhman, P. Souder, A. Tobias, Nucl. Instrum. Methods A **676**, 96 (2012).

“Design and performance of the ADMX SQUID-based microwave receiver,” S.J. Asztalos, G. Carosi, C. Hagmann, D. Kinion, K. van Bibber, M. Hotz, L. J. Rosenberg, G. Rybka, A. Wagner, J. Hoskins, C. Martin, N. S. Sullivan, D. B. Tanner, R. Bradley, J. Clarke, Nucl. Instrum. Methods A **656**, 39 (2011).

“Search for nonvirialized axionic dark matter,” J. Hoskins, J. Hwang, C. Martin, P. Sikivie, N. Sullivan, D. B. Tanner, M. Hotz, L. J. Rosenberg, G. Rybka, A. Wagner, S. J. Asztalos, G. Carosi, C. Hagmann, D. Kinion, K. van Bibber, R. Bradley, J. Clarke, Phys. Rev. D **84**, 121302(R) (2011).

“Measurement of linear stark interference in  $^{199}\text{Hg}$ ,” T. H. Loftus, M. D. Swallows, W. C. Griffith, M. V. Romalis, B. R. Heckel, and E. N. Fortson, Phys. Rev. Lett. **106**, 253002 (2011).

“Absolute determination of the  $^{22}\text{Na}(p, \gamma)$  reaction rate in novae,” A. L. Sallaska, C. Wrede, A. García, D. W. Storm, T. A. D. Brown, C. Ruiz, K. Snover, D. F. Ottewell, L. Buchmann, C. Vockenhuber, D. A. Hutcheon, J. A. Caggiano, J. José, Phys. Rev. C **83**, 034611 (2011).

“Preparation of a  $^{114m}\text{In}$  low-energy conversion-electron source,” C. Wrede, B. W. Filippone, A. García, S. Lassell, J. Liu, M. P. Mendenhall, A. S. C. Palmer, R. W. Pattie, Jr., A. R. Young, Nucl. Instrum. Methods B **269**, 1113 (2011).

“Branches of  $^{33}\text{S}(p, \gamma)^{34}\text{Cl}$  at Oxygen-Neon Nova Temperatures,” B. Freeman *et al.*, Phys. Rev. C **83**, 048801 (2011).

“A New Limit on Time-Reversal Violation in Beta Decay,” H. P. Mumm, T. E. Chupp, R. L. Cooper, K. P. Coulter, S. J. Freedman, B. K. Fujikawa, A. García, G. L. Jones, J. S. Nico, A. K. Thompson, C. R. Tull, J. F. Wilkerson, F. E. Wietfeldt, Phys. Rev. Lett. **107**, 102301 (2011).

“Precision Measurement of the  $^6\text{He}$  Half-Life and the Weak Axial Current in Nuclei,” A. Knecht, R. Hong, D. W. Zumwalt, B. G. Delbridge, A. García, P. Müller, H. E. Swanson, I. S. Towner, S. Utsuno, W. Williams, C. Wrede, Phys. Rev. Lett. **108**, 122502 (2012).

“Experimental Validation of the Largest Calculated Isospin-Symmetry-Breaking Effect in a Superallowed Fermi Decay,” D. Melconian, S. Triambak, C. Bordeanu, A. García, J. C. Hardy, V. E. Iacob, N. Nica, H. I. Park, G. Tabacaru, L. Trache, I. S. Towner, R. E. Tribble and Y. Zhai, Phys. Rev. Lett. **107**, 182301 (2011).

“The  $\beta^-$  Decay of  $^{32}\text{Cl}$ : Precision  $\gamma$ -Ray Spectroscopy and a Measurement of Isospin-Symmetry Breaking,” D. Melconian, S. Triambak, C. Bordeanu, A. García, J. C. Hardy, V. E. Iacob, N. Nica, H. I. Park, G. Tabacaru, L. Trache, I. S. Towner, R. E. Tribble, and Y. Zhai, Phys. Rev. C **85**, 025501 (2012).

“The forbidden pleasures of experimental physics,” A. García, AIP Conf. Proc. **1423**, 257 (2012).

“Search for an Annual Modulation in a P-type Point Contact Germanium Dark Matter Detector,” C. E. Aalseth *et al.*, Phys. Rev. Lett. **107**, 141301 (2011).

“Production of ultracold neutrons from cryogenic  $^2\text{H}_2$ ,  $\text{O}_2$ , and  $\text{C}_2\text{H}_4$  converters,” F. Atchison *et al.*, Eur. Phys. Lett **95**, 12001 (2011).

“Ellipsometric measurements of the refractive indices of linear alkylbenzene and EJ-301 scintillators from 210 to 1000 nm,” H. Wan Chan Tseung, N. Tolich, Phys. Scr. **3**, 035701 (2011).

“Measurement of the dependence of the light yields of linear alkylbenzene-based and EJ-301 scintillators on electron energy,” H. Wan Chan Tseung, J. Kaspar, N. Tolich, Nucl. Instrum. Methods A **654**, 318 (2011).

“Gluon correlations from a Glasma flux-tube model compared to measured hadron correlations on transverse momentum ( $\mathbf{p}_t, \mathbf{p}_t$ ) and angular differences ( $\eta_\Delta, \phi_\Delta$ ),” T. A. Trainor and R. L. Ray, Phys. Rev. C **84**, 034906 (2011).

“Comparing the same-side ‘ridge’ in CMS p-p angular correlations to RHIC p-p data,” T. A. Trainor and D. T. Kettler, Phys. Rev. C **84**, 024910 (2011).

“Parton fragment yields derived from minimum-bias jet angular correlations,” T. A. Trainor and D. T. Kettler, Phys. Rev. C. **83**, 034903 (2011).

“Partial radiogenic heat model for Earth revealed by geoneutrino measurements,” A. Gando *et al.* (KamLAND Collaboration), Nature Geoscience **4**, 647-651 (2011).

“Measurement of the  $^8\text{B}$  solar neutrino flux with the KamLAND liquid scintillator detector,” S. Abe *et al.* (KamLAND Collaboration), Phys. Rev. C **84**, 035804 (2011).

“Constraints on  $\theta_{13}$  from a Three-Flavor Oscillation Analysis of Reactor Antineutrinos at KamLAND,” A. Gando *et al.* (KamLAND Collaboration), Phys. Rev. D **83**, 052002 (2011).

“Measurement of the Positive Muon Lifetime and Determination of the Fermi Constant to Part-per-Million Precision,” D. M. Webber *et al.* (MuLan Collaboration), Phys. Rev. Lett. **106**, 041803 (2011).

“High Precision Study of Muon Catalyzed Fusion in  $\text{D}_2$  and HD Gas,” D. V. Balin *et al.*, Physics of Particles and Nuclei **42**, 185 (2011).

“The 10 bar hydrogen time projection chamber of the MuCap experiment,” J. Egger *et al.*, Nucl. Instrum. Meth. A **628**, 199 (2011).

“The G0 Experiment: Apparatus for Parity-Violating Electron Scattering Measurements at Forward and Backward Angles,” D. Androić *et al.* (G0 Collaboration), Nucl. Instrum. Meth. A **646**, 59-86 (2011).

## 11.2 Papers submitted or to be published 2012

“Final Analysis of Solar Neutrino Data from the Sudbury Neutrino Observatory,”  
 B. Aharmim, S. N. Ahmed, A. E. Anthony, N. Barros, E. W. Beier, A. Bellerive, B. Beltran,  
 M. Bergevin, S. D. Biller, K. Boudjemline, M. G. Boulay, T. H. Burritt, B. Cai, Y. D. Chan,  
 D. Chauhan, M. Chen, B. T. Cleveland, G. A. Cox, X. Dai, H. Deng, J. Detwiler,  
 M. DiMarco, P. J. Doe, G. Doucas, P.-L. Drouin, C. A. Duba, F. A. Duncan, M. Dunford,  
 E. D. Earle, S. R. Elliott, H. C. Evans, G. T. Ewan, J. Farine, H. Fergani, F. Fleurot,  
 R. J. Ford, J. A. Formaggio, N. Gagnon, J. T. M. Goon, K. Graham, E. Guillian, S. Habib,  
 R. L. Hahn, A. L. Hallin, E. D. Hallman, P. J. Harvey, R. Hazama, W. J. Heintzelman,  
 J. Heise, R. L. Helmer, A. Hime, C. Howard, M. A. Howe, M. Huang, B. Jamieson,  
 N. A. Jelley, K. J. Keeter, J. R. Klein, L. L. Kormos, M. Kos, C. Kraus, C. B. Krauss,  
 T. Kutter, C. C. M. Kyba, J. Law, I. T. Lawson, K. T. Lesko, J. R. Leslie, I. Levine,  
 J. C. Loach, R. MacLellan, S. Majerus, H. B. Mak, J. Maneira, R. Martin, N. McCauley,  
 A. B. McDonald, S. McGee, M. L. Miller, B. Monreal, J. Monroe, B. Morissette,  
 B. G. Nickel, A. J. Noble, H. M. O’Keeffe, N. S. Oblath, G. D. Orebi Gann, S. M. Oser,  
 R. A. Ott, S. J. M. Peeters, A. W. P. Poon, G. Prior, S. D. Reitzner, K. Rielage,  
 B. C. Robertson, R. G. H. Robertson, R. C. Rosten, M. H. Schwendener, J. A. Secrest,  
 S. R. Seibert, O. Simard, P. Skensved, T. J. Sonley, L. C. Stonehill, G. Tesic, N. Tolich,  
 T. Tsui, R. Van Berg, B. A. VanDevender, C. J. Virtue, B. L. Wall, D. Waller,  
 H. Wan Chan Tseung, D. L. Wark, N. West, J. F. Wilkerson, J. R. Wilson, J. M. Wouters,  
 A. Wright, M. Yeh, F. Zhang, and K. Zuber (SNO Collaboration) Phys. Rev. C (submitted  
 September 5, 2011); arXiv 1109.0763.

“Decay studies for neutrino physics: Electron capture decays of  $^{100}\text{Tc}$  and  $^{116}\text{In}$ ,”  
 A. García, S. Sjuve, E. Swanson, C. Wrede, D. Melconian, A. Algora, I. Ahmad, *Hyperfine  
 Interact.*, in press.

“Measurement of the  $\nu_e$  and Total  $^8\text{B}$  Solar Neutrino Fluxes with the Sudbury Neutrino  
 Observatory Phase-III Data Set,” B. Aharmim *et al.* (SNO Collaboration), Submitted to  
 Phys. Rev. C (2011).

“Search for time-reversal symmetry breaking in neutron beta decay,” A. García,  
 T. E. Chupp, R. L. Cooper, K. P. Coulter, S. J. Freedman, B. K. Fujikawa, G. L. Jones,  
 H. P. Mumm, J. S. Nico, A. K. Thompson, C. A. Trull, F. E. Wietfeldt, J. F. Wilkerson,  
 Proceedings of PAVI11, the 5th International Workshop “From Parity Violation to  
 Hadronic Structure and more...,” *Il Nuovo Cimento C*, in press.

“Azimuth multipoles vs minimum-bias jets in 2D angular correlations on  $\eta$  and  $\phi$ ,”  
 T. A. Trainor, arXiv:1109.2540, submitted to J. Phys. G.

“Measurement of the Double-Beta Decay Half-life of  $^{136}\text{Xe}$  in KamLAND-Zen,” A. Gando  
*et al.* (KamLAND Collaboration), Phys. Rev. C (accepted); arXiv 1201.4664.

“Stripper Foil Longevity,” N. M. Boyd, October, 2011, SNEAP 2011, Oak Ridge National  
 Laboratory, Knoxville, TN.

“Glasma flux tubes vs minimum-bias jets in 2D angular correlations on  $\eta$  and  $\phi$ ,”  
T. A. Trainor, arXiv:1012.2373, submitted to J. Phys. G.

“Anomalous centrality evolution of two-particle angular correlations from Au-Au collisions at  $\sqrt{s_{NN}} = 62$  and 200 GeV,” G. Agakishiev *et al.* (STAR Collaboration). arXiv:1109.4380, submitted to Phys. Rev. C.

### 11.3 Invited talks, abstracts, and other conference presentations

“Solar neutrino flux in 3 lines,” R. G. H. Robertson, Invited talk, “Sterile Neutrinos at the Crossroads” workshop, Virginia Tech, Blacksburg, VA, September 26 – 28, 2011.

“Catching up with the neutrino,” R. G. H. Robertson, Colloquium, Mississippi State University, November 7, 2011.

“Weighing neutrinos: What is the mass scale?” R. G. H. Robertson, Invited talk, “Fundamental Physics at the Intensity Frontier” Workshop, Washington, DC, November 30 – December 2, 2011.

“Catching up with the neutrino,” R. G. H. Robertson, Invited talk, Symposium on Electroweak Nuclear Physics, Duke University, Durham, NC, March 8 – 9, 2012.

“University of Washington Lab Report to SNEAP 2011,” N. M. Boyd, T. M. Cope, G. C. Harper, D. A. Peterson, D. A. Short, S. P. R. Steininger, T. D. VanWechel, and D. I. Will, October, 2011, SNEAP 2011, Oak Ridge National Laboratory, Knoxville, TN.

“Muon Capture on the Proton and Determination of the Nucleon’s Pseudoscalar Form Factor  $g_P$ ,” P. Winter, Invited talk at the 19th Particles and Nuclei International Conference (PANIC11), MIT, Cambridge, MA, July 24th – 29th, 2011.

“Quantum weak-value amplification for torsion-balance experiments,” M. D. Turner, Colloquium, Department of Physics, Brigham Young University, Provo, UT, November 2011.

“Measuring airborne radioactivity from the Fukushima incident,” A. Knecht, Invited talk, Physics Seminar, Indiana University, South Bend, IN, October 2011.

“Review of soft interactions and multiparticle correlations,” T A. Trainor, to be published in the Proceedings of the XLI International Symposium on Multiparticle Dynamics (ISMD2012), Miyajima Island, Hiroshima, Japan, September 26 – 30, 2012, arXiv:1110.3292.

“The forbidden pleasures of experimental physics,” A. García, Plenary talk at the IX Latin American Symposium on Nuclear Physics and Applications, Quito, Ecuador, July 20, 2011.

“Weak interactions in nuclei: a probe to search for new physics,” A. García, Physics Colloquium at Tulane University, New Orleans, LA, November 30, 2011.

“Angular deflection measurement using quantum weak-value amplification,” M. D. Turner, Particle Astrophysics Seminar, Fermi National Accelerator Laboratory, Batavia, IL, June 2011.

“Fundamental physics with ultracold neutrons,” A. Knecht, Invited talk, Physics Division Seminar, Argonne National Laboratory, Chicago, IL, May 2011.

“The MAJORANA DEMONSTRATOR: A search for neutrinoless double-beta decay of germanium-76,” A. G. Schubert on behalf of the MAJORANA Collaboration, Particles and Nuclei International Conference 2011 (PANIC11), MIT, Cambridge, MA, July 2011.

“The MAJORANA DEMONSTRATOR: A search for neutrinoless double-beta decay of germanium-76,” A. G. Schubert on behalf of the MAJORANA Collaboration, April APS Meeting, Anaheim, CA, April 2011.

“The ‘soft ridge’ – is it initial-state geometry or modified jets?,” T A. Trainor, to be published in the Proceedings of the XLI International Symposium on Multiparticle Dynamics (ISMD2012), Miyajima Island, Hiroshima, Japan, September 26 – 30, 2012, arXiv:1110.3293.

“Measurement of light yield dependence on electron energy for SNO+ scintillator,” H. Wan Chan Tseung, 2011 Fall Meeting of the APS Division of Nuclear Physics, Michigan State University, October 2011.

“Muon Capture on the Proton: Final results from the MuCap experiment,” P. Winter, Invited talk at the APS April meeting, Atlanta, GA, March 30 – April 3, 2012.

“Understanding RHIC Collisions: Modified QCD fragmentation vs quark coalescence from a thermalized flowing medium,” T A. Trainor, Published in the Proceedings of the XL International Symposium on Multiparticle Dynamics (ISMD2010), University of Antwerp, Antwerp, Belgium, September 21 – 25, 2010, University Press Antwerp (N. van Remortel and P. Van Mechelen, Eds.) arXiv:1011.6351.

“Precision physics with muons – Unveiling physics at the PPM level,” P. Winter, Seminar at Brookhaven National Laboratory, Long Island, NY, April 3, 2012.

“The new g-2 experiment: Taking the muon’s anomalous moment to the next precision level,” P. Winter, Seminar at Michigan State University, East Lansing, MI, April 10, 2012.

“Muons and GlobusOnline,” P. Winter, Talk at GlobusWORLD, Argonne National Laboratory, Lemont, IL, April 12, 2012.

“The SNO+ experiment,” H. Wan Chan Tseung, Particle Physics Seminar, Brookhaven National Laboratory, September 2011.

“Muon capture on the proton: Final results from the MuCap experiment Fermilab,” B. Kiburg, Joint Experimental-Theoretical Seminar, April 6, 2012.

“Search for time-reversal symmetry breaking in neutron beta decay,” A. García, Invited talk at PAVI11, the 5th International Workshop “From Parity Violation to Hadronic Structure and more...,” Rome, Italy, September 5, 2011.

“What can geo-neutrinos tell us about the Earth?,” N. Tolich, Invited talk, Division of Nuclear Physics meeting, East Lansing, MI, October 27, 2011.

“Neutrinos from heaven and hell,” N. Tolich, University of Washington, Department of Physics Colloquium, Seattle, WA, May 16, 2011.

“What can geo-neutrinos tell us about the Earth?,” N. Tolich, Los Alamos National Laboratory, Physics Division Colloquium, Los Alamos, NM, September 28, 2011.

“Precision Muon Physics: Capturing a Moment in a Lifetime,” D. W. Hertzog, Helmut W. Baer Lecture in Physics (Colloquium), University of Michigan, November 9, 2011.

“Measurement of the Positive Muon Lifetime and Determination of the Fermi Constant to ppm precision,” D. W. Hertzog, Seminar, Argonne National Laboratory, January 23, 2012.

“Precision Muon Physics: Capturing a Moment in a Lifetime,” D. W. Hertzog, Colloquium, University of Victoria, February 8, 2012.

“Precision Muon Physics: Capturing a Moment in a Lifetime,” D. W. Hertzog, Colloquium, University of Alberta, March 16, 2012.

“Preliminary Measurement of Longitudinal Spin Asymmetry  $A_1$  on  $^3\text{He}$ ,” D. Parno, APS April Meeting, Anaheim, CA, April 30–May 3, 2011.

#### 11.4 Patents

“Interferometric Quasi-Autocollimator,” U.S. Patent Application No. 13/426,309, unpublished (filing date Mar. 21, 2012) (M. D. Turner, J. H. Gundlach, C. A. Hagedorn, and S. Schlamming, applicants).